# The Archean Hammond Reef deposit: the formation of an orogenic gold deposit in a contractional step-over-zone along a major strike-slip fault system

by

Gabrielle Fouillard

A thesis submitted in partial fulfillment
of the requirements for the degree of
Master of Science (MSc) in Geology

The Faculty of Graduate Studies
Laurentian University
Sudbury, Ontario, Canada

# THESIS DEFENCE COMMITTEE/COMITÉ DE SOUTENANCE DE THÈSE

## Laurentian Université/Université Laurentienne

Office of Graduate Studies/Bureau des études supérieures

| | | |
|---|---|---|
| Title of Thesis<br>Titre de la thèse | The Archean Hammond Reef deposit: the formation of an orogenic gold deposit in a contractional step-over-zone along a major strike-slip fault system | |
| Name of Candidate<br>Nom du candidat | Fouillard, Gabrielle | |
| Degree<br>Diplôme | Master of Science | |
| Program<br>Programme | MSc Geology | Date of Defence<br>Date de la soutenance January 20, 2023 |

**APPROVED/APPROUVÉ**

Thesis Examiners/Examinateurs de thèse:

Dr. Bruno Lafrance
(Supervisor/Directeur(trice) de thèse)

Dr. Ross Sherlock
(Committee member/Membre du comité)

Dr. Stéphane Perrouty
(Committee member/Membre du comité)

Dr. Lori Kennedy
(External Examiner/Examinateur externe)

Approved for the Office of Graduate Studies
Approuvé pour le Bureau des études supérieures
Tammy Eger, PhD
Vice-President Research (Office of Graduate Studies)
Vice-rectrice à la recherche (Bureau des études supérieures)
Laurentian University / Université Laurentienne

## ACCESSIBILITY CLAUSE AND PERMISSION TO USE

I, **Gabrielle Fouillard**, hereby grant to Laurentian University and/or its agents the non-exclusive license to archive and make accessible my thesis, dissertation, or project report in whole or in part in all forms of media, now or for the duration of my copyright ownership. I retain all other ownership rights to the copyright of the thesis, dissertation or project report. I also reserve the right to use in future works (such as articles or books) all or part of this thesis, dissertation, or project report. I further agree that permission for copying of this thesis in any manner, in whole or in part, for scholarly purposes may be granted by the professor or professors who supervised my thesis work or, in their absence, by the Head of the Department in which my thesis work was done. It is understood that any copying or publication or use of this thesis or parts thereof for financial gain shall not be allowed without my written permission. It is also understood that this copy is being made available in this form by the authority of the copyright owner solely for the purpose of private study and research and may not be copied or reproduced except as permitted by the copyright laws without written authority from the copyright owner.

# Abstract

Hammond Reef is an orogenic gold deposit with a measured and indicated resource estimate of 3.3 Moz at an average grade of 0.84 g/t gold. It is located within the south-central region of the Wabigoon Subprovince in northwest Ontario. It is hosted within a system of north- to northeast-trending anastomosing shear zones, called the Marmion Shear System (MSS), which straddles the contact between the Mesoarchean Diversion stock to the west and Marmion Batholith to the east. Multiple shear sense indicators, including the deflection of mylonitic foliations in shear zones, drag folds, and shear bands, suggests that the MSS is a major sinistral transcurrent fault system. The bulk of gold mineralization is concentrated in an ENE-trending bend along the MSS, characterized by intense sericite and carbonate alteration. Mineralization formed between 2700-2690 Ma and is associated with syn-tectonic hydrothermal quartz breccias and shallowly dipping quartz-carbonate veins with down-dip striations, which formed during bulk NNW-directed shortening across the bend. This suggests that the Hammond Reef deposit formed along a contractional step-over-zone between two regional sinistral transcurrent faults. Compression across the bend resulted in more fracturing that localized the migration of hydrothermal fluids and the precipitation and concentration of gold.

# Keywords

Marmion Shear System, Marmion Batholith, Diversion stock, Hammond Reef gold deposit, Step-over-zones, orogenic gold mineralization, Archean gold deposit

# Co-Authorship Statement

The thesis is written as a manuscript for publication in an economic geology journal. The manuscript has multiple authors; this section outlines the many contributions made by the candidate and co-authors:

1. This project was developed by Dr. Bruno Lafrance. The co-author visited the field site and reviewed mapping results upon completion.
2. Field mapping and sample collection was completed by the candidate with the assistance of Khadija Kadu (2020) and Olivia Meier (2021). Mapping was conducted at a 1:2500 scale with additional mapping at a 1:100 scale.
3. Eighty-three samples were collected by the candidate from outcrops, saw cuts and drill core. The samples were cut by the candidate and thin sections were prepared at Vancouver Petrographic LTD. Petrographic analysis was conducted by the candidate with consultation from Dr. Lafrance. Sample preparation was conducted by the student and samples were sent to ALS Laboratories for whole rock geochemistry. One sample for zircon U-Pb TIMS was sent to the Jack Satterly Lab at the University of Toronto.
4. U-Pb TIMS ages were performed by Mike Hamilton at the Jack Satterly Lab at the University of Toronto and in-situ U-Pb monazite ages and sulfide maps were conducted by Jeff Marshall at the Mineral Exploration Research Centre - Isotope Geochemistry Lab (MERC-IGL) at Laurentian University.
5. All initial interpretations of the data and thesis drafts were prepared by the candidate with guidance and review from the co-authors.

# Acknowledgments

I would like to thank my supervisor, Dr. Bruno Lafrance, for his guidance, support, and patience during many challenges. You have taught me a tremendous amount and I appreciated that deeply.

Thank you to Dr. Jeffrey Marsh for all your excellent lab work and to all the working staff at the Mineral Exploration Research Center. This project would not have been possible without your support. A special acknowledgement to Lynn Bulloch, Courtney Folz, Natalie Lafleur-Roy, Roxanne Mehes, and Dr. Kirk Ross.

Thank you to my committee members Dr. Ross Sherlock and Dr. Stéphane Perrouty for your reviews and input on my project, it is greatly appreciated.

Thank you to Agnico Eagle Mines for their kind contributions and support during my research. Thank you to my field assistants Khadija Kadu (2020) and Olivia Meier (2021) for all their hard work. Lastly, a big thank you to Gilbert Dickson “Bud” for his help during my time in Atikokan, ON.

Thank you to all my amazing friends, especially to Mattea McRea, Emily Archibald, Jenna Whitney, Ruth Orlóci-Goodison, Shalaila Bhalla and Jacob Metzger. You have all stood by my side and encouraged me to keep going, whether it was in the office, on the trail or on the wall.

Thank you to my incredibly supportive family, you have always believed in me even when I didn’t believe in myself. Thank you to my adorable nieces and nephews for always putting a smile on my face.

I greatly appreciate all the help and support from everyone who has made this possible.

This project area is situated on lands under Treaty 3 (1792) between the British Crown and the Mississauga First Nation and is located north of the Nigigoonsiminikaaning First Nations communities

# Table of Contents

Abstract ........ iii

Co-Authorship Statement ........ iv

Acknowledgments ........ v

List of Tables ........ viii

List of Figures ........ ix

List of Appendices ........ xiv

Chapter 1 ........ 1

1 Introduction to Thesis ........ 1

- 1.1 Research Problem ........ 1
- 1.2 Objectives of Thesis ........ 2
- 1.3 Structure of Thesis ........ 2

Chapter 2 ........ 4

2 The Archean Hammond Reef deposit: the formation of an orogenic gold deposit in a contractional step-over-zone along a major strike-slip fault system ........ 4

- 2.1 Introduction ........ 4
- 2.2 Regional Geology ........ 5
- 2.3 Methodology ........ 7
- 2.4 Results ........ 10
  - 2.4.1 Marmion Shear System ........ 10
  - 2.4.2 Alteration and Mineralization ........ 16
  - 2.4.3 Geochronology ........ 25
- 2.5 Discussion ........ 35
  - 2.5.1 Structural Interpretation ........ 35
  - 2.5.2 Alteration and Mineralization Interpretation ........ 39

2.5.3 Comparison to other gold deposits in the Wabigoon subprovince ........... 42

2.6 Conclusions ........................................................................................... 44

References ................................................................................................. 45

Appendices ................................................................................................. 95

# List of Tables

Table 1: Summary of mineral chemistry from alteration associated with mineralized veins and alteration at the Hammond Reef deposit. 19

Table 2: Whole rock major elements (wt. %) and trace elements (ppm) of representative samples of altered and precursor porphyritic tonalite. 23

Table 3: Monazite U-Pb isotopic data from various mineralized veins within the Hammond Reef deposit. 28

Table 4: Zircon U-Pb isotopic data for Diverson stock tonalitic intrusion, Hammond Reef area. 34

# List of Figures

Figure 1: Outline of the subprovinces and terranes of the Superior Province (Wheeler et al., 1997; Montsion et al., 2018), with inset map to the top left showing the location of the Superior Province in North America. The Hammond Reef deposit is represented by a red star, and yellow circles are for geographical reference and represent the communities of Red Lake and Thunder Bay. .......... 60

Figure 2: Regional map of the MSS showing the location, extent, and orientation of its anastomosing shear zones (Modified from Stone 2010, Osisko, 2013). Location of the Hammond Reef deposit in the western Superior Province is indicated by a red star on the top left inset map, which is modified after Montsion et al. (2018). UTM coordinates in NAD83 Zone 15N. .......... 61

Figure 3: Map of the southern domain showing the MSS, with structural measurements and important outcrops discussed in text shown as filled red circles. Contours on upper stereonet diagram are in 2% of total data points per 1% area of the stereonet plots. Foliation, shear zones, conjugate faults and veins are plotted as poles. Number of measurements and average orientation of the plotted structural features at the bottom right of the stereonet plots. NAD83 Zone 15N UTM coordinates. .......... 63

Figure 4: Field photographs from Gold Mine Island in the southern domain. a) Zone of closely-spaced sinistral fractures with sericite alteration halos delineated by broken red lines. Quartz vein (blue lines) is sinistrally offset along the fractures (broken red lines). Camera cap (5.8 cm in diameter) for scale. b) Close-up photograph of sinistrally offset quartz vein (blue line) in (a). Fractures are represented by broken red lines. Camera cap (5.8 cm in diameter) for scale. c) Quartz veins (solid blue line) bisecting the angle between two sets of sericite altered shear fractures (broken red line) forming bridges between two fractures (broken yellow lines). Camera cap (5.8 cm in diameter) for scale. d) Foliation (solid red line) defined by sericite alteration. Ser = sericite; Carb = carbonate; QCC = quartz-carbonate-chlorite. .......... 64

Figure 5: Detailed map of Outcrop #5 showing a quartz breccia vein emplaced in a sericitic sinistral shear zone. UTM coordinates NAD83 Zone 15N. Location of outcrop is shown in

Figure 3. Encircled numbers and letters 6a, 6b, 6c refer to field photographs shown in Figure 6. ........................................................................................................................ 65

Figure 6: Field photographs and photomicrographs from Outcrop #5 in the southern domain a) Sericitic foliation (solid red line) dragged in anticlockwise manner along quartz breccia vein. Camera cap (5.8 cm in diameter) for scale. b) S-shaped drag folds along contact (solid black line) between medium grained tonalite and fine grained tonalite. Photo card (8.5 cm in length) for scale. c) Foliated host rock fragments within breccia vein. Foliation is represented by solid red line. d) Photomicrograph of porphyritic tonalite comprised dominantly of quartz and feldspar. Quartz shows undulose optical extinction, low angle boundaries, and irregular recrystallized margins, and is surrounded by smaller recrystallized quartz grains and sericite. Crossed polars. e) Photomicrograph of fractured plagioclase with kink bands. Crossed polars. f) Close-up of (e). Primary muscovite partially replaced by finer-grained sericite showing a sigmoidal mica fish geometry indicative of sinistral movement. Crossed polars. Plag = plagioclase; Qtz = quartz. Photograph locations are shown on Fig. 5. ........................................................................ 67

Figure 7: Map of the central domain with the MSS represented by the blue horizontal line pattern. Stereonet plots of poles to foliation, shear zone, conjugate shear fractures, and veins. Number of measurement (n=) and average orientation of structural feature to the lower right of the stereonet plots. Contours are in intervals of 2% of the total data points per 1% area of stereonet. UTM coordinates NAD83 Zone 15N. LCV, laminated crustiform veins; HBV, hydrothermal breccia veins; QCC, quartz chlorite carbonate veins; SRV, sulfide-rich veins...... 69

Figure 8: Map and field photographs of outcrop #3. See Figure 7 for location of outcrop. a) Detailed map of outcrops #3. Map shows dip-slip (blue lines) and sinistral strike-slip (red line) shear zones located in-between two strong lineaments representing major shear zones. UTM coordinates NAD83 Zone 15N. Location of field photographs 8b, 8c, 8d shown on map. b) S-fabric (S) dragged along sinistral shear bands (C’) in sheared mafic dike. Pencil (15.4 cm in length) for scale; c) Dip-parallel slickenline (red arrow) along the wall of a shallowly-dipping vein.d) Shallowly-dipping vein outlined by blue solid line. ....................................................... 71

Figure 9: Detailed geological map of the Hammond Reef showing which is representative of the Hammond Reef deposit.. See Figure 7 for location of outcrop. UTM coordinates NAD83 Zone 15N. Encircled numbers and letters 10a to 10d refer to field photographs shown in Figure 10. . 72

Figure 10: Field photographs from central domain. a) Laminated crustiform vein (solid blue line) with a chlorite-carbonate rich alteration halo (dashed blue line), Hammond Reef prospect. Photo card (8.5 cm in length) for scale; b) Sharp-walled hydrothermal breccia vein (solid blue line) with sericite ±carbonate alteration halo (dashed blue line). Photo card (8.5 cm in length) for scale; c) Irregular-shaped hydrothermal breccia vein with foliated fragments with the foliation represented by solid red line. Photo card (8.5 cm in length) for scale; d) Sulfide-rich vein with a sericite alteration halo. Photo card (8.5 cm in length) for scale. e) hydrothermal breccia vein surrounded by a stockwork of narrow quartz veins represented by blue lines; f) foliated fragments within hydrothermal breccia. HBV, hydrothermal breccia vein. Photograph locations are shown on Figure 9. ........................................................................................................ 74

Figure 11: Map of the northern domain showing extent and orientation of the MSS. Stereonet plots of poles to foliation, shear zones, faults, and veins. Number of measurement (n=) and average orientation of structural feature to the lower right of the stereonet plots. Contours (1% area) representing density distribution of poles to foliation, shear zone and veins forming syn-deformation at a 2% intervals. Conjugate faults are plotted as poles. UTM coordinates NAD83 Zone 15N. ........................................................................................................................ 75

Figure 12: Detailed map of the Sawbill showing (outcrop #6) with stereonet showing the average orientation of the shear vein, foliation, extensional quartz veins, and striation along the quartz vein. UTM coordinate NAD83 Zone15N. See Figure 11 for location of outcrop. ....................... 76

Figure 13: Field photographs of the Sawbill vein and outcrop in the northern domain. a) Quartz-filled dilational jog or left-stepping stepover-zone along shear zone indicating sinistral shear. Compass (10 cm in length) for scale. b) Laminated Sawbill vein. Compass (10 cm in length) for scale. c) Sub-horizontal striations along shear planes. Compass (10 cm in length) for scale. d) Sub-horizontal striations along wall of laminated Sawbill vein. Compass (10 cm in length) for scale. e) S foliation dragged in anticlockwise manner along the C-foliation indicating sinistral shearing. Compass (10 cm in length) for scale. f) Close-up of ESE-trending extensional quartz

veins with coarse quartz fibers and vuggy centers. Compass (10 cm in length) for scale. g) ESE-trending extensional quartz vein dragged in anticlockwise manner along the margin of the laminated vein. Compass (10 cm in length) for scale. h) Extensional quartz veins crosscutting laminated quartz vein. Compass (10 cm in length) for scale. Photograph location is shown on Figure 12. ........ 78

Figure 14: a) Graphic log of drill hole (BR-1060) b) 1. LCV with chlorite-carbonate alteration halo present in drill hole BR-4035, 2. QCC (solid blue line) with chlorite selvedges and sericite (±carbonate) alteration halo (outlined by the blue broken lines) overprinting a chlorite- carbonate (±sericite) altered host rock, 3. HBV within a zone of bleaching. Fragments outlined by blue broken lines, 4. Sericite (±carbonate) altered porphyritic tonalite, 5. Chlorite- carbonate (±sericite)-altered porphyritic tonalite. Modal percentage of minerals are visual estimates. Gold concentrations are from Agnico Eagle Mines Ltd. ........ 79

Figure 15: Photomicrographs of the early chlorite-carbonate (±sericite) and a late sericite (±carbonate) alteration (a) and (b) Plane polarized and cross polarized light microphotograph of porphyritic tonalite with early chlorite-carbonate (±sericite) alteration. (c) and (d) Plane polarized and cross polarized light microphotograph of a QCC vein with Fe-rich chlorite selvedges in contact with sericite altered porphyritic tonalite. (e) Sericite replacing chlorite in alteration halo of a QCC vein. Plane polarized light. (f) Close-up of (e). Plane polarized light. QCC, quartz-chlorite-carbonate vein; Chl, chlorite, qtz, quartz; ser, sericite ........ 81

Figure 16: Sericite mineral chemistry showing trends in composition along different vein types found throughout the Hammond Reef depsoit: a) Ternary diagram for potassic dioctahedral micas from the Hammond Reef deposit (after Tappert et al., 2013). $Al^{iv}$ cations apfu are plotted against Fe and Mg cations apfu calculated using 11 O. b) Binary plot of Si cations apfu versus Fe+Mg cations apfu. and c) Binary plot of Si cations apfu versus $Al^{vi}$ cations apfu. LCV, laminated crustiform veins; HBV, hydrothermal breccia veins; QCC, quartz-chlorite-carbonate veins; SRV, sulfide-rich veins; Chl-carb-ser, wider zone of chlorite-carbonate-sericite alteration on outcrop #3. Inset plots of sericite chemistry proximal (red) to distal (green) from QCC veins ........ 83

Figure 17: Chlorite and carbonate mineral chemistry showing variations in composition along vein types found throughout the Hammond Reef deposit; (a) Chlorite classification diagram after Foster (1962) calculated using 36 O. b) Ternary dolomite-ankerite-calcite diagram with Ca, Mg, Fe cations apfu calculated based on 6 O. LCV, laminated crustiform veins; HBV, hydrothermal breccia veins; QCC, quartz-chlorite-carbonate veins; SRV, sulfide-rich veins; Chl-Ser-Carb, chlorite-carbonate-sericite alteration. ........................................................................... 85

Figure 18: Binary plot of $TiO_2$ versus Zr with a R factor of 0.93 with the precursor sample shown by red solid circle.Mass balance diagrams in percent changes for distal (D835784), medial (D835783), and proximal (D835782) samples to shear zone on outcrop #3 shown on Figure 8. 88

Figure 19: Mass balance diagrams in percent changes for alteration halos associated with LCV, laminated crustiform veins; HBV, hydrothermal breccia veins; QCC, quartz chlorite carbonate veins ........................................................................................................................ 89

Figure 20: LA-ICP-MS element maps showing two generation of pyrite growth of a pyrite grain located in the alteration halo of an LCV. ........................................................................... 90

Figure 21: LA-ICP-MS element maps showing multiple generation of pyrite growth in pyrite grains associated with; a) HBV, b) QCC vein, and c) SRV. ....................................................... 91

Figure 22: In situ U-Pb monazite age of mineralization. a) Concordia diagram for monazite from the LCV, b) SEM backscattered image of analyzed monazite grain in LCV, c) Concordia diagram for monazite from the HBV, d) SEM backscatter image of analyzed monazite in alteration halo of HBV, e) Concordia diagram for monazite from the SRV, b) SEM backscatter image of analyzed monazite in SRV............................................................................... 93

Figure 23: Concordia diagram and associated images of analyzed zircons from sample MEAK21GJF0027A of the Diversion stock tonalite.................................................................... 94

# List of Appendices

Appendix A: Methodology ........................................................................................... 95

Appendix B: Sample description ................................................................................. 103

Appendix C: Whole rock geochemistry and assay analysis ...................................................... 109

Appendix D: Trace element maps.................................................................................. 117

# Chapter 1

# 1 Introduction to Thesis

## 1.1 Research Problem

The Hammond Reef deposit is a low grade high tonnage gold-only deposit located 170 km west of Thunder Bay, Ontario, in the Marmion terrane of the Wabigoon Subprovince of the Archean Superior Province (Fig. 1). The deposit is hosted by the Marmion Shear System (MSS) which straddles the contact between the late Mesoarchean Diversion stock to the west and the middle Mesoarchean Marmion Batholith to the east (Fig. 2). The MSS is a system of roughly parallel, north northeast-tending anastomosing shear zones which extends over 30 km, offsetting the 2730 - 2930 Ma Steep Rock Group to the south , and continues to the north and west of the Lumby Lake greenstone belt as the Red Paint Lake shear zone. The Hammond Reef deposit is different from other Archean orogenic gold deposits as it is hosted within a trondjemite-tonalite-granodiorite (TTG) complex rather than the adjacent greenstone belts.

Bakke (1995) suggested that Hammond Reef is an intrusion-related gold deposit similar to the Fort Knox deposit in east-central Alaska. His interpretation emphasized the association between gold, low sulfidation quartz stockwork and fracture systems, and a multi-phase intrusion complex. More recently, Backeberg (2015) re-classified Hammond Reef as a mesothermal “orogenic” gold deposit similar in age to other 2.7 Ga gold deposits in the Western Wabigoon terrane. He suggested that the deposit formed during a late phase of pure shear flattening across the MSS. This differs from current models on the formation of orogenic gold deposits, which are typically thought to form during the main phase of movement along faults and shear zones. These two contrasting interpretations and the incongruity of Backeberg's model with present thinking on the formation of orogenic gold deposits prompted the present thesis on the formation of the Hammond Reef deposit.

## 1.2 Objectives of Thesis

This thesis aims to resolve the geological, structural, and chronological controls on gold mineralization at the Hammond Reef deposit. Regional mapping along with more detailed mapping of structures and mineralization, together with geochemical and petrographic analyses of selected samples and U-Pb dating of the host intrusions and mineralization, were done to achieve this goal. The main objectives of this thesis are to:

1. Determine the structural deformation history of the MSS to provide a structural framework for the emplacement of the Hammond Reef deposit;
2. Characterize the geochemistry and mineralogy of veins and alteration mineral assemblages present at the deposit;
3. Provide chronological constraints on the formation of the deposit;
4. Suggest an interpretation and model for the formation of the Hammond Reef deposit.

## 1.3 Structure of Thesis

This thesis is written as two separate chapters. Chapter 1 provides an introduction to the thesis and establishes the research problem, objectives, and structure of the thesis.

Chapter 2 is written as a manuscript for submission to a scientific journal. It is entitled: "*The Archean Hammond Reef deposit: the formation of an orogenic gold deposit in a contractional step-over-zone along a major strike-slip fault system*". Co-authors on this publication are:

- Lafrance, B., Mineral Exploration Research Centre, Harquail School of Earth Sciences, Laurentian University, 935 Ramsey Lake Road, Sudbury, Ontario, P3E 2C6, Canada
- Marsh, J., Mineral Exploration Research Centre, Harquail School of Earth Sciences, Laurentian University, 935 Ramsey Lake Road, Sudbury, Ontario, P3E 2C6, Canada
- Hamilton, M., Jack Satterly Geochronology Research Laboratory, University of Toronto, Toronto, Ontario, M5S 3B1, Canada

Additional information collected during the research is included in appendices. **Appendix A** describes mapping and analytical techniques used in the thesis. **Appendix B** provides petrographic description of thin sections. **Appendix C** lists whole rock geochemical analytical and assay results. **Appendix D** includes LA-ICP-MS element maps of pyrite grains hosted in mineralized veins.

# Chapter 2

# 2 The Archean Hammond Reef deposit: the formation of an orogenic gold deposit in a contractional step-over-zone along a major strike-slip fault system

## 2.1 Introduction

Gold deposits form in low porosity and low permeability host rocks through fracture-controlled flow of hydrothermal fluids. As a result, dilation along and around major faults and shear zones are key features in forming ore deposits. The formation of dilational zones requires dynamic coupling between stress states, fluid pressure, fluid flow and deformation processes. The deformation processes are often controlled by geometry, displacement, and style of fracture-related permeability. Fault termination zones, fault bends and segment linkage zones are important dilational sites for the formation of all hydrothermal ore deposits, including gold deposits (Micklethwaite and Cox, 2006; Micklethwaite et al., 2010; Cox, 2020).

The Hammond Reef gold deposit is one of few excellent examples of an orogenic gold deposit forming in a contractional step-over-zone between two major transcurrent shear zones along a major shear system called the Marmion Shear System (MSS). In this paper, we: (1) Describe the orientation and style of structural features along the MSS; (2) Characterize the mineralogy and geochemistry of the veins and alteration haloes that make up the Hammond Reef deposit; (3) Provide U-Pb monazite age constraints on the formation of the deposit and compare the chronology of the deposit with that of deformation events and other gold deposits in the Wabigoon subprovince ; (4) Propose a model for the emplacement of the Hammond Reef deposit along a step-over-zone between major transcurrent faults; (5) Discuss how step-over-zones may localize the flow of hydrothermal fluids and the formation of orogenic gold deposits.

## 2.2 Regional Geology

The Superior Province is one of the world's largest exposed Archean cratons. It is characterised by fault-bounded subprovinces with distinct geochemical signatures, structures, ages, and metamorphic facies conditions (Thurston, 1991). These subprovinces were amalgamated together between 2.72 to 2.68 Ga during the Kenoran orogeny (Thurston, 1991; Tomlinson et al., 2003; Percival, 2007a). The Wabigoon subprovince is an east-west trending, 900 km long by 150 km wide, granite-greenstone belt located in the northwest Superior Province. It consists of metamorphosed volcanic rocks, sedimentary rocks, granitoid batholiths, stocks and gabbroic sills ranging in age from 3.00 to 2.69 Ga (Blackburn et al., 1991). It is fault-bounded against the metasedimentary English River subprovince to the north and metasedimentary Quetico subprovince to the south (Fig. 1). The Wabigoon subprovince has been further divided into the Winnipeg River, Marmion, eastern Wabigoon, and western Wabigoon terranes based on the U-Pb age and Nd isotopic composition of volcanic and associated plutonic rocks (Tomlinson et al., 2003). These terranes were amalgamated together during the Mesoarchean at around 2.92 Ga and were joined and/or overthrusted by Neoarchean volcanic rocks of the eastern and western Wabigoon terranes at ca. 2.70 Ga (Tomlinson et al., 2003; Percival & Helmstaedt, 2004; Tomlinson et al., 2004; Percival, 2007a; Ma et al., 2021).

The western Wabigoon terrane is dominated by tholeiitic to calc-alkaline metavolcanic rocks and large tonalitic plutons (Percival, 2007b). The juvenile Nd isotopic composition of the metavolcanic rocks suggest the western Wabigoon was juxtaposed to the Winnipeg River terrane at ca. 2712 Ma (Davis and Smith, 1991; Ayer and Dostal, 2000; Tomlinson et al., 2003). The Marmion terrane (Fig. 1) mainly consists of trondjemite-tonalite-granodiorite (TTG) intrusions surrounded by narrow greenstone belts. The Marmion Batholith forms an elongated tonalitic body located in the western to central portion of the Marmion terrane. It is a medium- to coarse-grained, biotite-rich, massive to gneissic, dioritic to granodioritic, multiphase body with a reported age of ca. 3.00 Ga (Davis & Jackson, 1988; Tomlinson et al., 2003; Stone, 2008). It is bounded by the Steep Rock and Finlayson greenstone belts to the west and extends eastwards for about 100 km in-between the ca. 2.96 - 3.10 Ga Lumby Lake greenstone belt to the north (Davis and Jackson, 1988; Tomlinson et al., 2003) and the Quetico fault zone to the south, where it is in contact with the metasedimentary Quetico subprovince (Fig. 2). The Steep Rock greenstone belt is dated at 2.73 - 2.93 Ga (Stone, 2008) and it unconformably overlies the Marmion Batholith (Tomlinson et al., 2003). The contact between the ca. 2.93 to 3.00 Ga Finlayson Lake greenstone belt and the Marmion Batholith is obscured by younger tonalitic intrusions (Stone and Kamineni, 1989; Tomlinson et al., 2003; Stone, 2010), including the tonalitic Diversion stock which vary in age between 2780 Ma to 2893 Ma (Buse et al., 2010; Bjorkman et al., 2017). The Diversion stock differs from the Marmion tonalites by its magmatic texture of interlocked quartz, feldspar, and hornblende (Stone, 2008; Backeberg, 2016).

The MSS straddles the Diversion stock and western margin of the Marmion Batholith. It is a 3 km wide system of anastomosing northeast-trending shear zones and faults, which extends over 30 km from the western margin of the Lumby Lake greenstone belt to the northeast, where it merges with the Red Paint Lake shear zone, to the Steep Rock greenstone belt to the south, where it offsets the Steep Rock – Marmion Batholith unconformity and is dragged along the Quetico fault zone as shown on the geological map of Stone (2008).

**Deposit Geology**

The Hammond Reef deposit is a low grade high tonnage gold only deposit with a measured and indicated resources estimate of 3.3 Moz of gold (Osisko, 2013). The deposit consists of porphyritic tonalite, fine grained tonalite and gneissic tonalite, other rock types include pegmatites and mafic dykes. All lithologies are locally foliated along meter wide shear zones which define the MSS. Gold mineralization is associated with auriferous quartz-carbonate veins and occurs as free gold along pyrite aggregate grain boundaries, healed fractures or inclusions in pyrite (Kolb, 2010; Osisko, 2013; Backeberg, 2015).

## 2.3 Methodology

Analytical methods are briefly described below, and detailed descriptions are provided in Appendix A.

*Petrography (optical and scanning electron microscope)*

A total of eighty-three samples of veins, alterations, lithologies, and structures were selected for optical petrographical work. Grab, channel, and drill core samples were collected across the MSS, with a focus on the Hammond Reef deposit. Billets of those samples were sent to Vancouver Petrographic for polished thin sections. A subset of these samples was further characterized using a Tescan Vega 3 – LMH scanning electron microscope (SEM) housed at Laurentian University. The SEM is equipped with a tungsten filament and a Bruker Flash 6 – 60 $mm^2$ energy dispersive spectrometer (EDS) detector. A working distance of 15 mm, a beam intensity of 15 – 16 nA, and accelerating voltage of 15kV were used to collect semi-quantitative mineral chemical data. Semi-quantitative data was collected using a SEM-EDS instrument and detector at Laurentian University. Internal standards were used to ensure data accuracy: pyrope (NMNH 143968) was selected to monitor $SiO_2$, $Al_2O_3$, FeO, MgO, CaO, $TiO_2$, MnO values (Jarosewich et al., 1972, 1980), and microcline (NMNH 143966) was selected to monitor $K_2O$ and $Na_2O$ values (Jarosewich et al., 1980).

### *Whole rock geochemistry*

Fifty-five samples were submitted for whole rock major and trace element geochemistry at ALS Canada Ltd. in Sudbury, Ontario (2021). Major elements were digested by metaborate fusion and analyzed by inductive coupled plasma emission spectrometry (ICP). Base metals Cd, Co, Cu, Mo, Ni, Pb, Sc, Zn, Ag, and Li were analyzed using four acid digestion ICP. Trace elements (Ba, Ce, Cr, Cs, Dy, Er, Eu, Ga, Gd, Hf, Ho, La, Lu, Nb, Nd, Pr, Rb, Sm, Sn, Sr, Ta, Tb, Th, Tm U, V, W, Y, Yb, Zr) were digested by metaborate fusion and analyzed by inductive coupled plasma emission mass spectrometry (ICP-MS). Concentration of S and C were analyzed by combustion using a Leco™ induction furnace. Precision and accuracy were better than 10%, for major elements, REE’s, and other trace metals except for analyses close to detection limits. The samples were further assayed for their Au and Ag content. They underwent four acid digestion, and an aliquot of these solutions were analyzed for Ag by atomic absorption spectroscopy (AAS), Au was analyzed by fire assay with an ICP instrumental finish. This work was done to characterize the geochemical footprint of the Hammond Reef deposit.

### *Trace element maps*

Five pyrite grains from different generation of veins were analyzed in-situ using the Thermo X Series II inductive coupled plasma mass spectrometer (ICP-MS) at the Chemical Fingerprinting Laboratory, Laurentian University, Sudbury, Ontario. Laser ablation sampling was performed using a Photon Machines Analyte G2 ArF excimer laser, with 193 nm wavelength, 5 ns pulse width, and HelEx II cell. Laterally contiguous line traverses were ablated with laser fluence of 4 J/cm$^2$, 30 Hz repetition rate, and 5 - 10 µm spot size. Data was processed using Iolite v4, with a baseline subtraction, instrumental drift correction, and concentration normalization performed with the Trace Element – Internal Standard reduction scheme (Paton et al., 2011; Petrus & Kamber, 2012). These analyses were completed to characterize the trace metals and other elements associated with sulfide minerals in mineralized zone of the Hammond Reef deposit.

### *In-situ U-Pb monazite*

Three samples from various veins were analyzed for in-situ monazite U-Th-Pb isotopic geochronology. The samples were analyzed using a Thermo Scientific Neptune Plus multicollector (MC) ICP-MS at the Mineral Exploration Research Centre - Isotope Geochemistry Lab (MERC-IGL) at Laurentian University, Sudbury, Ontario. Laser ablation sampling was performed using a Photon Machines Analyte G2 ArF excimer laser, with 193 nm wavelength, <5 ns pulse width, and HelEx II cell. The raw U-Th-Pb data were processed in Iolite v4, with baseline subtraction, instrumental drift, and downhole fractionation corrections performed with the U-Pb geochronology data reduction scheme (Petrus & Kamber, 2012). These analyses were conducted to constrain the timing of mineralization at the Hammond Reef deposit.

### *TIMS*

One sample of the Diversion stock was selected to undergo isotope dilution thermal ionization mass spectrometry (ID-TIMS) at the Jack Satterly Geochronology Research Laboratory, University of Toronto, Toronto, Ontario. The samples were crushed, ground and initial separation of heavy minerals was achieved by passing the heavy concentrate over a shaking, riffled water (Wilfley$^{TM}$) table multiple times. Further processing included density separations with methylene iodide and paramagnetic separations with a Frantz isodynamic separator. The final zircons analyzed were handpicked in alcohol under a binocular microscope. Analytical methods involved isotope dilution thermal ionization mass spectrometry (ID-TIMS) following chemical abrasion (CA, modified after Mattinson, 2005).

## 2.4 Results

### 2.4.1 Marmion Shear System

The MSS is divided into three structural domains based on the orientation of the shear zones; a southern domain trending north-northeast (NNE), a central domain trending east-northeast (ENE), and a northern domain trending north-northeast (NNE).

**Southern domain**

The southern domain extends over 15 km from the Steep Rock-Marmion unconformity to the south, to an inflection point to the north, where the shear zones change in orientation from NNE-trending in the southern domain to ENE-trending in the central domain (Fig. 3). The shear zones are well exposed along the shoreline of Marmion Lake. They initiated as zones of closely spaced fractures as exemplified on Gold Mine Island, which is located in Marmion Lake approximately 16 km NNE of the town of Atikokan. Historic gold mining on this 1.5 km$^2$ island began in 1948 by Plator Gralouise Gold Mines Limited and ended in 1966 due to a breach of mining regulations (Wilkinson, 1982). Zones of closely spaced fractures, trending 030°, are present near the old mine workings, where they cut across tonalite of the Marmion Batholith

(Fig. 4a). The fractures are spaced 5 to 10 cm apart and are surrounded by 1 to 5 cm wide, bleached, sericitic alteration halos (Fig. 4b). A second set of sericitic fractures trends 120° - 130°. Quartz veins bisect the angle between the two fracture sets (Fig. 4c). Their orientation and geometry suggest that they were emplaced along tensile fractures during NNW-directed compression and formation of a conjugate shear fracture set represented by the 030° and 120° fractures. Increased fluid flow along the dominant 030° fractures resulted in more intense sericite alteration, reaction strain softening, and the formation of a sericitic foliation during ductile shear along the fractures (Fig. 4d). The orientation (060°) and anticlockwise dragging of the foliation suggest sinistral shear along the brittle and sericite-filled 030° fractures and shear zones during NNW-directed compression.

Sinistral shear sense indicators are present along several sericitic, NNE-trending (030°), shear zones along the shoreline and on islands in the Marmion Lake. Outcrop #5, which is located at the north end of the southern domain (Fig. 3), exposes a 1.5 metre wide shear zone with a central 1 metre thick quartz vein (Fig. 5). The shear zone strikes 030° and cuts across three tonalitic rock units differing in grain size and relative abundance of plagioclase phenocrysts. The three tonalitic units are variably altered to sericite and carbonate with the intensity of the alteration increasing towards the quartz vein. Altered tonalite on both sides of the vein have a pronounced sericitic foliation, striking 060° and dipping steeply to the south. It rotates in anticlockwise manner along the vein contact suggesting sinistral shear (Fig. 6a). The presence of sinistral shear bands, S-shaped drag folds (Fig. 6b), boudinaged NNE-striking minor quartz veins, and folded NNW-striking quartz veins adjacent to the central vein, further suggest sinistral transcurrent slip along the shear zone. The central vein contains 1 to 5 cm in size, sub-angular, foliated fragments (Fig. 6c). The presence of these foliated fragments suggest that the shear zone did not nucleate on an older vein and its mechanically weak alteration halo. Instead, the central vein was emplaced during sinistral shearing and formation of the foliation.

The foliated tonalites consist of primary quartz, plagioclase, and biotite, altered to sericite. Primary quartz porphyroclasts have irregular grain boundaries with smaller recrystallized quartz along transgranular microfractures. Subgrains within and along the margins of the porphyroclasts have an average size of 100 - 150 µm, and exhibit internal undulose extinction and low-angle boundaries (Fig. 6d). Primary plagioclase porphyroclasts are partially recrystallized along their margin. They have irregular grain boundaries and an average size of 100 µm, and exhibit internal undulose extinction, low-angle boundaries, kink bands, and microfractures that span the width of the grains (Fig. 6e). A muscovite sigmoidal mica fish is partially replaced at both ends by foliation-parallel sericite (Fig. 6f). Its asymmetry suggests sinistral shear consistent with kinematic indicators observed on outcrop.

### Central domain

The central domain hosts the Hammond Reef deposit. It covers an ENE-trending segment of the Marmion shear zone, which is exposed over 3 km along strike across a peninsula extending into Marmion Lake (Fig. 7). The Marmion shear zone strikes parallel to the north shore of the small Mitta Lake in the center of the peninsula. Its southern boundary is located along the shoreline of Mitta Lake and its northern boundary is located 300 m to the north and is well exposed along the shoreline of Marmion Lake. Both boundaries are marked by 5 m wide shear zones separating a wider lower strain domain characterized by a weak foliation, conjugate shear fractures, and fewer narrow shear zones.

Stripped outcrop #3 is located in-between the two bounding shear zones shown as lineaments in red in Figure 8. The shear zone along the southern end of the outcrop is partially exposed and defined by a pronounced foliation and strong sericite (±carbonate) alteration. The shear zone to the north was delineated by Osisko in 2010 and is exposed to the east along the shoreline of Marmion Lake. Within the low strain domain located in-between the two major bounding shear zones, minor dip-slip and sinistral strike-slip shear zones are exposed. Within a sheared mafic dyke, a S-foliation is dragged in anticlockwise manner along C‘ shear bands indicating sinistral strike-slip movement (Fig. 8b). Near the south end of the outcrop, shallowly dipping veins strike ENE (060°) and dip 40° to the SSE. Slickenlines are present along the upper and lower surfaces of these veins and are parallel to the dip of the veins (Fig. 8c). The veins have minimum thicknesses of 5 cm; their true thicknesses cannot be determined because the veins dip parallel to the sloping surface of the outcrop and are weathered and eroded revealing the host rocks below the veins (Fig. 8d). In low strain domains in between shear zones, the foliation is less pronounced and late conjugate sinistral NE-trending shear fractures and dextral NW-striking shear fractures are present indicating a NNW shortening direction.

The main Hammond Reef Mine showing is located 1 km east of Mitta Lake and is represented by outcrop #2 in Figure 9. It consists of fine-grained and porphyritic tonalite cut by pegmatite dykes within a low strain domain (Fig. 9). Excellent cross-cutting relationships between different vein types are present on the outcrop. The vuggy and laminated crustiform veins (LCV), varying in width from 1 cm to 5 cm, consist of quartz and carbonate and are surrounded by roughly 3 cm wide alteration halos of chlorite, carbonate, and pyrite. The veins are folded, and their alteration halo is overprinted by a foliation, striking 060° parallel to the fold axial planes. They are offset along sharp-walled breccia veins, striking 060° (Fig. 9). The sharp-walled breccia veins are generally 5 to 10 cm wide with 5 cm wide sericite alteration halos. The sharp-walled breccia contain sub-angular to rounded, foliated, wall rock fragments with an average size of 1 to 2 cm. Irregular-shaped hydrothermal breccias occupy the southern part of the outcrop. The breccias formed along the contact between fine grained tonalite and porphyritic tonalite. The clasts have a jigsaw fit texture and range in size from 1 to 50 cm. They are strongly altered to sericite and contain a foliation striking 060º. Sulfide-rich veins cut across the hydrothermal breccia veins. The sulfide veins are 1 to 5 cm thick and consist of 30 - 40% (1 – 5 mm) cubic pyrite surrounded by a matrix of quartz and carbonate (ankerite and calcite), with 5 cm wide sericitic alteration halos (Fig. 9). These veins are undeformed, steeply dipping, and ENE-striking.

Excellent examples of irregular-shaped hydrothermal breccias are present on an outcrop located 200 m west of Mitta Lake. The hydrothermal breccias are hosted by tonalite which is locally foliated but contains no shear zone (Fig.10a). The breccias range in size from a few meters to 10s of meters and only contain clasts of the host tonalite altered to sericite and subordinate carbonate with trace pyrite and chalcopyrite. The clasts are angular with a jigsaw fit texture. They contain a strong to moderate foliation, which strikes 060º and is parallel to the foliation overprinting the host rocks. The same foliation is axial planar to folds locally overprinting the breccias (Fig. 10b).

## Northern domain

The Northern domain extends for 6 km north of the central domain (Fig. 11). Shear zones within the northern domain have a similar NNE trend as those within the southern domain. The Sawbill mine prospect (Fig. 12) shows the relationships between a shear zone, foliation, and quartz veins. The prospect consists of the Sawbill laminated vein, within a 5 metre wide shear zone that can be traced continuously over 100 metres across a mechanically stripped outcrop. The Sawbill vein produced 1342 ounces of Au from 1897 to 1899 and from 1940 to 1941 (Tremblay, 1940; Ferguson et al., 1971). The shear zone and vein cut across porphyritic tonalite, fine-grained tonalite, and late mafic dikes and pegmatite. These rocks are strongly altered to sericite (±carbonate) within the shear zone. The laminated quartz vein and host shear zone are steeply-dipping and NNE-trending. The laminated quartz vein is typically 1 m to 2 m thick, but it thickens to 3 m within left-stepping jogs (Fig. 13a). Laminae within the vein have a spacing of 1 cm to 5 cm, are parallel to the trend of the vein and shear zone, and are defined by sericite altered host rocks (Fig. 13b). They are striated by a sub-horizontal lineation expressed as ridge-and-groove corrugations (Fig. 13c,d). The shear zone has an internal, ENE-striking (040°) and steeply-dipping, sericitic foliation, which is oriented oblique and clockwise to the trend of the shear zone and laminated vein. It is dragged in anticlockwise manner next to the vein and shear bands (Fig. 13e). Narrow, cm-wide veins, striking 110° and dipping 72°, are oriented oblique and anticlockwise to the laminated vein. They have internal euhedral comb textures, vuggy centers, and wedge-shaped tips (Fig. 13f), and can be traced from the undeformed wallrocks of the shear zone into the shear zone where they undergo anticlockwise rotations (Fig. 13g). Some are truncated by the laminated vein while others cut across the laminated vein (Fig. 13h). These mutually overprinting relationships suggest that they are coeval with the formation of the laminated vein. Two sets of late fractures are subvertical and trend 063º and 010º, which is consistent with their formation as conjugate shear fractures during NNW-directed shortening.

### 2.4.2 Alteration and Mineralization

Detailed mapping, core logging, petrographic analysis, mineral chemistry, and LA-ICP-MS trace element sulfide maps reveal two distinct alteration assemblages: an early chlorite-carbonate (±sericite) alteration assemblage and a later sericite (±carbonate) alteration assemblage. They are described below.

*Chlorite - carbonate (±sericite) rich alteration*

Early chlorite-carbonate (±sericite) rich alteration is present in all tonalitic intrusions including the Marmion and Diversion stock tonalites. It increases in intensity in the wallrocks of the LCV (drill core #1 and #5 in Fig. 14b). In thin section, primary biotite and amphibole grains are replaced by chlorite ±rutile, and plagioclase grains are partially to completely replaced by fine-grained sericite and carbonate (Figs. 15a). The latter also occurs along grain boundaries of primary minerals. Chlorite has a vibrant blue colour in cross polarized light suggesting a Mg-rich composition (Fig. 15a). Disseminated titanite is associated with sericite within strongly altered plagioclase grains. Cubic pyrite with inclusion-rich centers and minor chalcopyrite are present within the alteration halos of LCV.

*Sericite (±carbonate) rich alteration*

Up to 40 cm wide alteration haloes of sericite (±carbonate) surround quartz-chlorite-carbonate veins (QCC), hydrothermal breccia veins (HBV), and sulfide rich veins (SRV) (drill core #2, #3, and #4 in Fig. 14b). Wider zones of sericitic alteration, which are expressed as zones of pale yellow-green “bleaching”, are present in sheared tonalite and in less deformed tonalite containing multiple HBVs. In both cases, sericite replaces early chlorite after primary biotite and amphibole (Fig. 15c,d). Chlorite is also present within the QCC veins and HBV and as selvedge along the margin of the QCC veins, but it differs from the early chlorite by its deep purple colour under cross polarized light suggesting a more Fe-rich composition (Fig. 15c,d). Sericite is observed as replacing early chlorite after primary biotite and amphibole (Fig. 15e,f). Carbonate infills microfractures and grain boundaries between primary and alteration minerals. Hematite is locally present in association with magnetite and changes the colour of the bleached zones to brick red.

Pyrite is the most abundant sulfide mineral in the sericitic alteration halos and bleached zones. Pyrite cubes (1-2 mm in size) make up 1-10% of the alteration halo surrounding the QCC veins and HBV, and the SRVs contain up to 20-30% (1-5 mm) cubic pyrite. Disseminated grains of chalcopyrite and galena are present, as well as telluride micro-inclusions within pyrite grains.

The relationships between gold concentrations and alteration are shown on a representative graphic core log diagram of drill hole BR-1060, which was drilled across and below the main Hammond Reef showing (Fig. 14a). Alteration intensity is visually estimated in 5% increments. Au concentrations in part per million (ppm) are from Osisko (2010)’s assay database. The log shows increasing gold values in zones of strong sericite alteration and HBV and QCC veining.

### *Mineral chemistry*

Representative mineral chemistry of white mica, chlorite and carbonate from the early chlorite-carbonate (±sericite) alteration and sericite (±carbonate) alteration, broken down in terms of their association with the LCV, HBV, SRV, and QCC veins, are listed in Table 1 and shown in Figures 16 and 17. In addition, the chemistry of the same minerals from a wider zone of chlorite-carbonate-sericite alteration on outcrop #3, where both alteration assemblages are superposed, is presented.

**Table 1:** Summary of mineral chemistry from alteration associated with mineralized veins and alteration at the Hammond Reef deposit.

*White mica*

| Host | Description | $SiO_2$ (Wt%) | $TiO_2$ (Wt%) | $Al_2O_3$ (Wt%) | FeO (Wt%) | MnO (Wt%) | MgO (Wt%) | CaO (Wt%) | $Na_2O$ (Wt%) | $K_2O$ (Wt%) | Total | Formula | Si (apfu) | Al(iv) (apfu) | Al(vi) (apfu) | Ti (apfu) | Fe (apfu) | Mn (apfu) | Mg (apfu) | Ca (apfu) | Na (apfu) | K (apfu) | Fe/(Fe+Mg) |
|---|---|---|---|---|---|---|---|---|---|---|---|---|---|---|---|---|---|---|---|---|---|---|---|
| LCV | 07AG02A,n=58; 02AG04, n=44 | 44.99 | 0.64 | 32.09 | 4.51 | 0.01 | 0.87 | 0 | 0.36 | 11.18 | 94.01 | 11O | 6.18 | 1.82 | 3.37 | 0.07 | 0.52 | 0.00 | 0.18 | 0.00 | 0.10 | 1.96 | 0.74 |
| HBV | 05AG01, n=66; 87AG02, n=71; 88AG03, n=40 | 45.71 | 0.09 | 33.43 | 3.31 | 0.48 | 0.66 | 0.00 | 0.39 | 10.90 | 94.32 | | 6.20 | 1.80 | 3.55 | 0.01 | 0.38 | 0.06 | 0.13 | 0.00 | 0.10 | 1.89 | 0.74 |
| QCC | 01AG01A, n=63; 01AG04, n=34; 01AG05, n=30 | 46.05 | 0.24 | 31.36 | 4.09 | 0.32 | 1.22 | 0.00 | 0.42 | 10.98 | 94.03 | | 6.30 | 1.70 | 3.36 | 0.02 | 0.47 | 0.04 | 0.25 | 0.00 | 0.11 | 1.92 | 0.65 |
| SRV | 07AG05, n=109; 02AG06, n=82 | 45.87 | 0.84 | 32.19 | 4.61 | 0.00 | 0.98 | 0.00 | 0.04 | 10.24 | 94.12 | | 6.24 | 1.76 | 3.40 | 0.09 | 0.52 | 0.00 | 0.20 | 0.00 | 0.01 | 1.78 | 0.72 |
| Chl-Carb-Ser | 86AG04, n=22; 87AG03, n=64; 98AG03, n=25 | 48.44 | 0.07 | 29.81 | 4.26 | 0.12 | 1.34 | 0.01 | 0.40 | 10.20 | 94.00 | | 6.57 | 1.43 | 3.33 | 0.01 | 0.48 | 0.01 | 0.27 | 0.00 | 0.11 | 1.76 | 0.64 |

*Chlorite*

| Host | Description | $SiO_2$ (Wt%) | $TiO_2$ (Wt%) | $Al_2O_3$ (Wt%) | FeO (Wt%) | MnO (Wt%) | MgO (Wt%) | CaO (Wt%) | $Na_2O$ (Wt%) | $K_2O$ (Wt%) | Total | Formula | Si (apfu) | Al(iv) (apfu) | Al(vi) (apfu) | Ti (apfu) | Fe (apfu) | Mn (apfu) | Mg (apfu) | Ca (apfu) | Na (apfu) | K (apfu) | Fe/(Fe+Mg) |
|---|---|---|---|---|---|---|---|---|---|---|---|---|---|---|---|---|---|---|---|---|---|---|---|
| LCV | 91AG02, n=99; 02AG04, n=101 | 27.03 | 0.06 | 19.83 | 23.78 | 0.00 | 17.39 | 0.15 | 0.07 | 0.00 | 88.31 | 36O | 5.59 | 2.41 | 2.43 | 0.01 | 4.10 | 0.00 | 5.36 | 0.03 | 0.06 | 0.00 | 0.43 |
| QCC | 01AG01A, n=140 | 23.63 | 0.12 | 21.20 | 33.99 | 0.41 | 9.23 | 0.05 | 0.20 | 0.00 | 88.83 | | 5.15 | 2.85 | 2.63 | 0.02 | 6.30 | 0.08 | 3.00 | 0.01 | 0.17 | 0.00 | 0.68 |
| Chl-Carb-Ser | 87AG03, n=66; 86AG04, n=134; 98AG03, n=73 | 25.69 | 0.20 | 21.53 | 28.31 | 0.36 | 12.15 | 0.16 | 0.12 | 0.07 | 88.58 | | 5.42 | 2.58 | 2.80 | 0.03 | 4.87 | 0.06 | 3.82 | 0.04 | 0.10 | 0.04 | 0.57 |

Table 1: Continued.

*Carbonates*

| Host | Description | MgO (Wt%) | CaO (Wt%) | MnO (Wt%) | FeO (Wt%) | Total | Formula | Ca (apfu) | Mg (apfu) | Mn (apfu) | Fe (apfu) |
|---|---|---|---|---|---|---|---|---|---|---|---|
| LCV | 91AG02, n=84 | 16.27 | 29.72 | 0.16 | 9.83 | 55.99 | 6O | 49.40 | 37.63 | 0.21 | 12.75 |
| HBV | 01AG10, n=116; 05AG01, n=37; 88AG03, n=64 | 0.02 | 54.62 | 0.06 | 1.05 | 55.75 | | 98.39 | 0.05 | 0.08 | 1.48 |
| | | 7.84 | 27.17 | 0.72 | 18.55 | 54.29 | | 51.13 | 20.52 | 1.07 | 27.25 |
| QCC | 01AG01A, n=14;01AG04, n=79; 98AG04, n=84 | 0.02 | 53.29 | 0.00 | 0.06 | 53.37 | | 99.86 | 0.04 | 0.00 | 0.09 |
| | | 7.59 | 26.22 | 0.98 | 18.31 | 53.10 | | 50.58 | 20.36 | 1.50 | 27.56 |
| SRV | 07AG05, n=25; 02AG06, n=87 | 0.22 | 55.38 | 0.00 | 0.19 | 55.79 | | 99.18 | 0.56 | 0.00 | 0.26 |
| | | 8.37 | 27.31 | 0.76 | 18.54 | 54.99 | | 50.55 | 21.55 | 1.11 | 26.78 |
| Chl-Carb-Ser | 86AG04, n=29; 87AG03, n=76; 98AG03, n=92 | 0.02 | 53.83 | 0.00 | 0.21 | 54.07 | | 99.63 | 0.06 | 0.00 | 0.31 |

**Notes***:* LCV, Laminated crustiform vein; HBV, Hydrothermal breccia vein; QCC, Quartz chlorite carbonate vein; SRV, Sulfide rich vein; Chl-Carb-Ser, Chlorite-carbonate (±sericite) alteration; n, number of spot analysis; Wt%, weight percent; apfu, atoms per formula unit.

Sericite mineral chemistry is shown on the $Al^{iv}$-Fe-Mg ternary diagram of Tappert et al. (2013) (Fig. 16a). The diagram plots the relative percentage of Al, Mg, Fe cations occupying octahedral sites in the sericite mineral structure. Their value is in atoms per formula unit (apfu) calculated based on 11 oxygens. Sericite has a consistent Mg : Fe ratio of 0.1 and variable $Al^{vi}$ content of 45 apfu to 90 apfu for all vein types. Except for the QCC veins where $Al^{iv}$ content in sericite becomes slightly more aluminous with increasing proximity to the veins, no trend is observed in sericite composition for the other veins. Binary diagrams of Fe+Mg versus Si and $Al^{vi}$ versus Si show similar trends with decreasing Fe + Mg content and increasing $Al^{vi}$ content with increasing proximity to the QCC veins (Fig. 16b).

Chlorite compositions are plotted on the chlorite classification diagram (Fig. 17a) of Fosters (1962). The binary diagram plot Fe/Fe+Mg apfu ratio against Si apfu, calculated based on 36 oxygens. The plot shows several clusters of chlorite compositions. Chlorite associated with the LCV plots mainly within the clinochlore and ripidolite fields and overlaps with the composition of chlorite from the wider zone of chlorite-carbonate-sericite alteration on outcrop #3. Chlorite from the QCC veins and their selvedges are more Fe-rich and plots within the ripidolite field.

Carbonate mineral compositions are shown on a dolomite-ankerite-calcite ternary diagram (Fig. 17b). Cations Ca, Mg, Fe apfu are calculated based on 6 oxygen. Ankerite is present in altered wallrocks of all vein types. Ankerite associated with the LCV has a higher Mg composition than that of the HBV and SRV. Calcite is present in altered wallrocks of QCC veins only.

### *Mass Balance*

The MacLean (1990) method is used to calculate the mass gains and losses during alteration associated with deformation and veining. Table 2 lists the whole rock major and trace element composition of representative samples used for these calculations. Three porphyritic tonalite samples were collected from the wider zone of chlorite-carbonate-sericite alteration on outcrops #3 (Fig. 8) at increasing distances from a prominent shear zone along the southern end of these outcrops. Proximal sample D835782 is located within the sericitized wallrocks of the shear zone, and medial and distal samples D835783 and D835784 are located 20 m and 40 m, respectively, north of the shear zone (see Figure 8 for sample location). Samples of LCV, HBV, and QCC alteration halos were collected from drill core. Zr was chosen as the immobile element for calculating enrichment factors as it has the highest linear regression R squared factors on binary plots of Zr versus $TiO_2$ ($R^2 = 0.9$; Fig. 18), $Al_2O_3$ ($R^2 = 0.89$), and Y ($R^2 = 0.9$). A least altered porphyritic tonalite precursor was selected using the following criteria: <5% loss of ignition, >1% Na2O, <10 on the Spitz-Darling alteration index (Spitz and Darling, 1978), between 15-85 on the chlorite-carbonate-pyrite index (Large et al., 2001), between 20-65 on the Hashimoto index (Ishikawa et al., 1976), and <1% on the sericite index (Saeki and Date, 1980).

**Table 2:** Whole rock major elements (wt. %) and trace elements (ppm) of representative samples of altered and precursor porphyritic tonalite.

| **Sample No.** | | **D835782** | **D835783** | **D835784** | **D835777** | **D835787** | **D835753** | **D835807** |
|---|---|---|---|---|---|---|---|---|
| **Vein Association** | | - | - | - | LCV | HBV | QCC | Precursor |
| **Alteration** | | Strong | Median | Weak | Strong | Strong | Strong | Weak |
| **Easting** | | 611928 | 611928 | 611928 | 612829 | 613714 | 611959 | 617166 |
| **Northing** | | 5421486 | 5421486 | 5421486 | 5421786 | 5422237 | 5420959 | 5422019 |
| Major oxides | Method | | | | | | | |
| SiO2_% | FUS-ICP | 77.60 | 76.20 | 72.87 | 88.74 | 71.29 | 71.41 | 73.32 |
| Al2O3_% | FUS-ICP | 12.77 | 12.87 | 13.46 | 5.89 | 12.49 | 16.14 | 13.76 |
| Fe2O3_% | FUS-ICP | 1.60 | 2.85 | 1.68 | 1.40 | 3.12 | 1.78 | 2.01 |
| CaO_% | FUS-ICP | 0.18 | 0.07 | 2.81 | 0.08 | 2.79 | 0.98 | 2.07 |
| MgO_% | FUS-ICP | 0.23 | 0.41 | 0.46 | 0.11 | 0.73 | 0.36 | 0.49 |
| Na2O_% | FUS-ICP | 4.19 | 2.14 | 4.97 | 2.06 | 2.45 | 3.61 | 3.69 |
| K2O_% | FUS-ICP | 2.07 | 3.27 | 0.70 | 0.89 | 2.60 | 3.34 | 1.64 |
| TiO2_% | FUS-ICP | 0.14 | 0.23 | 0.21 | 0.09 | 0.27 | 0.14 | 0.18 |
| MnO_% | FUS-ICP | 0.02 | 0.03 | 0.02 | 0.02 | 0.05 | 0.02 | 0.02 |
| P2O5_% | FUS-ICP | 0.05 | 0.06 | 0.07 | 0.02 | 0.12 | 0.04 | 0.06 |
| LOI_% | FUS-ICP | 1.09 | 1.81 | 2.69 | 0.68 | 4.01 | 2.06 | 2.69 |
| Total | | 99.94 | 99.92 | 99.96 | 99.97 | 99.92 | 99.88 | 99.93 |
| C_% | LECO | 0.03 | 0.04 | 0.46 | 0.05 | 0.78 | 0.22 | 0.4 |
| S_% | LECO | 0.02 | 0.13 | 0.01 | 0.02 | 0.08 | 0.05 | 0.02 |
| Trace elements | Method | | | | | | | |
| Au_ppm | INAA | 0.002 | 1.065 | 0.003 | 0.003 | 0.084 | 0.082 | <LOD |
| Ag_ppm | AR-MS | 0.02 | 0.4 | 0.2 | 0.02 | 0.02 | 0.02 | 0.02 |
| Ba_ppm | FUS-MS | 354.0 | 586 | 125.0 | 162 | 464 | 918 | 400 |
| Ce_ppm | FUS-MS | 46.3 | 97.6 | 42.9 | 28.7 | 69.8 | 37.6 | 46.4 |
| Cr_ppm | FUS-MS | 20.00 | 30 | 20.00 | 60 | 40 | 30 | 50 |
| Eu_ppm | FUS-MS | 0.44 | 0.73 | 0.79 | 0.38 | 0.86 | 0.55 | 0.73 |
| Gd_ppm | FUS-MS | 1.1 | 1.83 | 1.88 | 1.19 | 3.57 | 1.9 | 2.7 |
| La_ppm | FUS-MS | 26.6 | 57.1 | 20.9 | 15.100 | 34.2 | 19.3 | 24.4 |
| Lu_ppm | FUS-MS | 0.1 | 0.09 | 0.12 | 0.07 | 0.13 | 0.07 | 0.12 |
| Nb_ppm | FUS-MS | 6.8 | 9 | 8.00 | 3.2 | 7.5 | 5.5 | 6.3 |
| Nd_ppm | FUS-MS | 13.1 | 25.6 | 16.8 | 10.8 | 28.4 | 13.7 | 18.6 |
| V_ppm | FUS-MS | 18 | 38 | 17 | 18 | 29 | 15 | 17 |
| W_ppm | FUS-MS | 1 | 2 | 1 | 2 | 3 | 1 | 0.1 |
| Yb_ppm | FUS-MS | 0.59 | 0.62 | 0.68 | 0.32 | 0.93 | 0.53 | 0.71 |
| Co_ppm | TD-ICP | 2 | 4 | 3.00 | 2 | 6.00 | 2 | 4.00 |
| Cu_ppm | TD-ICP | 7 | 5 | 1 | 2 | 6 | 8 | 2.000 |
| Li_ppm | TD-ICP | 0.1 | 0.1 | 20 | 0.1 | 10 | 0.1 | 20 |

**Table 2**: continue.

| **Sample No.** | | **D835782** | **D835783** | **D835784** | **D835777** | **D835787** | **D835753** | **D835807** |
|---|---|---|---|---|---|---|---|---|
| **Vein Association** | | - | - | - | LCV | HBV | QCC | Precursor |
| **Alteration** | | Strong | Median | Weak | Strong | Strong | Strong | Weak |
| **Easting** | | 611928 | 611928 | 611928 | 612829 | 613714 | 611959 | 617166 |
| **Northing** | | 5421486 | 5421486 | 5421486 | 5421786 | 5422237 | 5420959 | 5422019 |
| Trace elements | Method | | | | | | | |
| Mo_ppm | TD-ICP | 1 | 2 | 2 | 3 | 2 | 4 | 3 |
| Ni_ppm | TD-ICP | 2.00 | 4 | 3 | 8 | 4 | 3 | 2 |
| Pb_ppm | TD-ICP | 10 | 7 | 5 | 2 | 4 | 7 | 5 |
| Zn_ppm | TD-ICP | 32 | 42 | 14 | 17 | 41 | 31 | 30 |
| As_ppm | FUS-MS | 0.3 | 0.4 | 0.3 | 0.01 | 0.4 | 0.4 | 0.1 |
| Bi_ppm | FUS-MS | 0.02 | 0.13 | 0.02 | 0.02 | 0.01 | 0.15 | 0.01 |
| Te_ppm | FUS-MS | 0.01 | 0.15 | 0.005 | 0.02 | 0.01 | 0.12 | 0.005 |
| Sr_ppm | FUS-MS | 133.00 | 55.4 | 250 | 43.8 | 116.5 | 80.2 | 235.00 |

**Notes***:* LOI, loss on ignition; FUS-ICP, lithium metaborate & tetraborate fusion ICP;
FUS-MS, lithium metaborate & tetraborate fusion FUS-MS; AR-MS, aqua regia digestion FUS-MS;
TD-ICP, total four acid digestion ICP; INAA, instrumental neutron activation analysis;
LECO, combustion by LecoTM induction furnace; <LOD, lower detection limit

Mass balance calculation results are displayed on percent mass change histograms in Figure 17 and 18. As alteration increase in intensity with increasing proximity to the shear zone, mass gains in $K_2O$, Ce, La, V, W, Cu, Ni, As, Bi, Te, S are coupled with mass losses in CaO, Li, Sr, C (Fig. 18b). The alteration halos of the HBV and QCC show similar mass gains in $K_2O$, W, Cu, Pb, As, Bi, Te, S and mass losses in Li and Sr. The alteration halo associated with the LCV differ by their mass gains in $SiO_2$ and Cr, no mass change in $K_2O$, and a strong mass loss in As (Fig. 19a).

### *Sulfide maps*

Gold is typically associated with pyrite within the sericitic alteration halo of veins and bleached zones. LA-ICP-MS element maps of pyrite grains are shown in Figures 20 and 21. Pyrite grains from the alteration halo of LCV, HBV and QCC veins are characterized by inclusion-rich domains (Py-2) and an inclusion-free domains (Py-1), and the pyrite grain in the alteration halo of SRV is entirely inclusion-free (Py-1). Py-1 in the LCV pyrite grain (Fig. 20) is characterized by compositional bands rich in Ni and bands rich in As, which are parallel to the grain crystal faces. Py-2 is characterized by Au-Ag inclusions, magnetite inclusions rich in Co, V, Mn, and other inclusions rich in Te, Sn, W, Cu, Zn. Other elements, such as Bi, Co, Pb, are enriched but more uniformly distributed. Their distribution outlines the Py-2 domains, whose irregular boundaries cut across the Ni-rich and As-rich bands in Py-1.

The HBV pyrite grain (Fig. 21a) is characterized by strongly zoned Py-1. Compositional bands are parallel to the grain crystal faces and are defined by differential enrichments in Ni, As, Co. Other elements, such as Au, Ag, Te, Bi, Pb, are strongly enriched in Py-2 and along irregular planar features (i.e. fractures) cutting across Py-1.

The QCC pyrite grain (Fig. 21b) has an internal Py-2 domain surrounded by Py-1. The latter is enriched in Ni and display, weakly-defined, Ni-rich bands. Other elements, such as Au, Ag, Te, Bi, Pb, Cr, occur in inclusions within Py-2 and along fractures cutting Py-1.

The SRV pyrite grain (Fig. 21c) differs from the other grains. It consists of several grains of unzoned Py-1 with enrichment in Ni, As, Co, Te, Bi, Pb, Cr along grain margins and transgranular fractures. Au-Ag occurs as small, isolated grains along grain boundaries.

### 2.4.3 Geochronology

*In-situ U-Pb Monazite*

Monazite associated with LCV, HBV and SRV were analyzed in-situ by LA-MC-ICP-MS at the MERC-IGL (Laurentian University). Laser spots varied in size between 10-20 µm depending on grain size (details on analytical methodology are presented in appendix A). Twenty-five grains of monazite were analyzed within the LCV and alteration halo. The grains range in size from 15-50 µm with an average size of 20 µm, they are located in association with chlorite and sericite within the alteration halo, and along quartz grain boundaries within the vein. Eighteen grains of monazite with an average grain size of 10 µm were analyzed from the sericite (±carbonate) rich alteration associated with the HBV. The grains were largely concentrated along quartz grain boundaries and within patches of sericite alteration. Finally, twelve grains of monazite with an average grain size of 20 µm from the SRV and alteration halo were analyzed. These grains occur along pyrite grain boundaries within the vein and in association with chlorite altered by sericite within the alteration halo of the vein.

Uncertainty propagation followed the method of Horstwood et al. (2016), including within-session variance from primary reference material (monazite KM03-72) analyses and uncertainty in the primary reference material age. The low long-term variance in $^{207}Pb/^{206}Pb$ ratios from in-house reference materials (i.e. MSWD<1) negated the need for further uncertainty propagation on $^{207}Pb/^{206}Pb$ weighted mean ages. Verification reference materials analyzed during each session were all reproduced within uncertainty of their accepted ages, with weighted mean ages for monazite DD90-26 = 2670 ± 1.0 Ma (n=12; MSWD = 1.03; TIMS age = 2671.1 ± 1.2 Ma; Davis, 1992). For unknown monazite grains from this study, only analyses with <5% discordance and high $Pb^*/Pb_c$, as defined from Age-U concentration relationships in each sample, are presented below.

Results from analyses with <5% discordant for the various veins are listed in Table 3. Forty-five total monazite analyses of the twenty-five grains from the LCV were < 5% discordant, with a U concentration threshold of <1000 ppm, high U analyses, which yielded $^{207}Pb/^{206}Pb$

dates that ranged from 2725-2690 Ma, with the highest U analyses clustering at ~2697 Ma (Fig. 22a). Twenty-two monazite analyses of the eighteen monazite grains from HBV have very low U in comparison to the other veins, with common Pb affecting dates which range from 2.0-3.5 Ga. The thirteen analysis from monazite with a higher U concentration form a spread of dates, largely between 2711-2780 Ma, with a cluster of four analyses from the HBV yielding a weighted mean $^{207}Pb/^{206}Pb$ date of 2723 Ma ± 16 Ma (Fig. 22b). Finally, nineteen monazite analysis of the twelve monazite grains from the SRV had a high U concentration (>500ppm) and a low (< 5%) discordant, which yielded a spread of individual $^{207}Pb/^{206}Pb$ dates that ranged from 2725-2700 Ma, with five monazite analysis with the highest U analyses clustering at ~2701 Ma (Fig. 22c).

**Table 3:** Monazite U-Pb isotopic data from various mineralized veins within the Hammond Reef deposit**.**

| | | | | | | | | | | **Ages** | | | | | | |
|---|---|---|---|---|---|---|---|---|---|---|---|---|---|---|---|---|
| **Fraction** | **Description** | **U (ppm)** | **U/ Th** | **$^{206}$Pb/ $^{238}$U/** | **± 2σ** | **$^{207}$Pb/ $^{235}$U** | **± 2σ** | **$^{207}$Pb/ $^{206}$Pb** | **± 2σ** | **$^{206}$Pb/ $^{238}$U** | **± 2σ** | **$^{207}$Pb/ $^{235}$U** | **± 2σ** | **$^{207}$Pb/ $^{206}$Pb** | **± 2σ** | **Disc. (%)** |
| ***Monazite in LCV*** | | | | | | | | | | | | | | | | |
| M1 | 20 µm, no zoning, loc. Alt halo | 1151.2 | 0.440961271 | 0.506843833 | 0.013168404 | 12.86111838 | 0.411245694 | 0.184296982 | 0.000538339 | **2643.06** | **56.3** | **2669.36** | **30.1** | **2691.08** | **4.8** | 1.8 |
| M2 | 20 µm, no zoning, loc. Alt halo | 1064.8 | 0.256044305 | 0.514235428 | 0.013366891 | 13.11401083 | 0.418672617 | 0.184485833 | 0.00046128 | **2674.54** | **56.9** | **2687.68** | **30.0** | **2692.82** | **4.1** | 0.7 |
| M3 | 20 µm, no zoning, loc. Alt halo | 931.8 | 0.256215134 | 0.505061801 | 0.013149014 | 12.8515311 | 0.412080008 | 0.184533342 | 0.000441008 | **2635.38** | **56.2** | **2668.58** | **30.0** | **2693.26** | **3.9** | 2.1 |
| M4 | 20 µm, no zoning, loc. Alt halo | 1623.0 | 0.417256174 | 0.513500965 | 0.013678589 | 13.08475231 | 0.426457261 | 0.184617 | 0.000543311 | **2671.35** | **58.1** | **2685.47** | **30.6** | **2693.99** | **4.9** | 0.8 |
| M5 | 20 µm, no zoning, loc. Alt halo | 1144.8 | 0.278043571 | 0.518687006 | 0.013453333 | 13.23808217 | 0.422787332 | 0.184812209 | 0.00044667 | **2693.57** | **57.0** | **2696.68** | **30.0** | **2695.75** | **4.0** | 0.1 |
| M6 | 20 µm, no zoning, loc. Alt halo | 458.8 | 0.132059468 | 0.51438504 | 0.015188578 | 13.25800209 | 0.494037463 | 0.184873132 | 0.000674391 | **2674.69** | **64.4** | **2696.85** | **34.3** | **2696.26** | **6.0** | 0.8 |
| M7 | 20 µm, no zoning, loc. Alt halo | 1407.8 | 0.420614964 | 0.527469201 | 0.013657195 | 13.41911183 | 0.42733761 | 0.184914797 | 0.000432146 | **2730.71** | **57.5** | **2709.50** | **29.9** | **2696.68** | **3.9** | -1.3 |
| M8 | 20 µm, no zoning, loc. Alt halo | 1175.0 | 0.298502554 | 0.514054277 | 0.013727321 | 13.15411973 | 0.428700585 | 0.184908351 | 0.000450606 | **2673.46** | **58.2** | **2690.15** | **30.2** | **2696.97** | **3.9** | 0.9 |
| M9 | 20 µm, no zoning, loc. Alt halo | 708.8 | 0.17857513 | 0.521359609 | 0.013591267 | 13.36199526 | 0.427238588 | 0.185143135 | 0.000425153 | **2704.90** | **57.5** | **2705.48** | **30.1** | **2698.72** | **3.8** | -0.2 |
| M10 | 20 µm, no zoning, loc. Alt halo | 1158.1 | 0.397276878 | 0.521296854 | 0.01353861 | 13.30890318 | 0.423567508 | 0.185143332 | 0.000426887 | **2704.66** | **57.4** | **2701.78** | **30.1** | **2698.72** | **3.8** | -0.2 |
| M11 | 20 µm, no zoning, loc. vein | 385.6 | 0.062931786 | 0.53402495 | 0.01429144 | 13.6943082 | 0.464636538 | 0.185225781 | 0.000900131 | **2758.24** | **59.8** | **2728.35** | **31.6** | **2699.35** | **8.0** | -2.2 |
| M12 | 20 µm, no zoning, loc. vein | 673.8 | 0.039750186 | 0.540157794 | 0.014097225 | 13.80406097 | 0.455079168 | 0.185237911 | 0.001120515 | **2784.07** | **58.9** | **2736.13** | **31.1** | **2699.39** | **10.0** | -3.1 |
| M13 | 20 µm, no zoning, loc. Alt halo | 354.5 | 0.154268973 | 0.534659541 | 0.013987874 | 13.71703088 | 0.447563728 | 0.185291944 | 0.001045527 | **2761.01** | **58.8** | **2730.23** | **30.8** | **2699.93** | **9.3** | -2.3 |
| M14 | 20 µm, no zoning, loc. Alt halo | 470.7 | 0.259046268 | 0.510735868 | 0.013269143 | 13.07647513 | 0.422264833 | 0.185413937 | 0.000743684 | **2659.74** | **56.6** | **2685.07** | **30.2** | **2701.08** | **6.6** | 1.5 |
| M15 | 20 µm, no zoning, loc. Alt halo | 588.5 | 0.180538103 | 0.521794452 | 0.013479552 | 13.370937 | 0.425025002 | 0.185435663 | 0.0004525 | **2706.78** | **57.0** | **2706.17** | **30.0** | **2701.31** | **4.0** | -0.2 |
| M16 | 20 µm, no zoning, loc. Alt halo | 791.0 | 0.203187923 | 0.526843019 | 0.013770313 | 13.50076567 | 0.432515472 | 0.185499122 | 0.000439863 | **2727.92** | **58.1** | **2715.86** | **31.6** | **2701.88** | **3.9** | -1.0 |

**Table 3:** Continue

| | | | | | | | | | | **Ages** | | | | | | |
|---|---|---|---|---|---|---|---|---|---|---|---|---|---|---|---|---|
| **Fraction** | **Description** | **U (ppm)** | **U/ Th** | **$^{206}$Pb/ $^{238}$U/** | **± 2σ** | **$^{207}$Pb/ $^{235}$U** | **± 2σ** | **$^{207}$Pb/ $^{206}$Pb** | **± 2σ** | **$^{206}$Pb/ $^{238}$U** | **± 2σ** | **$^{207}$Pb/ $^{235}$U** | **± 2σ** | **$^{207}$Pb/ $^{206}$Pb** | **± 2σ** | **Disc. (%)** |
| M17 | 20 µm, no zoning, loc. Alt halo | 231.3 | 0.029002457 | 0.490651129 | 0.050668675 | 12.56787322 | 1.310250581 | 0.185419953 | 0.001073232 | **2573.43** | **218.8** | **2647.63** | **98.7** | **2702.70** | **8.9** | 4.8 |
| M18 | 20 µm, no zoning, loc. Alt halo | 805.6 | 0.04467871 | 0.516480057 | 0.01336048 | 13.15898678 | 0.41908696 | 0.18559873 | 0.000511296 | **2684.20** | **56.7** | **2691.04** | **30.0** | **2702.73** | **4.6** | 0.7 |
| M19 | 20 µm, no zoning, loc. Alt halo | 583.5 | 0.20331609 | 0.51326178 | 0.013347712 | 13.19061789 | 0.421014904 | 0.185680882 | 0.000466991 | **2670.51** | **56.8** | **2693.31** | **30.0** | **2703.48** | **4.2** | 1.2 |
| M20 | 20 µm, no zoning, loc. vein | 766.1 | 0.042891388 | 0.532826854 | 0.013975614 | 13.6623964 | 0.452018587 | 0.18579844 | 0.000735899 | **2753.28** | **58.6** | **2726.29** | **30.9** | **2704.49** | **6.5** | -1.8 |
| M21 | 20 µm, no zoning, loc. Alt halo | 2063.2 | 0.770905608 | 0.512669226 | 0.013285554 | 13.13669488 | 0.419064763 | 0.185833931 | 0.00047125 | **2667.98** | **56.5** | **2689.42** | **29.9** | **2704.84** | **4.2** | 1.4 |
| M22 | 20 µm, no zoning, loc. Alt halo | 748.7 | 0.224339673 | 0.519658179 | 0.013428941 | 13.37183163 | 0.425636172 | 0.186105216 | 0.000516936 | **2697.70** | **56.8** | **2706.21** | **29.8** | **2707.26** | **4.6** | 0.4 |
| M23 | 20 µm, no zoning, loc. vein | 263.7 | 0.07628995 | 0.537534296 | 0.014708654 | 13.86873913 | 0.474996836 | 0.186167478 | 0.001086287 | **2772.90** | **61.5** | **2740.29** | **32.2** | **2707.66** | **9.6** | -2.4 |
| M24 | 20 µm, no zoning, loc. Alt halo | 730.9 | 0.116485394 | 0.515654041 | 0.013466828 | 13.32637647 | 0.441092432 | 0.18616984 | 0.000760866 | **2680.67** | **57.1** | **2702.80** | **30.8** | **2707.80** | **6.7** | 1.0 |
| M25 | 20 µm, no zoning, loc. Alt halo | 462.7 | 0.161659402 | 0.523529138 | 0.013672863 | 13.47420358 | 0.433455542 | 0.186196587 | 0.00073114 | **2714.04** | **57.9** | **2713.25** | **30.5** | **2707.91** | **6.5** | -0.2 |
| M26 | 20 µm, no zoning, loc. vein | 270.4 | 0.04279236 | 0.53126143 | 0.01391577 | 13.68374357 | 0.449234787 | 0.186476327 | 0.000821583 | **2746.70** | **58.5** | **2727.84** | **30.8** | **2710.48** | **7.3** | -1.3 |
| M27 | 20 µm, no zoning, loc. Alt halo | 166.8 | 0.052393279 | 0.512660327 | 0.013786392 | 13.21062483 | 0.434939904 | 0.186778536 | 0.000662802 | **2667.53** | **58.7** | **2694.11** | **30.9** | **2713.09** | **5.8** | 1.7 |
| M28 | 20 µm, no zoning, loc. Alt halo | 669.0 | 0.041009399 | 0.516976665 | 0.01352214 | 13.34954759 | 0.430903957 | 0.186878862 | 0.000515768 | **2686.24** | **57.2** | **2704.48** | **30.0** | **2714.10** | **4.5** | 1.0 |
| M29 | 20 µm, no zoning, loc. Alt halo | 1301.2 | 0.279479085 | 0.523855694 | 0.013658557 | 13.50478422 | 0.434053786 | 0.18699156 | 0.000639407 | **2715.38** | **57.8** | **2715.35** | **30.3** | **2714.98** | **5.6** | 0.0 |
| M30 | 20 µm, no zoning, loc. Alt halo | 506.9 | 0.152183371 | 0.513190149 | 0.01361161 | 13.26300092 | 0.438401829 | 0.187007954 | 0.000728627 | **2669.93** | **57.8** | **2697.78** | **30.9** | **2715.07** | **6.4** | 1.7 |
| M31 | 20 µm, no zoning, loc. vein | 141.3 | 0.041433973 | 0.526431531 | 0.013930558 | 13.54514102 | 0.438564159 | 0.1871118 | 0.000701232 | **2726.13** | **58.6** | **2718.06** | **30.2** | **2716.91** | **6.5** | -0.3 |
| M32 | 20 µm, no zoning, loc. Alt halo | 603.6 | 0.151097372 | 0.51771029 | 0.013986363 | 13.59240352 | 0.469300707 | 0.187554751 | 0.000729849 | **2689.36** | **59.2** | **2721.41** | **32.3** | **2720.05** | **6.4** | 1.1 |
| M33 | 20 µm, no zoning, loc. Alt halo | 448.1 | 0.084732652 | 0.535390653 | 0.014103628 | 13.97336527 | 0.464123813 | 0.187561834 | 0.000717341 | **2764.07** | **59.1** | **2747.70** | **31.2** | **2720.11** | **6.3** | -1.6 |
| M34 | 20 µm, no zoning, loc. Alt halo | 233.6 | 0.103112748 | 0.509107275 | 0.013568015 | 13.20955293 | 0.432559762 | 0.187619553 | 0.000662914 | **2652.60** | **57.9** | **2694.37** | **30.9** | **2720.56** | **5.8** | 2.5 |

**Table 3**: Continue

| | | | | | | | | | | Ages | | | | | | |
|---|---|---|---|---|---|---|---|---|---|---|---|---|---|---|---|---|
| **Fraction** | **Description** | **U** | **U/** | **$^{206}$Pb/** | **± 2σ** | **$^{207}$Pb/** | **± 2σ** | **$^{207}$Pb/** | **± 2σ** | **$^{206}$Pb/** | **± 2σ** | **$^{207}$Pb/** | **± 2σ** | **$^{207}$Pb/** | **± 2σ** | **Disc.** |
| | | **(ppm)** | **Th** | **$^{238}$U/** | | **$^{235}$U** | | **$^{206}$Pb** | | **$^{238}$U** | | **$^{235}$U** | | **$^{206}$Pb** | | **(%)** |
| M35 | 20 µm, no zoning, loc. Alt halo | 38.7 | 0.003945322 | 0.497228222 | 0.052465724 | 12.91827511 | 1.470518017 | 0.18753094 | 0.007728031 | **2600.37** | **225.9** | **2665.32** | **110.3** | **2724.79** | **61.1** | 4.6 |
| M36 | 20 µm, no zoning, loc. Alt halo | 295.6 | 0.125780116 | 0.513045034 | 0.013666261 | 13.41411987 | 0.445636537 | 0.188345135 | 0.000890068 | **2669.50** | **58.1** | **2708.95** | **31.1** | **2726.90** | **7.8** | 2.1 |
| M37 | 20 µm, no zoning, loc. Alt halo | 221.4 | 0.031596019 | 0.529975174 | 0.055394188 | 13.77093332 | 1.459176691 | 0.188399521 | 0.001284696 | **2739.99** | **230.8** | **2731.95** | **97.0** | **2726.93** | **11.2** | -0.5 |
| M38 | 20 µm, no zoning, loc. Alt halo | 230.6 | 0.031432031 | 0.508668367 | 0.052542462 | 13.28940082 | 1.388585566 | 0.188392749 | 0.001876578 | **2650.91** | **224.8** | **2700.27** | **98.4** | **2727.00** | **16.3** | 2.8 |
| M39 | 20 µm, no zoning, loc. Alt halo | 286.7 | 0.183553804 | 0.507875452 | 0.013209897 | 13.19199283 | 0.421543235 | 0.18848603 | 0.000542029 | **2647.43** | **56.5** | **2693.30** | **30.1** | **2728.16** | **4.7** | 3.0 |
| M40 | 20 µm, no zoning, loc. Alt halo | 304.0 | 0.085238285 | 0.516352607 | 0.013377644 | 13.49517315 | 0.434624797 | 0.189361794 | 0.000878604 | **2683.67** | **56.8** | **2714.83** | **30.4** | **2735.74** | **7.6** | 1.9 |
| M41 | 20 µm, no zoning, loc. Alt halo | 399.2 | 0.014523163 | 0.533660348 | 0.013746617 | 13.95585972 | 0.444611268 | 0.189619314 | 0.00058412 | **2756.84** | **57.7** | **2746.64** | **30.1** | **2738.05** | **5.1** | -0.7 |
| M42 | 20 µm, no zoning, loc. vein | 247.8 | 0.009666308 | 0.543065219 | 0.014116461 | 14.34823282 | 0.46547399 | 0.191503215 | 0.001051356 | **2796.23** | **58.9** | **2772.85** | **30.7** | **2754.18** | **9.0** | -1.5 |
| M43 | 20 µm, no zoning, loc. Alt halo | 214.1 | 0.068626878 | 0.503287141 | 0.014209073 | 13.57228648 | 0.524709637 | 0.193026085 | 0.001975081 | **2627.50** | **60.8** | **2718.53** | **36.2** | **2766.59** | **16.5** | 5.0 |
| M44 | 20 µm, no zoning, loc. Alt halo | 234.4 | 0.015707611 | 0.53082515 | 0.054853531 | 14.37036774 | 1.506462918 | 0.194834387 | 0.002345867 | **2744.89** | **231.0** | **2774.21** | **99.9** | **2782.12** | **19.8** | 1.3 |
| M45 | 20 µm, no zoning, loc. Alt halo | 139.8 | 0.016138732 | 0.510316311 | 0.052826626 | 13.90554107 | 1.470249224 | 0.196094133 | 0.002983147 | **2657.79** | **225.2** | **2742.09** | **98.4** | **2791.45** | **24.7** | 4.8 |
| ***Monazite in HBV*** | | | | | | | | | | | | | | | | |
| M1 | 10 µm, zoning, loc. Alt halo | 1276.7 | 0.016125006 | 0.50561323 | 0.052218597 | 13.10219542 | 1.368811209 | 0.186547248 | 0.001209064 | **2637.85** | **223.3** | **2686.88** | **98.1** | **2711.02** | **10.7** | 2.7 |
| M2 | 10 µm, zoned, loc. Alt halo | 230.1 | 0.00309638 | 0.553956909 | 0.05733894 | 14.41906955 | 1.505303604 | 0.188287553 | 0.001035104 | **2841.30** | **238.4** | **2777.37** | **99.8** | **2726.18** | **9.0** | -4.2 |
| M3 | 10 µm, zoned, loc. Alt halo | 291.1 | 0.002120697 | 0.533125512 | 0.101465044 | 13.88880139 | 2.651112877 | 0.188488081 | 0.001862457 | **2669.41** | **394.0** | **2653.58** | **156.2** | **2727.39** | **16.3** | 2.1 |
| M4 | 10 µm, zoned, loc. Alt halo | 161.0 | 0.003152104 | 0.497154075 | 0.051589351 | 13.01540292 | 1.366561913 | 0.189175304 | 0.001628462 | **2600.94** | **221.2** | **2679.57** | **98.5** | **2736.10** | **15.3** | 4.9 |

**Table 3**: Continue

| | | | | | | | | | | Ages | | | | | | |
|---|---|---|---|---|---|---|---|---|---|---|---|---|---|---|---|---|
| **Fraction** | **Description** | **U (ppm)** | **U/ Th** | **$^{206}$Pb/ $^{238}$U/** | **± 2σ** | **$^{207}$Pb/ $^{235}$U** | **± 2σ** | **$^{207}$Pb/ $^{206}$Pb** | **± 2σ** | **$^{206}$Pb/ $^{238}$U** | **± 2σ** | **$^{207}$Pb/ $^{235}$U** | **± 2σ** | **$^{207}$Pb/ $^{206}$Pb** | **± 2σ** | **Disc. (%)** |
| ***Monazite in SRV*** | | | | | | | | | | | | | | | | |
| M1 | 20 µm, no zoning, loc. Alt halo | 217.6 | 0.010944553 | 0.507054101 | 0.013159162 | 13.52324269 | 0.434328811 | 0.192702758 | 0.000832781 | **2643.96** | **56.2** | **2716.64** | **30.3** | **2764.32** | **7.1** | 4.4 |
| M2 | 20 µm, no zoning, loc. vein | 294.8 | 0.025284907 | 0.516283234 | 0.013847872 | 14.21773118 | 0.468401702 | 0.199244082 | 0.001153159 | **2682.90** | **58.9** | **2764.89** | **32.4** | **2820.05** | **9.8** | 4.9 |
| M3 | 20 µm, no zoning, loc. vein | 305.7 | 0.01603761 | 0.516774012 | 0.013365157 | 14.02470246 | 0.448921673 | 0.196616642 | 0.000758276 | **2685.48** | **56.8** | **2751.35** | **30.2** | **2797.54** | **6.3** | 4.0 |
| M4 | 20 µm, no zoning, loc. vein | 315.8 | 0.015814695 | 0.505538186 | 0.013079667 | 13.29321439 | 0.424490397 | 0.190062016 | 0.000716507 | **2637.52** | **56.0** | **2700.58** | **30.0** | **2741.81** | **6.2** | 3.8 |
| M5 | 20 µm, zoned, loc. Alt halo | 1626.1 | 0.055811913 | 0.51695714 | 0.013442114 | 13.23688907 | 0.422047221 | 0.185307542 | 0.00040982 | **2686.24** | **57.1** | **2696.66** | **30.1** | **2700.19** | **3.7** | 0.5 |
| M6 | 20 µm, zoned, loc. Alt halo | 2107.8 | 0.090605727 | 0.507394653 | 0.01311893 | 12.99095723 | 0.412224684 | 0.185317702 | 0.000418659 | **2645.49** | **56.1** | **2678.98** | **29.8** | **2700.29** | **3.7** | 2.0 |
| M7 | 20 µm, zoned, loc. Alt halo | 1493.5 | 0.042251684 | 0.516427129 | 0.013369376 | 13.23543137 | 0.420753553 | 0.185522725 | 0.000404486 | **2684.00** | **56.9** | **2696.57** | **30.0** | **2702.11** | **3.6** | 0.7 |
| M8 | 20 µm, zoned, loc. Alt halo | 1734.2 | 0.084310199 | 0.491827224 | 0.012724472 | 12.60922816 | 0.400016949 | 0.185530132 | 0.000422161 | **2578.50** | **55.0** | **2650.81** | **29.9** | **2702.17** | **3.8** | 4.6 |
| M9 | 20 µm, zoned, loc. Alt halo | 526.0 | 0.028600315 | 0.509601954 | 0.013215793 | 13.08921469 | 0.417035355 | 0.185896579 | 0.000462467 | **2654.84** | **56.5** | **2686.58** | **31.7** | **2705.40** | **4.1** | 1.9 |
| M10 | 20 µm, zoned, loc. Alt halo | 680.6 | 0.026185301 | 0.496821198 | 0.012916721 | 12.77570009 | 0.407462451 | 0.186104003 | 0.000404603 | **2599.99** | **55.5** | **2663.07** | **29.8** | **2707.27** | **3.6** | 4.0 |
| M11 | 20 µm, zoned, loc. Alt halo | 1070.1 | 0.035889003 | 0.491937889 | 0.012869144 | 12.6636157 | 0.406755318 | 0.186148256 | 0.000407937 | **2578.87** | **55.6** | **2654.65** | **30.1** | **2707.66** | **3.6** | 4.8 |
| M12 | 20 µm, no zoning, loc. Alt halo | 537.8 | 0.022018479 | 0.504418694 | 0.013274713 | 13.00700845 | 0.422412858 | 0.186319774 | 0.000818182 | **2632.65** | **56.6** | **2679.94** | **30.3** | **2709.05** | **7.2** | 2.8 |
| M13 | 20 µm, zoned, loc. Alt halo | 810.0 | 0.034580114 | 0.50649402 | 0.013816588 | 13.11530617 | 0.428181577 | 0.186476865 | 0.000641136 | **2641.52** | **59.1** | **2687.87** | **30.8** | **2710.56** | **5.7** | 2.5 |
| M14 | 20 µm, zoned, loc. Alt halo | 497.8 | 0.019998295 | 0.528241163 | 0.014364311 | 13.61703195 | 0.446116254 | 0.186479986 | 0.000437802 | **2733.39** | **60.2** | **2722.79** | **30.5** | **2710.59** | **3.9** | -0.8 |
| M15 | 20 µm, zoned, loc. Alt halo | 1521.7 | 0.039093648 | 0.505593344 | 0.013131939 | 13.03699321 | 0.414661568 | 0.186687826 | 0.00042487 | **2637.78** | **56.2** | **2682.31** | **30.0** | **2712.43** | **3.8** | 2.8 |
| M16 | 20 µm, no zoning, loc. Alt halo | 504.7 | 0.020606641 | 0.506937573 | 0.013147393 | 13.18384373 | 0.427249235 | 0.187219634 | 0.001239666 | **2643.53** | **56.2** | **2692.77** | **30.5** | **2716.89** | **10.9** | 2.7 |
| M17 | 20 µm, zoned, loc. Alt halo | 1142.6 | 0.037137121 | 0.494695281 | 0.013089738 | 12.82643301 | 0.419552193 | 0.187193925 | 0.000431794 | **2590.77** | **56.3** | **2666.57** | **30.3** | **2716.90** | **3.8** | 4.6 |

**Table 3**: Continue

| Fraction | Description | U (ppm) | U/ Th | $^{206}$Pb/ $^{238}$U/ | ± 2σ | $^{207}$Pb/ $^{235}$U | ± 2σ | $^{207}$Pb/ $^{206}$Pb | ± 2σ | Ages | | | | | | Disc. (%) |
|---|---|---|---|---|---|---|---|---|---|---|---|---|---|---|---|---|
| | | | | | | | | | | **$^{206}$Pb/ $^{238}$U** | **± 2σ** | **$^{207}$Pb/ $^{235}$U** | **± 2σ** | **$^{207}$Pb/ $^{206}$Pb** | **± 2σ** | |
| M18 | 20 µm, zoned, loc. Alt halo | 698.9 | 0.025646241 | 0.505944941 | 0.013093792 | 13.11186687 | 0.417060481 | 0.187525711 | 0.000443919 | **2639.29** | **56.0** | **2687.72** | **30.0** | **2719.81** | **3.9** | 3.0 |
| M19 | 20 µm, zoned, loc. Alt halo | 848.5 | 0.028204869 | 0.505439461 | 0.013110134 | 13.40071981 | 0.436161062 | 0.188196576 | 0.000628142 | **2637.12** | **56.1** | **2708.26** | **30.7** | **2725.71** | **5.5** | 3.3 |

Notes: LCV, Laminated crustiform vein; HBV, Hydrothermal breccia vein; SRV, Sulfide rich vein
Loc., Location; Alt., Alteration; Disc., Discordance

### *TIMS U/Pb age of Diversion stock*

Sample 21GJF-0027A of the Diversion stock tonalite was collected along the western margin of the Marmion Batholith beyond the alteration envelope of the Hammond Reef deposit. The sample is a coarse grained porphyritic tonalite with weak sericite and chlorite alteration. A heavy mineral concentrate from this sample yielded mostly pyrite with 180 tiny, colourless to medium brown, altered zircons. The zircons are cloudy and locally stained; 3 of the higher quality grains have straight crystal faces with square cross-sections and short (~2:1) clear prisms (Fig 23).

Results for three chemically abraded, single grain fractions returned uniform results; two of the three fractions are perfectly concordant (Z1, Z3) and yielded a weighted average $^{207}$Pb/$^{206}$Pb age of 2890.2 ± 1.0 Ma (Table 4). A third fraction (Z2) is slightly discordant and lies on a poorly-defined secondary Pb-loss trajectory with an upper intercept age of 2889.0 ± 2.2 Ma, which is consider less reliable than the age for the two concordant points alone. It has an imprecise lower intercept age of 1662 ± 390 Ma without geological significance.

**Table 4:** Zircon U-Pb isotopic data for Diverson stock tonalitic intrusion, Hammond Reef area.

| | | | | | | | | | | | | | **Ages (Ma)** | | | | | | |
|---|---|---|---|---|---|---|---|---|---|---|---|---|---|---|---|---|---|---|---|
| **Fraction** | **Description** | **U (ppm)** | **Pb$^T$ (pg)** | **Pb$_C$ (pg)** | **Th/U** | **$^{206}$Pb/ $^{204}$Pb** | **$^{206}$Pb/ $^{238}$U** | **± 2σ** | **$^{207}$Pb/ $^{235}$U** | **± 2σ** | **$^{207}$Pb/ $^{206}$Pb** | **± 2σ** | **$^{206}$Pb/ $^{238}$U** | **± 2σ** | **$^{207}$Pb/ $^{235}$U** | **± 2σ** | **$^{207}$Pb/ $^{206}$Pb** | **± 2σ** | **Disc. (%)** |
| ***21GJF-0027A; Diversion stock, coarse-grained tonalite (607308E, 5419217N, Zone 15U).*** | | | | | | | | | | | | | | | | | | | |
| Z1 | 1 clr, cls, dbly-term pr | 229 | 155.71 | 0.30 | 0.687 | 27751 | 0.566095 | 0.001318 | 16.23705 | 0.04315 | 0.208026 | 0.000175 | **2891.8** | **5.4** | **2890.9** | **2.5** | **2890.2** | **1.4** | -0.1 |
| Z2 | 1 clr, cls, sm shard | 176 | 50.72 | 0.22 | 0.629 | 12468 | 0.561396 | 0.001318 | 16.02649 | 0.04298 | 0.207046 | 0.000179 | **2872.4** | **5.4** | **2878.4** | **2.6** | **2882.6** | **1.4** | 0.4 |
| Z3 | 1 clr, 3:1 dbly-term pr, cldy tips | 160 | 110.68 | 0.41 | 0.771 | 14275 | 0.566315 | 0.001402 | 16.24338 | 0.04532 | 0.208026 | 0.000184 | **2892.7** | **5.8** | **2891.2** | **2.7** | **2890.2** | **1.4** | -0.1 |

*Notes:*

All analyzed fractions represent best optical quality (crack-, inclusion-, core-free), fresh (least altered) grains of zircon. Zircons were chemically abraded (modified after Mattinson, 2005).

Abbreviations: Z - zircon; clr - clear; cldy - cloudy; cls - colourless; dbly-term - doubly-terminated; pr - prism/prismatic; sm - small; X:Y - length:breadth ratio.

Pb$^T$ is total amount (in picograms) of Pb.

Pb$_C$ is total measured common Pb (in picograms) assuming the isotopic composition of laboratory blank: 206/204 - 18.49 ± 0.4%; 207/204 - 15.59 ± 0.4%; 208/204 - 39.36 ± 0.4%

Pb/U atomic ratios are corrected for spike, fractionation, blank, and, where necessary, initial common Pb; 206Pb/204Pb is corrected for spike and fractionation.

Th/U is model value calculated from radiogenic 208Pb/206Pb ratio and 207Pb/206Pb age, assuming concordance.

Disc. (%) - per cent discordance for the given 207Pb/206Pb age.

Uranium decay constants are from Jaffey et al. (1971).

## 2.5 Discussion

### 2.5.1 Structural Interpretation

Shear zones and faults in the northern and southern domains have similar NNE trends and kinematic deformation history. In the northern domain, the Sawbill vein fills and is parallel to a NNE-striking shear zone. The anticlockwise rotation of the foliation and veins within the shear zone and the presence of dilatational left-stepping jogs suggest sinistral transcurrent movement along the shear zone. The foliation is only present within the shear zone, where it is oriented oblique and clockwise to the walls of the shear zone, suggesting that it formed as a mylonitic S-fabric during shearing. The striations along the laminated Sawbill vein are subhorizontal and perpendicular to the common intersection line between the foliation and the vein, further suggesting that the laminated vein formed as a shear vein during transcurrent movement along the shear zone (Fig. 12). Other narrow quartz veins are oblique to both foliation and laminated vein but share the same common intersection line. Their orientation (i.e. 70° anticlockwise of the laminated vein), open-space filling vuggy textures, and wedge-like tapering, are consistent with their formation as extensional veins during sinistral transcurrent movement along the shear zone. Sinistral transcurrent shear indicators are further observed along NNE-trending faults and shear zones in the southern domain, as exemplified on Outcrop #5 by S-shaped drag folds, sinistral shear bands, and the rotation of the foliation along the margin of the quartz vein filling the shear zone. As the vein contains foliated fragments of the host rock but predates the dragging of the foliation along its margin, this suggests that it was emplaced during slip and the formation of the foliation along the shear zone, similar to the Sawbill vein.

Sericitization along shear zones began during early brittle faulting prior to ductile shearing. Faults and fractures localized the flow of hydrothermal fluids, which reacted with the host tonalite to produce sericite sealing the faults. Because sericite is a weak mineral, further slip along the faults was accommodated by ductile shearing instead of brittle faulting. This process, which is called fluid-rock reaction weakening, was responsible for the evolution of early brittle faults into the ductile Marmion shear system (Backeberg et al., 2016). Ductile shearing resulted in the formation of an internal shear zone foliation (S-fabric) and reduced the permeability of the shear zones. Reductions in permeability caused increases in fluid pressures, which can be enhanced by the influx of fluids at depth and their upward migration along the shear zones (Gratier and Gueydan, 2007; Wintsch et al., 1995). The increases in fluid pressures and stresses across the shear zones caused brittle failure and the formation of through-going faults, which were sealed again by the formation of more alteration minerals, compaction, and the deposition of hydrothermal minerals. Cyclic changes in fluid pressures, permeability, and stresses across faults and shear zones explain the formation of orogenic gold deposits along major faults and shear zones, as conceptualized in the fault valve model of Sibson et al. (1988) (see also Robert et al., 1995 and Cox, 1999, 2010, 2020).

Shear zones and faults in the central domain differ in orientation from those in the southern and northern domains. They trend ENE; thus, the central domain represents a contractional bend or jog between the NNE trending southern and northern domains. The central domain likely originated as a soft-linked step-over zone between the underlapping transcurrent shear zones and faults of the southern and northern domains. Step-over zones are areas of more evenly distributed strain and are characterized by the formation of fracture networks, folds and second-order faults (Parchell and Evans, 2002; Micklethwaite, 2010). The central domain evolved into a hard-linked step-over zone by the formation of through-going faults that linked the southern domain with the northern domain. Thus, the central domain represents a hard-linked, right-stepping, contractional step-over zone between the sinistral transcurrent faults of the northern and southern domain.

Although gold-bearing veins formed during shearing along NNE-trending faults and shear zones in the southern domain (Gold Mine Island) and northern domain (Sawbill prospect), the bulk of the mineralization (Hammond Reef deposit) occurs in the central domain. Fault and shear zone linkage across step-over zones can be significant in localizing permeability and enhancing fluid flow and mineralization in fault-related hydrothermal systems (Cox, 2020). Along the MSS, the cleavage is ENE-striking across the three structural domain, which is consistent with sinistral shearing along the NNE-trending shear zones and faults of the southern and northern domains and with compression and increased contraction across the central domain. Increased compression and normal stress across the central domain during bulk NNW shortening increased compaction and permeability reduction in the host rocks. Conversely, it increased fracture-controlled permeability through the formation of fracture networks, represented by the syn-deformation hydrothermal breccias, and the formation of linking second-order sinistral faults and reverse faults in which the shallowly-dipping thick quartz veins with dip-parallel striations were emplaced. Dilation and increased permeability in a contractional jog, such as the central domain, may occur through in-fault dilation associated with slip on irregular fault surfaces and dilational fracture growth driven by increased fluid pressure, resulting in the formation of extensional veins and dilational breccias (Cox, 2020).

During major earthquakes, contractional jogs or step-over zones may impede the propagation of faults. The stress is then transferred from the main faults to the step-over zones, resulting in the localization of minor ruptures and aftershocks in those zones (King et al., 1994; Cox et al., 2004; Micklethwaite and Cox, 2006; Micklethwaite, 2010). In addition, fluid reservoirs may be breached during seismic ruptures along the main faults resulting in the injection of high-pressure fluid pulses and further rupture of stress-loaded second-order faults in the step-over zones (Cox, 2010, 2016, 2020). Repeated shear failure and ruptures along the main faults may have resulted in the cyclical formation of the gold-bearing extensional veins, hydrothermal breccias, and fracture arrays in the step-over zone hosting the Hammond Reef deposit.

A similar structural setting is reported for the St. Ives deposit in the Yilgarn craton, Western Australia. This world renown deposit has a measured and indicated resource estimate of 5.17 Moz of gold (Gold Fields Updated Mineral Resource, 2018). The bulk of the mineralization is hosted by low displacement faults and shear zones within a 20 $km^2$ contractional jog, called the Victory jog, located between two major sinistral transcurrent faults: the Boulder-Lefroy and Playa faults (Nguyen, 1997; Cox and Ruming, 2004). Gold deposition and fluid flow occurred along the low displacement structures during aftershocks driven by major slip events along the Boulder-Lefroy and Playa faults (Cox et al., 2001; Cox and Ruming, 2004). The Hammond Reef deposit occupies a similar structural setting and thus may have formed by similar processes.

### 2.5.2 Alteration and Mineralization Interpretation

Orogenic gold systems form during the main orogenic event in a deformed terrane. They have the following general characteristics: a spatial association with major faults/shear zones, intense carbonate and sericite alteration, high Au/Ag ratios and Ag, W, B, As, Mo metal concentrations (Phillips, 1986; Robert and Brown, 1986; Workman, 1986; Proudlove et al., 1989; Groves and Goldfarb, 1998; Poulsen et al., 2000; Legault et al., 2006). Because major faults/shear zones act as conduits for the upward migration of both hydrothermal fluids and melts, intrusion-related gold deposits may be spatially associated with orogenic gold deposits (Hattori, 1987; Roberts and Poulsen, 2001; Duuring et al., 2007; De Souza et al., 2015). Some may even be hybrid deposits with both orogenic and intrusion-related origins (Bigot et al., 2015; Mériaud et al., 2017; Mathieu, 2021; McDivitt et al., 2021); others are solely intrusion-related or orogenic gold deposits but may have experienced more than one mineralization/remobilization events (Martin, 2012; Zhang et al., 2014). Interpreting the origin of gold deposits along major faults and shear zones can therefore be challenging because intrusion-related and orogenic gold deposits may occupy the same space and multiple mineralization events and overprinting deformation and remobilization events may obscure how the deposits formed.

Two mineralization events with distinct alteration envelopes, metal association and alteration mineral chemistry, coexist within the Hammond Reef deposit. The first mineralization event is represented by the LCVs. The LCVs have an alteration halo of Mg-rich chlorite and fine-grained sericite, which is also characteristic of the wider chlorite-carbonate (±sericite) alteration present across the Hammond Reef deposit. The latter has been described on outcrops #3 where it is overprinted by the second mineralization and alteration event. The alteration halo of the LCVs shows a mass gain in Ni and a mass loss in As; however, both Ni and As define the primary growth bands in pyrite. Au, Ag, Te, Pb, Sn, Bi, Co, W are enriched along fractures and are associated with a second generation of inclusion-rich pyrite where they likely precipitated in pores created during dissolution of the zoned pyrite. The metals were either liberated during coupled dissolution of the zoned pyrite and precipitation of the metals in the newly created pores and fractures (Larocque et al., 1995; Fougerouse et al., 2016; Wagner at al., 2016; Hastie et al., 2020), or were precipitated from an external metal-rich fluid. The LCV are folded and overprinted by the regional cleavage and thus represent either a pre-tectonic, possibly intrusion-related, mineralization event, or an early, syn-tectonic, possibly MSS-related, mineralization event.

The second and main mineralization event is represented by the syn-MSS hydrothermal breccias, the quartz-carbonate-chlorite veins, and localized sericite (±carbonate) alteration associated with the veins, faults and shear zones. The altered host tonalite incurred mass gains in K, Ba, S during their sericitization and sulfidation, which are common alteration processes associated with orogenic gold deposits (Phillips, 1986; Robert and Brown, 1986; Workman, 1986; Proudlove et al., 1989; Groves and Goldfarb, 1998; Poulsen et al., 2000; Legault et al., 2006). Early Ni-As-Co-zoned pyrite is replaced by inclusion-rich pyrite and fractures enriched in Au, Ag, As, Te, Bi, Pb, as observed for pyrite in the alteration halo of the LCV, but lack the enrichment in magmatophile W, Sn associated with the latter. Gold is present as micro inclusions in pyrite and as disseminations along pyrite and silicate grain boundaries, fractures, and cleavage (Kolb, 2010; Backeberg, 2015; this study). Thus, gold was either emplaced late during this event from gold-rich fluid pulses or was deposited early and later remobilized during the same event.

The age of mineralization at the Hammond Reef deposit is constrained by the emplacement of the Diversion stock at 2890.2 ± 1 Ma, which is similar to SHRIMP U-Pb zircon ages of 2893 ± 4 Ma for tonalitic intrusions along the northern margin of the Marmion Batholith (Bjorkman, 2017), and the emplacement of ca. 2735 Ma gabbroic intrusions (Stone, 2010), which cut across the 2730-2930 Ma Steep Rock Group (Stone, 2010). These intrusions are offset and overprinted by the MSS and thus provide a maximum age for mineralization. Its minimum age is constrained by the analyzed monazite grains within mineralized veins and their alteration haloes. Monazite is particularly useful in dating hydrothermal systems due to a high thermal resistance of 500-800ºC and successive growth generations capturing variations in fluid composition and age (Smith and Giletti, 1997; Crowley et al., 1999; Williams et al., 2002). Monazite grains range in age from 2690 – 2720 Ma with the highest U analyses clustering at ~2700 Ma, which represent the best estimate on the age of gold mineralization at Hammond Reef. This age corresponds with the main deformation event in the Wabigoon subprovince, which occurred at ca. 2690-2700 Ma during accretion of the Wabigoon and Wawa terranes (or subprovinces) with the Winnipeg River-North Caribou terranes (Corfu et al., 1992; Percival et al., 2006; Sanborn-Barrie and Skulski, 2006; Ma et al., 2022).

The only detailed study conducted on the Hammond Reef deposit is by Backeberg (2015) as part of his PhD thesis. Backeberg (2015) suggested that the NE-trending MSS, which hosts the Hammond Reef deposit, formed along the contact between the Marmion Batholith and the Finlayson greenstone belt before the emplacement of the Diversion stock along this contact. It lay dormant for 100-200 Ma prior to its reactivation as a pure shear high strain zone during boundary-normal NW-SE shortening and coeval dextral slip along the E-trending Quetico fault. However, the MSS is dragged into the Quetico fault which indicates that coeval deformation is not likely. Furthermore, apart from the important observation that the MSS initially formed as brittle faults that overprint the Diversion stock, the interpretation by Backeberg (2015) clashes with current understanding of orogenic gold systems, which invokes the migration of large volumes of hydrothermal fluids with low gold concentrations (Tilling et al., 1973; Kwong and Crokcket, 1978; Kerrich, 1991; Goldfarb and Groves, 2015) along major structures such as faults and shear zones that remain permeable through repeated reactivation and seismic slip along those structures (Sibson et al., 1988; Roberts et al., 1995; Cox, 1999, 2010, 2020; Sibson, 2020).

### 2.5.3 Comparison to other gold deposits in the Wabigoon subprovince

Hammond Reef is one of five significant gold deposits in the Wabigoon Subprovince. Of the four other significant gold deposits, two of them, that is, the Goliath and Rainy River deposits, are syn-volcanic, and the other two, the Goldlund deposit and Hard Rock Mine, are orogenic gold deposits.

The syn-volcanic Goliath gold deposit is located in the Western Wabigoon terrane and has a measured and indicated resource estimate of 1.23 Moz of Au and 3.8 Moz of Ag (Treasury Metals Inc. press release, 2022). Mineralization is associated with a felsic volcanic sill or flow dated at 2703 Ma within a turbiditic sandstone and mudstone sequence of similar age (McRae, 2022). It predates regional deformation and is interpreted as part of a syn-volcanic system (McRae, 2022). The Rainy River deposit in the western Wabigoon has a measured and indicated resource estimate of 6.7 Moz of gold (New Gold Inc. website, December 2015). Mineralization is hosted in a calc-alkaline dacite to rhyodacite complex surrounded by tholeiitic basalts. Mineralized zones are oriented parallel to the main tectonic foliation in the area and high grade zones plunge parallel to a strong stretching lineation along this foliation. Monzonitic dikes, which cut across mineralization, and a weakly mineralized coherent dacite flow or sill, are dated at ca. 2693 Ma and ca. 2717 Ma, respectively (U-Pb zircon; Pelletier et al., 2016). These ages, structural overprinting relationships, and the style and spatial zonation of alteration and mineralization, suggest that Rainy River deposit is a gold-rich volcanogenic massive sulfide (VMS) deposit (Pelletier et al., 2016).

The Hard Rock mine in the eastern Wabigoon subprovince has a resource estimate of 6.4 Moz gold (G Mining Services, 2016). Mineralization is hosted within a panel of < ca. 2700 Ma turbiditic sandstone, polymictic conglomerate, banded iron formation, and younger ca. 2694 Ma feldspar-quartz porphyry intrusions. Gold was emplaced during two separate events. The first mineralization event, which is expressed by quartz-carbonate veins and their alteration halo, occurred during an early $D_1$ thrusting event, which postdates the emplacement of the feldspar-quartz porphyry and predate the emplacement of the 2690 ± 1 Ma Croll Lake Stock (Tóth, 2019; Tóth et al., 2022). Thus, it is similar in age (ca. 2694 Ma – ca. 2690 Ma) to that of gold mineralization at the Hammond Reef deposit. The second mineralization event is associated with tourmaline and quartz-carbonate veins that were emplaced during a later regional folding and shearing event (Tóth, 2019; Tóth et al., 2022).

The Goldlund deposit in the western Wabigoon subprovince occupies a wide shear zone similar in orientation and shear sense to the MSS. It has a measured and indicated resource estimate of 1 Moz of Au (Treasury Metals Inc. website, October 2022). Mineralization was emplaced within competent granodioritic and gabbroic intrusions during sinistral transpression along the NE-trending Manitou Dinorwic deformation zone (McCracken, 2019; Zammit et al., 2022). Mineralization is younger in age than that at the Hammond Reef deposit and was emplaced during two events dated at ca. 2672 to ca. 2626 Ma and ca. 2590 Ma to ca. 2580 Ma (U-Pb xenotime; Zammit et al., 2022). Sinistral transcurrent movement on another major NE-trending shear zone, the Miniss River fault, is dated at ca. 2681 Ma (Bethune et al., 2006). Although no significant gold deposits have been located along this fault, NE-trending sinistral faults and shear zones within the western Wabigoon underwent multiple shearing and hydrothermal events and are therefore highly prospective structures for the discovery of new gold deposits.

## 2.6 Conclusions

The Hammond Reef deposit formed along a contractional step-over-zone between two regional sinistral transcurrent faults of the MSS. Compression across this zone resulted in more fracturing that localize the formation of breccias, the migration of hydrothermal fluids, and the precipitation and concentration of gold mineralization. Step-over-zones may control mineralization and the formation of vein systems as pulses of high-pressure fluids originating from breached fluid reservoirs along the main transcurrent faults, are injected in the step-over-zones, creating breccias and reactivating fractures and faults (Micklethwaite and Cox, 2006; Micklethwaite et al., 2010). What caused the formation and localization of step-over-zones requires further research. At the Hammond Reef deposit, the early chlorite-carbonate alteration may have changed the mechanical properties of the rocks, creating a large zone of weakness which arrested the propagation of the main transcurrent faults and resulted in the formation of a step-over-zone. Although speculative, this hypothesis may help explain the location of gold deposits along the major NE-trending faults and shear zones that transect the Wabigoon subprovince.

# References

Ayer, J.A., and Dostal, J., 2000, Nd and Pb isotopes from the Lake of the Woods greenstone belt, northwestern Ontario: implications for mantle evolution and the formation of crust in the southern Superior Province: Canadian Journal of Earth Sciences, v. 37, no. 12, p. 1677–1689.

Backeberg, N.R., 2015,Damaged Goods: Regional deformation history and structural controls on the Hammond Reef gold deposit, Atikokan, Ontario: Ph.D. Thesis, Montreal, Canada, McGill University.

Backeberg, N.R., Rowe, C.D., and Barshi, N., 2016, Alteration-weakening leading to localized deformation in a damage aureole adjacent to a dormant shear zone: Journal of Structural Geology, v. 90, p. 144–156.

Bakke, A.A., 1995, The Fort Knox “porphyry” gold deposit - Structurally controlled and shear quartz vein, sulphide-poor mineralization hosted by a Late Cretaceous pluton, east-central Alaska: Porphyry Deposits of the Northwestern Cordillera of North America, Mining Metals, v. 46, p. 795–802.

Bethune, K.M., Helmstaedt, H.H., and McNicoll, V.J., 2006, Structural analysis of the Miniss River and related faults, western Superior Province: post-collisional displacement initiated at terrane boundaries: Canadian Journal of Earth Sciences, v. 43, no. 7, p. 1031–1054.

Bigot, L., and Jébrak, M., 2015, Gold mineralization at the syenite-hosted Beattie gold deposit, Duparquet, Neoarchean Abitibi belt, Canada: Economic Geology, v. 110, no. 2, p. 315–335.

Bjorkman, K.E., 2017,4D crust-mantle evolution of the Western Superior Craton: implications for Archaean granite-greenstone petrogenesis and geodynamics: Ph.D. Thesis, Perth, Australia, The University of Western Australia: p. 317.

Blackburn, C.E., Johns, G.W., Ayer, J., and Davis, D.W., 1991, Wabigoon subprovince (P.C. Thurston, H.R. Williams, H.R. Sutcliffe, & G.M. Stott, Eds.): Ontario Geological Survey, v. 4, Part 1, p. 303–381.

Buse, S., Lewis, D., Davis, D.W., and Hamilton, M.A., 2010, U/Pb Geochronological Results from the Lumby Lake Greenstone Belt, Wabigoon Subprovince, Northwestern Ontario: Ontario Geological Survey.

Corfu, F., and Davis, D.W., 1992, A U-Pb geochronological framework for the western Superior Province, Onta, in Thurston, P.C., Williams, H.R., Sutcliffe, R.H., and Stott, G.M. eds., Geology of Ontario: Ontario Geological Survey, Special:, p. 1335–1346.

Cox, S.F., 1999, Deformational controls on the dynamics of fluid flow in mesothermal gold systems: Geological Society of London Special Publication, v. 155, p. 123–140.

Cox, S.F., 2010, The application of failure mode diagrams for exploring the roles of fluid pressures and stress states in controlling styles of fracture-controlled permeability enhancement in faults and shear zones: Geofluids, v. 10, p. 217–233.

Cox, S.F., 2016, Injection-driven swarm seismicity and permeability enhancement: Implications for the dynamics of hydrothermal ore systems in high fluid flux, overpressured faulting regimes: Economic Geology, v. 111, p. 559–587.

Cox, S.F., 2020, The dynamics of permeability enhancement and fluid flow in overpressured fracture-controlled hydrothermal system: Reviews in Economic Geology, v. 21, p. 25–82.

Cox, S.F., Knackstedt, M.A., and Braun, J., 2001, Principles of structural control on permeability and fluid flow in hydrothermal systems: Society of Economic Geologists Reviews, v. 14, p. 1–24.

Cox, S.F., and Ruming, K., 2004, The St Ives Mesothermal Gold System, Western Australia – a case of golden aftershocks?: Journal of Structural Geology, v. 26, p. 1109–25.

Crowley, J.L., and Ghent, E.D., 1999, An electron microprobe study of the U–Th–Pb systematics of metamorphosed monazite: the role of Pb diffusion versus overgrowth and recrystallization: Chemical Geology, v. 157, nos. 3–4, p. 285–302.

Davis, D.W., and Jackson, M., 1988, Geochronology of the Lumby Lake greenstone belt: a 3 Ga complex within the Wabigoon Subprovince, northwest Ontario: Geological Society of America Bulletin, v. 100, p. 818–824.

Davis, D.W., and Smith, P.M., 1991, Archean gold mineralization in the Wabigoon Subprovince, a product of crustal accretion: Evidence from U-Pb geochronology in the Lake of the Woods area: Superior Province, Canada: Journal of Geology, v. 99, p. 337–353.

De Souza, S., Dubé, B., McNicoll, V. J., Dupuis, C., Mercier-Langevin, P., Creaser, R. A., & Kjarsgaard, I. M., 2015, Geology, hydrothermal alteration, and genesis of the world-class Canadian Malartic stockwork-disseminated Archean gold deposit, Abitibi, Quebec: Targeted geoscience initiative, 4, p. 113-126.

Duuring, P., Cassidy, K.F., and Hagemann, S.G., 2007, Granitoid-associated orogenic, intrusion-related, and porphyry style metal deposits in the Archean Yilgarn Craton, Western Australia: Ore Geology Reviews, v. 32, nos. 1–2, p. 157–186.

Ferguson, S.A., Groen, H.A., and Haynes, R., 1971, Gold Deposits of Ontario, Part 1, Districts of Algoma, Co chrane, Kenora, Rainy River, and Thunder Bay, in Ontario Department of Mines and Northern Affairs: Mineral Resources Circular, v. 13, p. 315.

Foster, M., 1962. Interpretation of the composition and classification of chlorites: Washington: US Depart. Of the Interior, Geology Survey p. 33.

Fougerouse, D., Micklethwaite, S., Tomkins, A.G., Mei, Y., Kilburn, M., Guagliardo, P., Fisher, L.A., Halfpenny, A., Gee, M., Paterson, D., and Howard, D.L., 2016, Gold remobilisation and formation of high grade ore shoots driven by dissolution-reprecipitation replacement and Ni substitution into auriferous arsenopyrite: Geochimica et Cosmochimica Acta, v. 178, p. 143–159.

Gerstenberger, H., and Haase, G., 1997, A highly effective emitter substance for mass spectrometric Pb isotope ratio determinations: Chemical Geology, v. 136, p. 309–312.

Gold Fields Updated Mineral Resource Estimate at St. Ives Gold Mine. 2018. Available at : https://www.goldfields.com/reports/annual-report-2018/mrr/australia-st-ives-gold-mine.php [November 15, 2022].

Goldfarb, R.J., and Groves, D.I., 2015, Orogenic gold: Common or evolving fluid and metal sources through time: Lithos, v. 233, p. 2–26.

Gratier, J.P., and Gueydan, F., 2007, Effect of fracturing and fluid–rock interaction on seismic cycles, in Tectonic Faults: Agents of Change on a Dynamic Earth:, p. 319-356.

Groves, D.I., Goldfarb, R.J., Gebre-Mariam, M., Hagemann, S.G., and Robert, F., 1998, Orogenic gold deposits: a proposed classification in the context of their crustal distribution and relationship to other gold deposit types: Ore Geology Reviews, v. 13, nos. 1–5, p. 7–27.

Hastie, E.C., Kontak, D.J., and Lafrance, B., 2020, Gold remobilization: insights from gold deposits in the Archean Swayze greenstone belt, Abitibi Subprovince, Canada: Economic Geology, v. 115, no. 2, p. 241–277.

Hattori, K., 1987, Magnetic felsic intrusions associated with Canadian Archean gold deposits: Geology, v. 15, no. 12, p. 1107–1111.

Horstwood, M.S.A., Koˇsler, J., Gehrels, G., Jackson, S.E., McLean, N.M., Paton, C., Pearson, N.J., Sircombe, K., Sylvester, P., Vermeesch, P., Bowring, J.F., Condon, D.J., and Schoene, B., 2016, Community-derived standards for LA-ICP-MS U-(Th-) Pb geochronology–Uncertainty propagation, age interpretation and data reporting: Geostandards and Geoanalytical Research, v. 40, no. 3, p. 311–332.

Ishikawa, Y., Sawaguchi, T., Iwaya, S., and Horiuchi, M., 1976, Delineation of prospecting targets for Kuroko deposits based on modes of volcanism of underlying dacite and alteration haloes: Mining Geology, v. 26, no. 136, p. 105–117.

Jaffey, A.H., Flynn, K.F., Glendenin, L.E., Bentley, W.C., and Essling, A.M., 1971, Precision measurement of half-lives and specific activities of 235U and 238U: Physical Review, v. 4, p. 1889–1906.

Jarosewich, E., 1972, Chemical analysis of five minerals for microprobe standards: Smithsonian Contributions to the Earth Sciences, v. 9, p. 83–84.

Jarosewich, E., Nelen, J.A., and Norberg, J.A., 1980, Reference Samples for Electron Microprobe Analysis: Geostandards Newsletter, v. 4, p. 43–47.

Kerrich, R., 1991, Radiogenic isotope systems applied to mineral deposits, in Heaman, L. and Ludden, J.N. eds., Applications of Radiogenic Isotope Systems to Problems in Geology. Mineralogical Association Canada, Short Course Handbook:, p. 365-421.

King, G.C., Stein, R.S., and Lin, J., 1994, Static stress changes and the triggering of earthquakes: Bulletin of the Seismological Society of America, v. 84, p. 567–585.

Kolb, M.J., 2010,A microstructural study of Musselwhite Mine and Hammond Reef shear-zone-hosted gold deposits: M. Sc. thesis, Thunder Bay, Canada, Lakehead University. http://knowledgecommons.lakeheadu.ca/handle/2453/767

Krogh, T.E., 1973, A low contamination method for hydrothermal decomposition of zircon and extraction of U and Pb for isotopic age determinations: Geochimica et Cosmochimica Acta, v. 37, p. 485–494.

Kwong, Y.T.J., and Crocket, J.H., 1978, Background and anomalous gold in rocks of an Archean greenstone assemblage, Kakagi Lake area, northwestern Ontario: Economic Geology, v. 73, no. 1, p. 50–63.

Large, R.R., Gemmell, J.B., Paulick, H., and Huston, D.L., 2001, The alteration box plot: A simple approach to understanding the relationship between alteration mineralogy and lithogeochemistry associated with volcanic-hosted massive sulfide deposits: Economic geology, v. 96, no. 5, p. 957–971.

Larocque, A.C.L., Hodgson, C.J., Cabri, L.J., and Jackman, J.A., 1995, Ion microprobe analysis of pyrite, chalcopyrite and pyrrhotite from the Mobrun VMS deposit in northwestern Quebec: Evidence for metamorphic remobilization of gold: The Canadian Mineralogist, v. 33, p. 373–388.

Legault, M., and Daigneault, R., 2006, Synvolcanic gold mineralization within a deformation zone: the Chevrier deposit, Chibougamau, Abitibi Subprovince, Canada: Mineralium Deposita, v. 41, no. 3, p. 203–228.

Ludwig, K.R., 2009. User’s manual for Isoplot 3.71 a geochronological toolkit for Excel. Berkeley Geochronological Center Special Publication 4, p. 72.

Ma, C., Naghizadeh, M., Adetunji, A., Lodge, R., Snyder, D.B., and Sherlock, R., 2021, Imaging Neoarchean crustal structures: An integrated geologic-seismic-magnetotelluric study in the western Wabigoon and Winnipeg River terranes, Superior craton: Precambrian Research, v. 364. p. 106

Ma, C., Marsh, J., Lodge, R.W., and Sherlock, R., 2022, Crustal growth/reworking and stabilization of the western Superior Province: Insights from a Neoarchean gneiss complex of the Winnipeg River terrane: Geological Society of America Bulletin. https://doi.org/10.1130/B36441.1

MacLachlan, K., Rayner, N., Dunning, G., and Leugner, C., 2004, New results and ideas from the Rottenstone Domain project, in Summary of Investigations 2004 [CD-ROM],Misc. Report 2004 Industry Resources, Saskatchewan Geological. Survey., Saskatchewan, Canada vol. 2, p. 21.

MacLean, W.H., 1990, Mass change calculations in altered rock series: Mineralium Deposita, v. 25, no. 1, p. 44–49.

Martin, R.D., 2012,Syenite-Hosted gold Mineralization and Hydrothermal Alteration at the Young-Davidson Deposit, Matachewan, Ontario: M. Sc. thesis, Waterloo, ON, Canada, University of Waterloo. http://hdl.handle.net/10012/6677

Mathieu, L., 2021, Intrusion-Associated Gold Systems and Multistage Metallogenic Processes in the Neoarchean Abitibi Greenstone Belt: Minerals, v. 11, no. 3, p. 261.

Mattinson, J., 2005, Zircon U-Pb chemical abrasion (CA-TIMS) method: Combined annealing and multi-step partial dissolution analysis for improved precision and accuracy of zircon ages: Chemical Geology, v. 220, p. 47–66.

McCracken, T., 2019, Technical report and resource estimation update: Goldlund gold project, Sioux Lookout, Ontario: p. 198.

McDivitt, J.A., Kontak, D.J., and Lafrance, B., 2021, A trace metal, stable isotope (O. H & S., Eds.): Mineralium Deposita, v. 56, p. 561–582.

McNaughton, N.J., Rasmussen, B., and Fletcher, I.R., 1999, SHRIMP uranium-lead dating of diagenetic xenotime in siliciclastic sedimentary rocks: Science, v. 285, no. 5424, p. 78–80.

McRea, M., 2022,Chemostratigraphy and structural framework for gold mineralization at the Goliath Deposit, Western Wabigoon Subprovince, Ontario: M. Sc. Thesis, Sudbury, Canada, Laurentian University. https://zone.biblio.laurentian.ca/handle/10219/3928

Mériaud, N., and Jébrak, M., 2017, From intrusion-related to orogenic mineralization: the Wasamac deposit, Abitibi Greenstone Belt, Canada: Ore Geology Reviews, v. 84, p. 289–308.

Micklethwaite, S., 2010, Active fault and shear processes and their implications for mineral deposit formation and discovery: Journal of Structural Geology, v. 32, p. 151–165.

Micklethwaite, S., and Cox, S.F., 2006, Progressive fault triggering and fluid flow in aftershock domains: examples from mineralized Archaean fault systems: Earth and Planetary Science Letters, v. 250, p. 318–330.

Montsion R.M., Thurston. P., and Ayer, J., 2018. 1:2 000 000 Scale Geological Compilation of the Superior Craton – Version 1. Mineral Exploration Research Centre, Harquail School of Earth Sciences, Laurentian University Document Number MERC-ME-2018-017 https://merc.laurentian.ca/sites/default/files/superiormap_8x11_2018.pdf

New Gold Inc. (February 4, 2015a) Summary of Mineral Reserve and Mineral Resource Estimates. New Gold Inc. news release. http://www.newgold.com/investors/reserves-and-resources/default.aspx

Nguyen, T.P., 1997,Structural controls on gold mineralisation at the Revenge Mine and its tectonic setting in the Lake Lefroy area, Kambalda, Western Australia: Ph.D. thesis, Perth, Australia, University of Western Australia. p. 155.

Osisko, 2013, Executive summary: Hammond Reef gold project. Technical report., Osisko Mining Corporation.

Pachell, M.A., and Evans, J.P., 2002, Growth, linkage, and termination processes of a 10-km-long strike-slip fault in jointed granite: the Gemini fault zone, Sierra Nevada, California: Journal of Structural Geology, v. 24, p. 1903–1924.

Paton, C., Hellstrom, J., Paul, B., Woodhead, J., and Hergt, J., 2011, Iolite: Freeware for the visualisation and processing of mass spectrometric data: Journal of Analytical Atomic Spectrometry, v. 26, no. 12, p. 2508–2518.

Pelletier, M., 2016,The rainy river gold deposit, Wabigoon subprovince, western ontario: style, geometry, timing and structural controls on ore distribution and grades: M. Sc. Thesis, Quebec City, Canada, Université du Québec.

Percival, J. A. (2007a). Eo- to Mesoarchean terranes of the Superior Province and their tectonic context, in Van Kranendonk, M. J., Smithies, R. H., and Bennet V. C. , ed., Earth's Oldest Rocks. v. 15, Developments in Precambrian Geology, p. 1065– 1085.

Percival, J.A., 2007b, Geology and metallogeny of the Superior Province, Canada (W.D. Goodfellow, Ed.): Geological Association of Canada, Mineral Deposits Division, Special Publication, no. 5, p. 903–928.

Percival, J.A., and Helmstaedt, H., 2004, Insights on Archean continent-ocean assembly, western Superior Province, from new structural, geochemical and geochronological observations: Introduction and summary: Precambrian Research, v. 132, p. 209–212.

Percival, J.A., Sanborn-Barrie, M., Skulski, T., Stott, G.M., Helmstaedt, H., and White, D.J., 2006, Tectonic evolution of the western Superior Province from NATMAP and Lithoprobe studies: Canadian Journal of Earth Sciences, v. 43, no. 7, p. 1085–1117.

Petrus, J.A., and Kamber, B.S., 2012, VizualAge: A novel approach to laser ablation ICP-MS U-Pb geochronology data reduction: Geostandards and Geoanalytical Research, v. 36, no. 3, p. 247–270.

Phillips, G.N., 1986, Geology and alteration in the Golden Mile, Kalgoorlie: Economic Geology, v. 81, no. 4, p. 779–808.

Poulsen, K.H., Robert, F., and Dubé, B., 2000, Geological classification of Canadian gold deposits: Geological Survey of Canada Bulletin, v. 540, no. 106.

Proudlove, D. C., Hutchinson, R. W., and Rogers, D. S., 1989, Multiphase mineralization in concordant and discordant gold veins, Dome mine, South Porcupine, Ontario, Canada. https://doi.org/10.5382/Mono.06.08

Robert, F., and Brown, A.C., 1986, Archean gold-bearing quartz veins at the Sigma Mine, Abitibi greenstone belt, Quebec; Part I, Geologic relations and formation of the vein system: Economic Geology, v. 81, no. 3, p. 578–592.

Robert, F., Boullier, A. M., and Firdaous, K., 1995, Gold-quartz veins in metamorphic terranes and their bearing on the role of fluids in faulting: Journal of Geophysical Research, v. 100, p. 12,861-12,879.

Robert, F., and Poulsen, K.H., 2001, Structural controls on veins in gold deposits in metamorphic rocks: Reviews in Economic Geology, v. 14, p. 111–156.

Saeki, Y., and Date, J., 1980, Computer application to the alteration data of the footwall dacite lava at the Ezuri Kuroko deposits, Akita prefecture: Mining Geology, v. 30, no. 162, p. 241–250.

Sanborn-Barrie, M., and Skulski, T., 2006, Sedimentary and structural evidence for 2.7 Ga continental arc–oceanic arc collision in the Savant–Sturgeon greenstone belt, western Superior Province: Canada: Canadian Journal of Earth Sciences, v. 43, p. 995-1030.

Sibson, R.H., 2020, Preparation zones for large crustal earthquakes consequent on fault-valve action: Earth, Planets and Space, v. 72, no. 1, p. 1–20.

Sibson, R.H., Robert, F., and Poulsen, K.H., 1988, High-angle reverse faults, fluid-pressure cycling, and mesothermal gold deposits: Geology, v. 16, p. 551–555.

Smith, H.A., and Giletti, B.J., 1997, Lead diffusion in monazite: Geochimica et Cosmochimica Acta, v. 61, no. 5, p. 1047–1055.

Spitz, G., and Darling, R., 1978, Major and minor element lithogeochemical anomalies surrounding the Louvem copper deposit, Val d’Or, Quebec: Canadian Journal of Earth Sciences, v. 15, no. 7, p. 1161–1169.

Stacey, J.S., and Kramers, J.D., 1975, Approximation of terrestrial lead isotope evolution by a two-stage model: Earth and Planetary Science Letters, v. 26, p. 207–221.

Stern, R.A., and Rayner, N.M., 2003, Ages of several xenotime megacrysts by ID-TIMS: Potential reference materials for ion microprobe U-Pb geochronology: Natural Resources Canada, Geological Survey of Canada, p. 7.

Stone, D., 2008, Precambrian geology, Atikokan Area, Preliminary Map – Revised: Technical report, Ontario Geological Survey p.3349

Stone, D., 2010, Precambrian geology of the central Wabigoon subprovince area, northwest Ontario: Ontario Geological Survey. p. 5422

Stone, D. and Kamineni, D. C., 1989, Geology, Atikokan Area, Ontario, Map 1666A, scale 1:50 000: Technical report, Ontario Geological Survey.

Tappert, M.C., Rivard, B., Giles, D., Tappert, R., and Mauger, A., 2013, The mineral chemistry, near-infrared, and mid-infrared reflectance spectroscopy of phengite from the Olympic Dam IOCG deposit, South Australia: Ore Geology Reviews, v. 53, p. 26–38.

Thurston, P.C., Osmani, I.A., and Stone, D., 1991, Northwestern Superior Province: Review and terrane analysis (P.C. Thurston, H.R. Williams, R.H. Sutcliffe, & G.M. Stott, Eds.): Geology of Ontario: Ontario Geological Survey Special Volume, v. 4, Part 1, p. 81–144.

Tilling, R.I., Gottfried, D., and Rowe, J.J., 1973, Gold abundance in igneous rocks; bearing on gold mineralization: Economic Geology, v. 68, no. 2, p. 168–186.

Tomlinson, K.Y., Davis, D.W., Stone, D., and Hart, T., 2003, New U-Pb and Nd isotopic evidence for crustal recycling and Archean terrane development in the south-central Wabigoon Subprovince: Canada: Contributions to Mineralogy and Petrology, v. 144, p. 684–702.

Tomlinson, K.Y., Stone, D., and Hattori, K.H., 2004, Basement terranes and crustal recycling in the western Superior Province: Nd isotopic character of granitoid and felsic volcanic rocks in the Wabigoon subprovince, Ontario, Canada: Precambrian Research, 132 , 245–27.

Tóth, Z., 2019,The geology of the Beardmore-Geraldton belt, Ontario, Canada: geochronology, tectonic evolution and gold mineralization: Ph.D. thesis, Sudbury, Canada, Laurentian University. https://zone.biblio.laurentian.ca/handle/10219/3207

Tóth, Z., McNicoll, V., Lafrance, B., and Dubé, B., 2022, Early depositional and magmatic history of the Beardmore-Geraldton Belt: Formation of a transitional accretionary belt along the Wabigoon-Quetico Subprovince boundary in the Archean Superior Craton, Canada: Precambrian Research, v. 371, p. 106579.

Treasury Metals Announces Updated Mineral Resource Estimate at Goliath Gold Complex. 2022. Available at: https://ca.finance.yahoo.com/news/treasury-metals-announces-updated-mineral-112000531.html [April 14, 2022]

Tremblay, M., 1940, Statistical Review of the Mineral Industry for 1938; Ontario Department of Mines, Annual Report for 1939:, p. 1-54.

Wagner, T., Fusswinkel, T., Wälle, M., and Heinrich, C.A., 2016, Microanalysis of fluid inclusions in crustal hydrothermal systems using laser ablation methods: Elements, v. 12, p. 323–328.

Wheeler, J O; Hoffman, P F; Card, K D; Davidson, A; Sanford, B V; Okulitch, A V; Roest, W R., 1997, Geological map of Canada: Geological Survey of Canada, Map D1860A, *Seymour M. Sears, P. Geo.(APGO# 0413) Consulting Geologist and President Sears Barry & Associates Ltd*. https://doi.org/10.4095/208175)

Wilkinson, S.J., 1982, Gold deposits of the Atikokan area: Ontario Geological Survey, mineral deposits circular v. 24, p. 16.

Williams, M.L., and Jercinovic, M.J., 2002, Microprobe monazite geochronology: putting absolute time into microstructural analysis: Journal of Structural Geology, v. 24, nos. 6–7, p. 1013–1028.

Wintsch, R.P., Christoffersen, R., and Kronenberg, A.K., 1995, Fluid-rock reaction weakening of fault zones: Journal of Geophysical Research: Solid Earth, v. 100, no. B7, p. 13021–13032.

Workman A.W., 1986, Geology of the McDermott Gold Deposit, Kirkland Lake Area, Northeastern Ontario, Canada. In: MacDonald A.J. ed. Proceedings of Gold ’86, an international symposium on the geology of gold. Toronto, p. 184–190.

York, D., 1969, Least-squares fitting of a straight line with correlated errors: Earth and Planetary Science Letters, v. 5, p. 320–324.

Zammit, K., Perrouty, S., Frieman, B.M., Marsh, J.H., and Holt, K.A. Structural and geochronological constraints on orogenic gold mineralization in the western Wabigoon subprovince, Canada.: Canadian Journal of Earth Sciences., v. 59, no. 5, p. 278–299.

Zhang, J., Lin, S., Linnen, R., and Martin, R., 2014, Structural setting of the Young-Davidson syenite-hosted gold deposit in the western Cadillac-Larder Lake deformation zone, Abitibi greenstone belt, Superior Province, Ontario: Precambrian Research, v. 248, p. 39–59.

# Figures

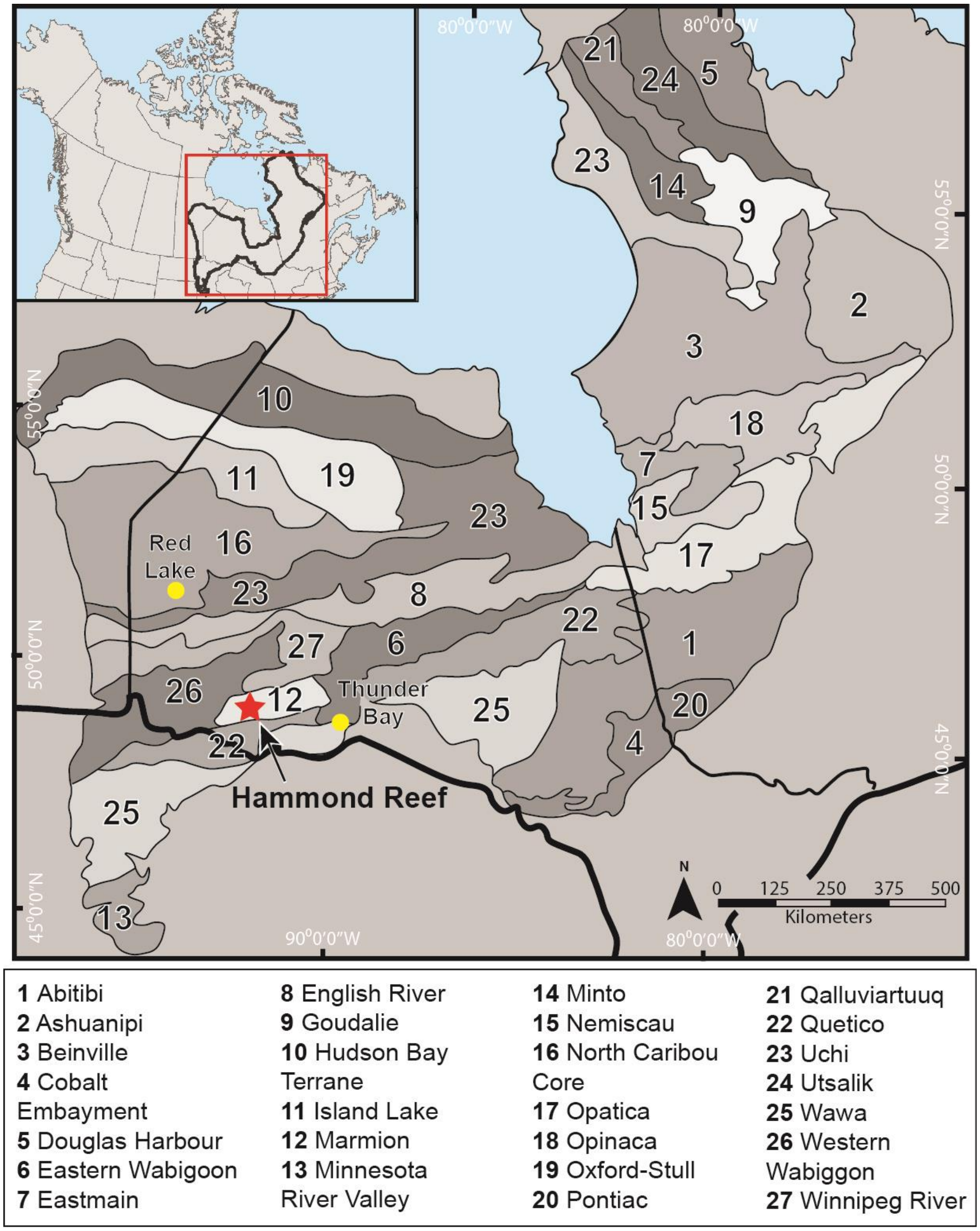

**Figure 1:** Outline of the subprovinces and terranes of the Superior Province (Wheeler et al., 1997; Montsion et al., 2018), with inset map to the top left showing the location of the Superior Province in North America. The Hammond Reef deposit is represented by a red star, and yellow circles are for geographical reference and represent the communities of Red Lake and Thunder Bay.

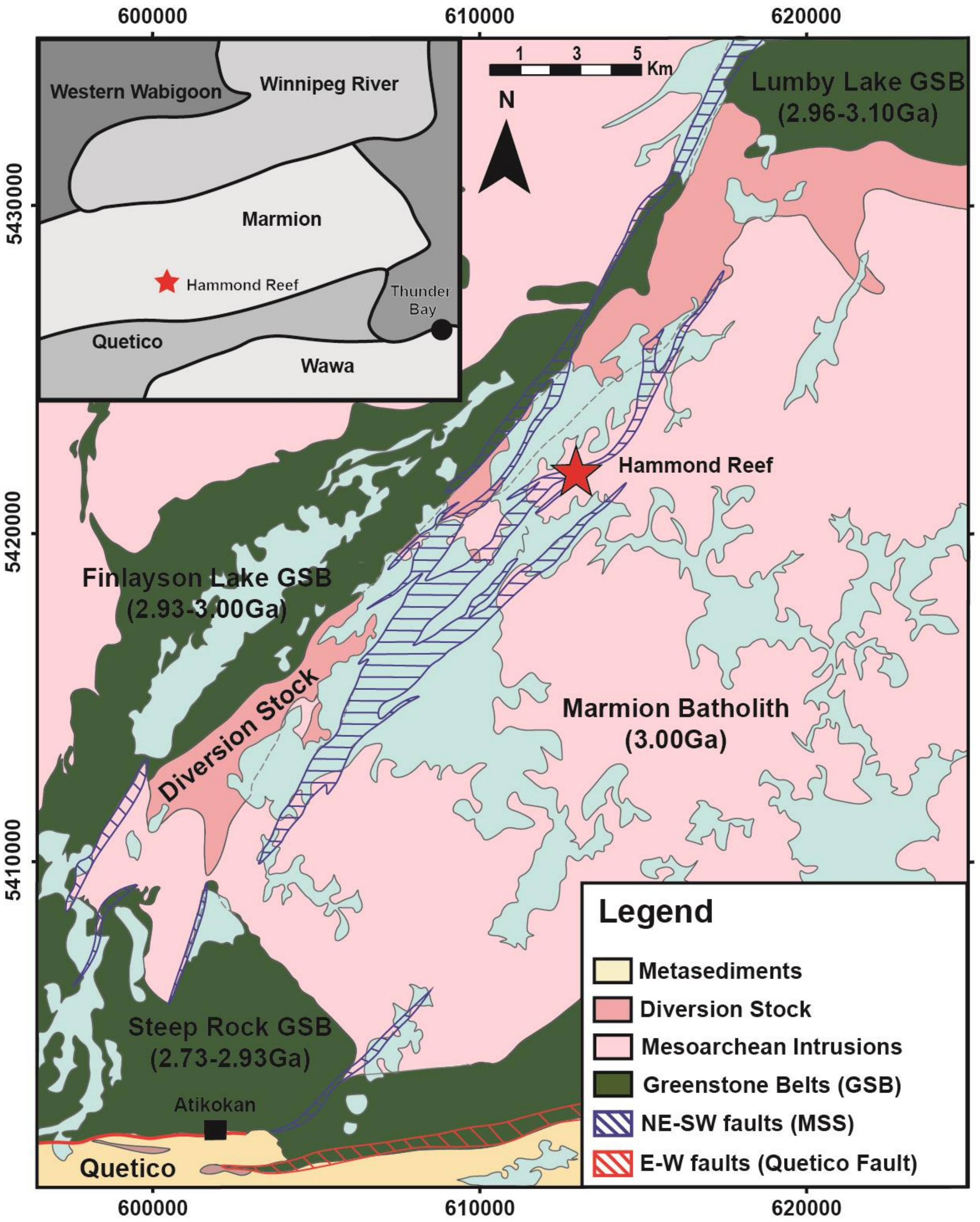

**Figure 2**: Regional map of the MSS showing the location, extent, and orientation of its anastomosing shear zones (Modified from Stone, 2010; Osisko, 2013). Location of the Hammond Reef deposit in the western Superior Province is indicated by a red star on the top left

inset map, which is modified after Montsion et al. (2018). UTM coordinates in NAD83 Zone 15N.

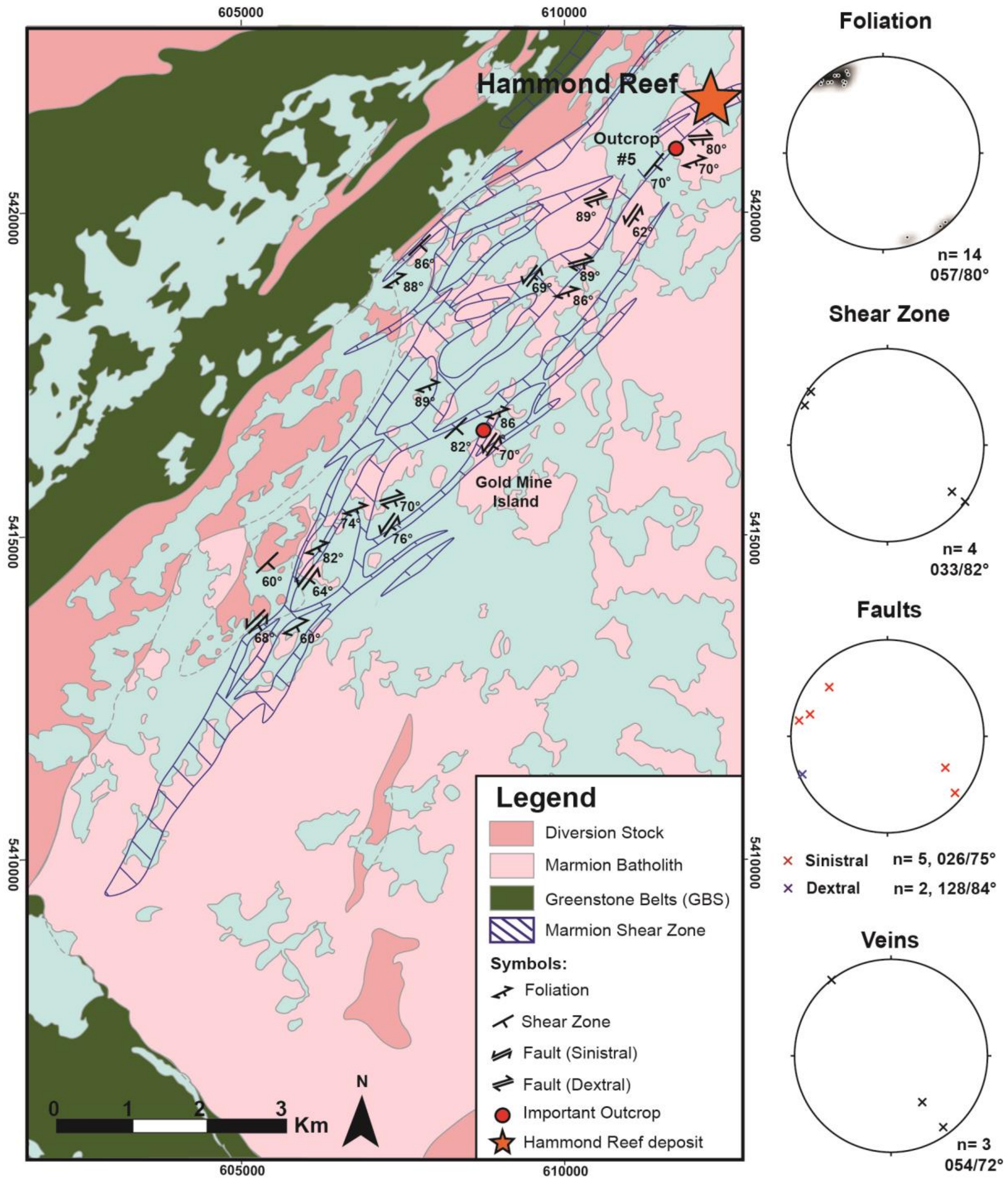

**Figure 3:** Map of the southern domain showing the MSS, with structural measurements and important outcrops discussed in text shown as filled red circles. Contours on upper stereonet diagram are in 2% of total data points per 1% area of the stereonet plots. Foliation, shear zones, conjugate faults and veins are plotted as poles. Number of measurements and average orientation of the plotted structural features at the bottom right of the stereonet plots. NAD83 Zone 15N UTM coordinates.

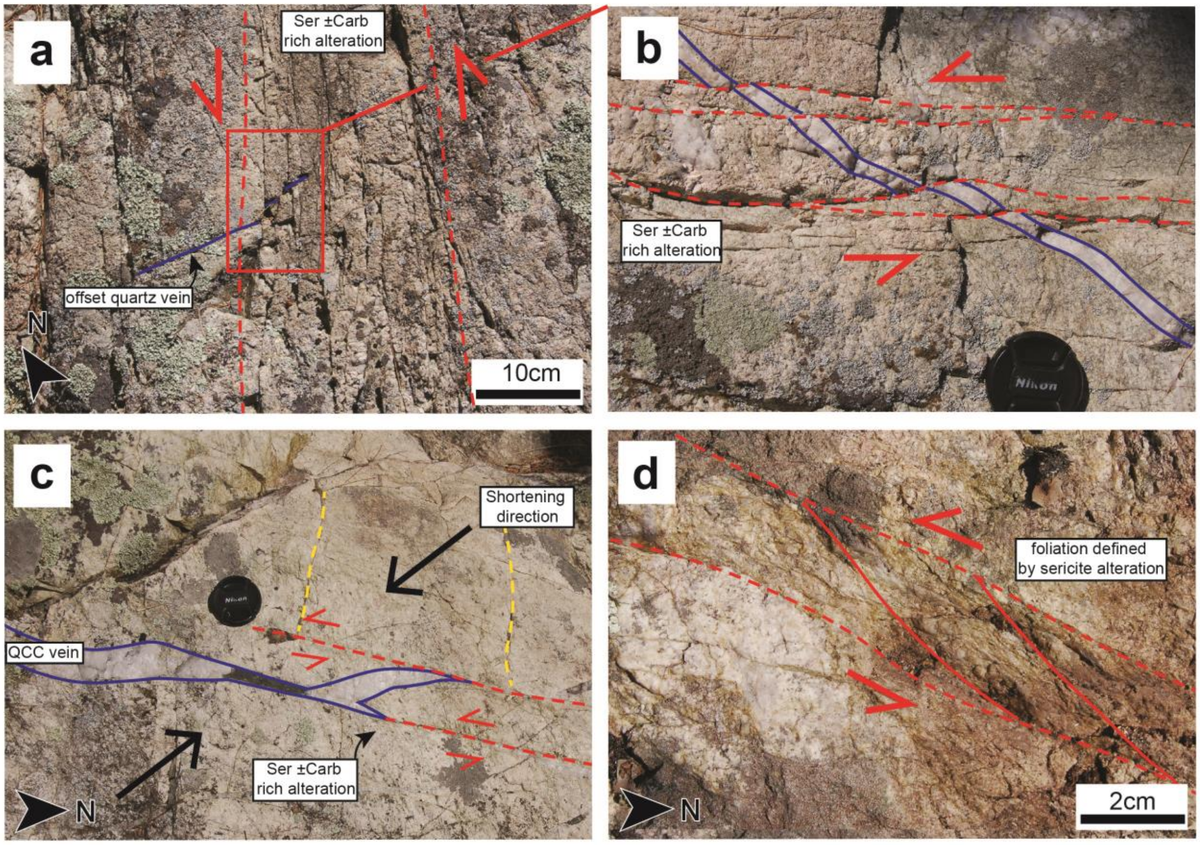

**Figure 4:** Field photographs from Gold Mine Island in the southern domain. a) Zone of closely-spaced sinistral fractures with sericite alteration halos delineated by broken red lines. Quartz vein (blue lines) is sinistrally offset along the fractures (broken red lines). Camera cap (5.8 cm in diameter) for scale. b) Close-up photograph of sinistrally offset quartz vein (blue line) in (a). Fractures are represented by broken red lines. Camera cap (5.8 cm in diameter) for scale. c) Quartz veins (solid blue line) bisecting the angle between two sets of sericite altered shear fractures (broken red line) forming bridges between two fractures (broken yellow lines). Camera cap (5.8 cm in diameter) for scale. d) Foliation (solid red line) defined by sericite alteration. Ser = sericite; Carb = carbonate; QCC = quartz-carbonate-chlorite.

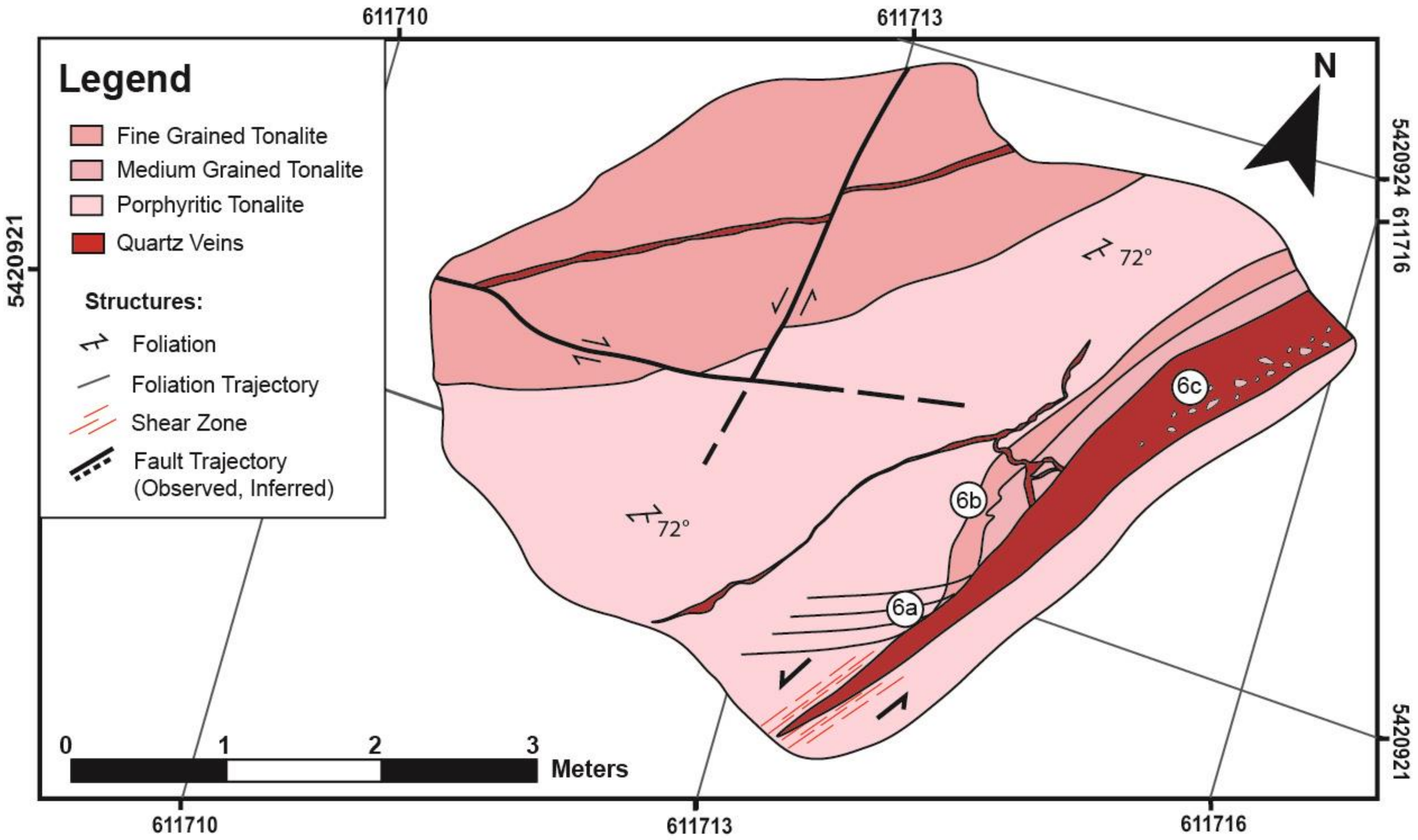

**Figure 5:** Detailed map of Outcrop #5 showing a quartz breccia vein emplaced in a sericitic sinistral shear zone. UTM coordinates NAD83 Zone 15N. Location of outcrop is shown in Figure 3. Encircled numbers and letters 6a, 6b, 6c refer to field photographs shown in Figure 6.

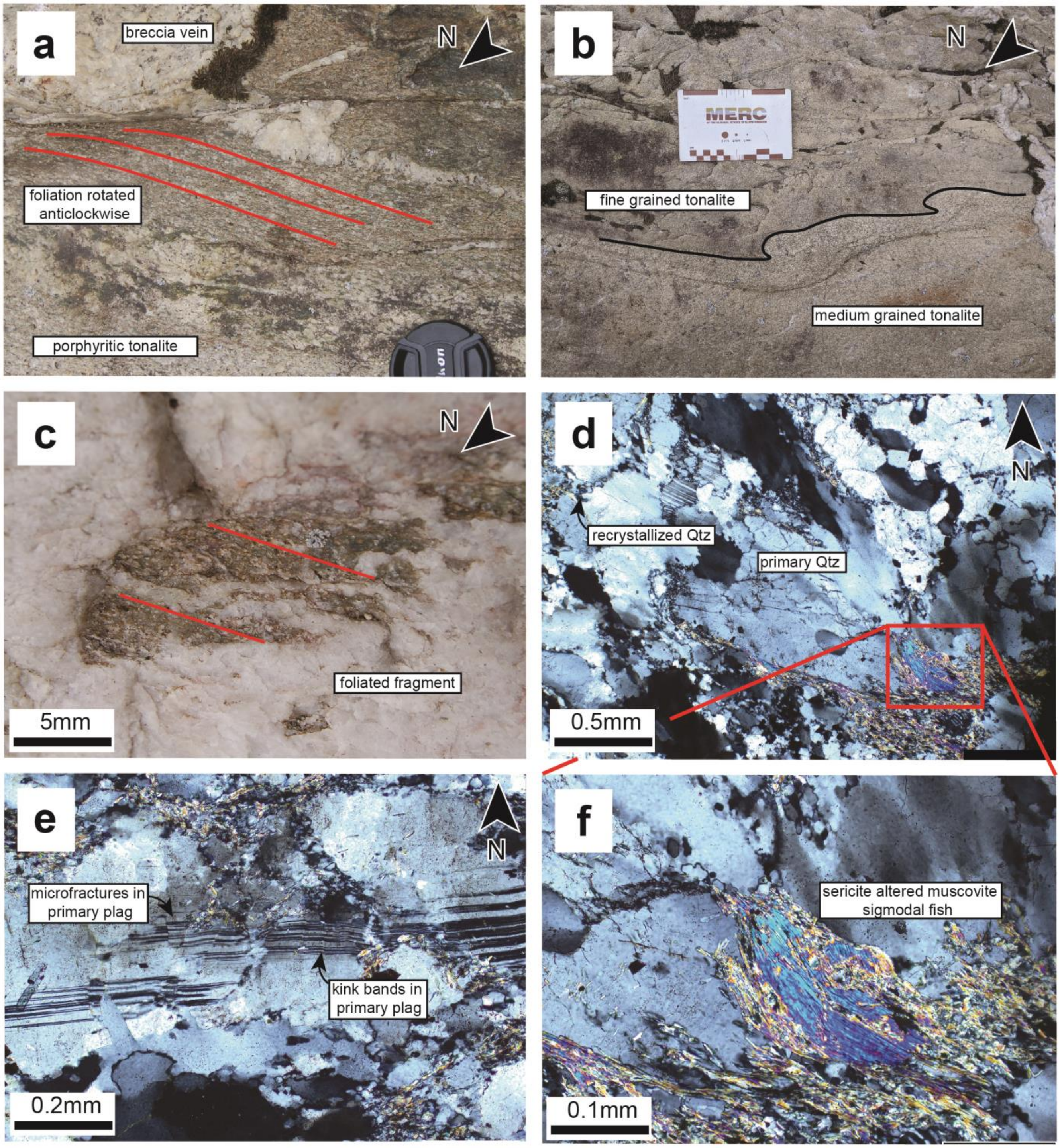
a
breccia vein
N
foliation rotated anticlockwise
porphyritic tonalite
b
N
MERC
fine grained tonalite
medium grained tonalite
c
N
foliated fragment
5mm
d
N
recrystallized Qtz
primary Qtz
0.5mm
e
N
microfractures in primary plag
kink bands in primary plag
0.2mm
f
sericite altered muscovite sigmodal fish
0.1mm

**Figure 6:** Field photographs and photomicrographs from Outcrop #5 in the southern domain. a) Sericitic foliation (solid red line) dragged in anticlockwise manner along quartz breccia vein. Camera cap (5.8 cm in diameter) for scale. b) S-shaped drag folds along contact (solid black line) between medium grained tonalite and fine grained tonalite. Photo card (8.5 cm in length) for scale. c) Foliated host rock fragments within breccia vein. Foliation is represented by solid red line. d) Photomicrograph of porphyritic tonalite comprised dominantly of quartz and feldspar. Quartz shows undulose optical extinction, low angle boundaries, and irregular recrystallized margins, and is surrounded by smaller recrystallized quartz grains and sericite. Crossed polars. e) Photomicrograph of fractured plagioclase with kink bands. Crossed polars. f) Close-up of (e). Primary muscovite partially replaced by finer-grained sericite showing a sigmoidal mica fish geometry indicative of sinistral movement. Crossed polars. Plag = plagioclase; Qtz = quartz. Photograph locations are shown on Fig. 5.

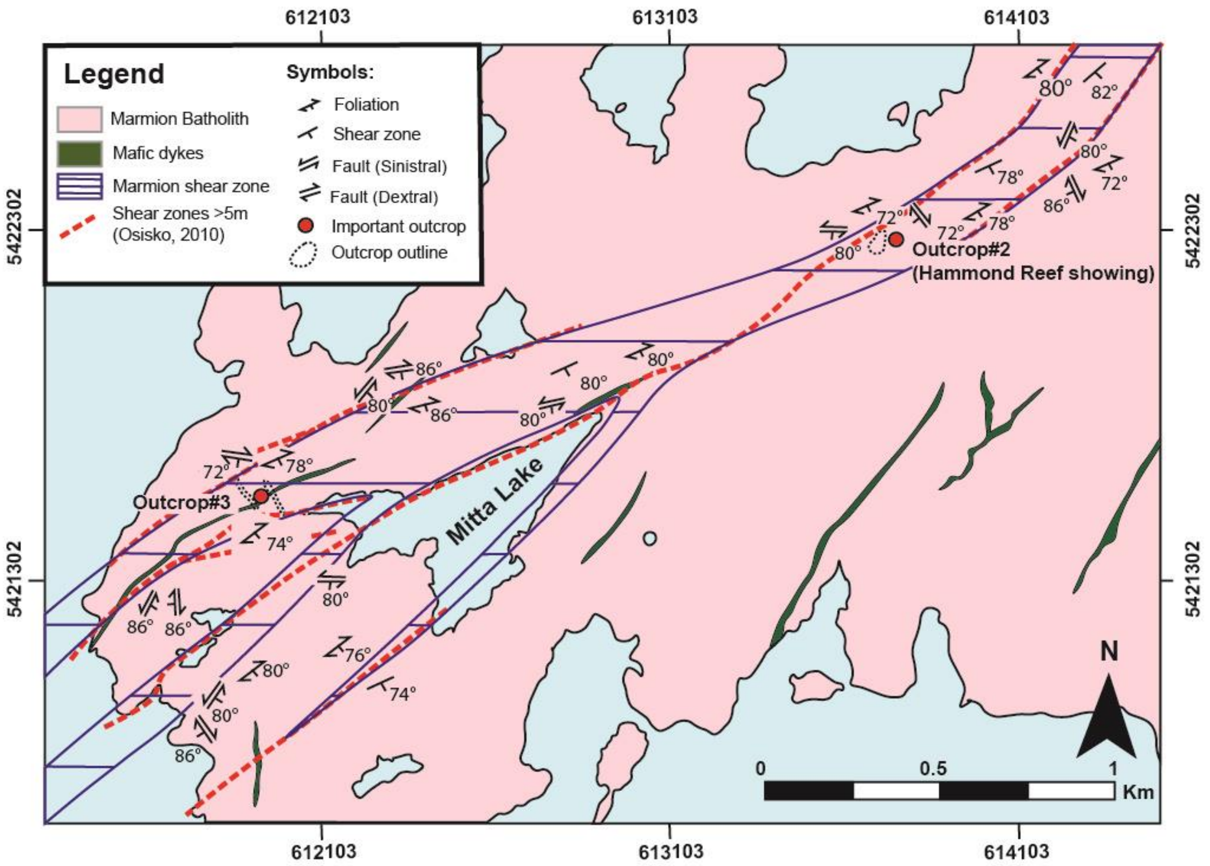
612103
613103
614103
5422302
5421302
Legend
Marmion Batholith
Mafic dykes
Marmion shear zone
Shear zones >5m (Osisko, 2010)
Symbols:
Foliation
Shear zone
Fault (Sinistral)
Fault (Dextral)
Important outcrop
Outcrop outline
Outcrop#2 (Hammond Reef showing)
Outcrop#3
Mitta Lake
80°
82°
78°
72°
86°
74°
76°
N
0
0.5
1
Km

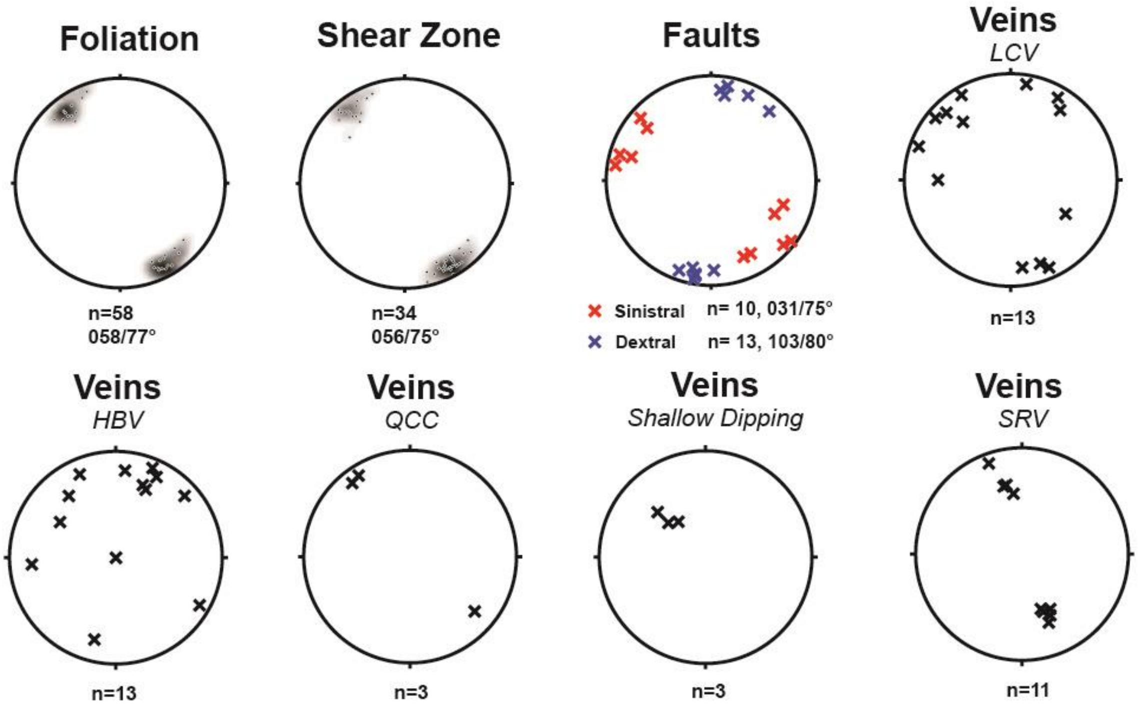
Foliation
n=58
058/77°
Shear Zone
n=34
056/75°
Faults
Sinistral n= 10, 031/75°
Dextral n= 13, 103/80°
Veins
LCV
n=13
Veins
HBV
n=13
Veins
QCC
n=3
Veins
Shallow Dipping
n=3
Veins
SRV
n=11

**Figure 7:** Map of the central domain with the MSS represented by the blue horizontal line pattern. Stereonet plots of poles to foliation, shear zone, conjugate shear fractures, and veins. Number of measurement (n=) and average orientation of structural feature to the lower right of the stereonet plots. Contours are in intervals of 2% of the total data points per 1% area of stereonet. UTM coordinates NAD83 Zone 15N. LCV, laminated crustiform veins; HBV, hydrothermal breccia veins; QCC, quartz chlorite carbonate veins; SRV, sulfide-rich veins.

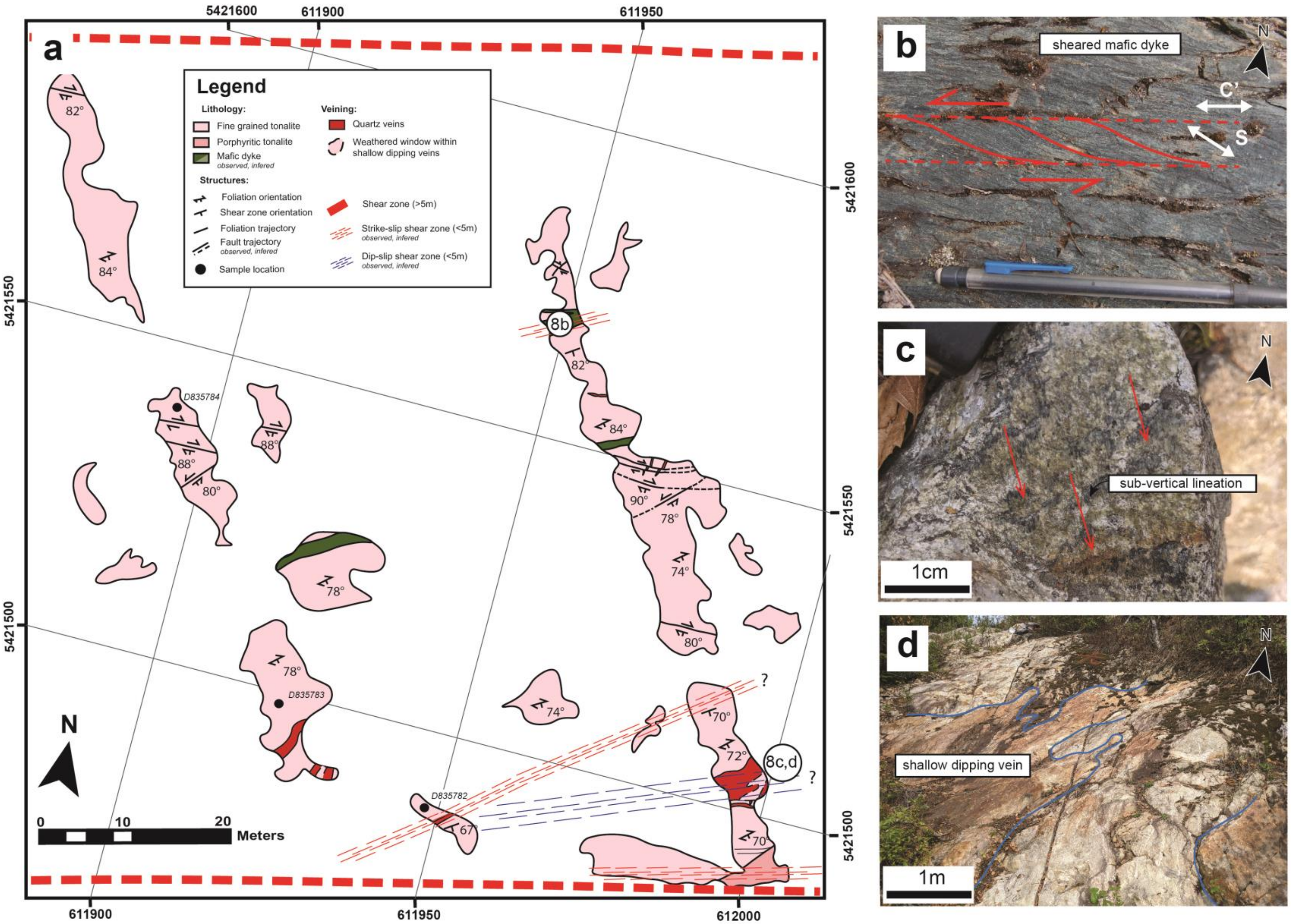
a
Legend
Lithology:
Fine grained tonalite
Porphyritic tonalite
Mafic dyke
observed, infered
Structures:
Foliation orientation
Shear zone orientation
Foliation trajectory
Fault trajectory
observed, infered
Sample location
Veining:
Quartz veins
Weathered window within shallow dipping veins
Shear zone (>5m)
Strike-slip shear zone (<5m)
observed, infered
Dip-slip shear zone (<5m)
observed, infered
5421600
611900
611950
5421550
5421500
612000
8b
8c,d
D835784
D835783
D835782
82°
84°
88°
80°
78°
90°
74°
72°
70°
67°
?
N
0
10
20
Meters
b
sheared mafic dyke
C'
S
N
c
sub-vertical lineation
1cm
N
d
shallow dipping vein
1m
N

**Figure 8:** Map and field photographs of outcrop #3. See Figure 7 for location of outcrop. a) Detailed map of outcrops #3. Map shows dip-slip (blue lines) and sinistral strike-slip (red line) shear zones located in-between two strong lineaments representing major shear zones. UTM coordinates NAD83 Zone 15N. Location of field photographs 8b, 8c, 8d shown on map. b) S-fabric (S) dragged along sinistral shear bands (C') in sheared mafic dike. Pencil (15.4 cm in length) for scale; c) Dip-parallel slickenline (red arrow) along the wall of a shallowly-dipping vein.d) Shallowly-dipping vein outlined by blue solid line.

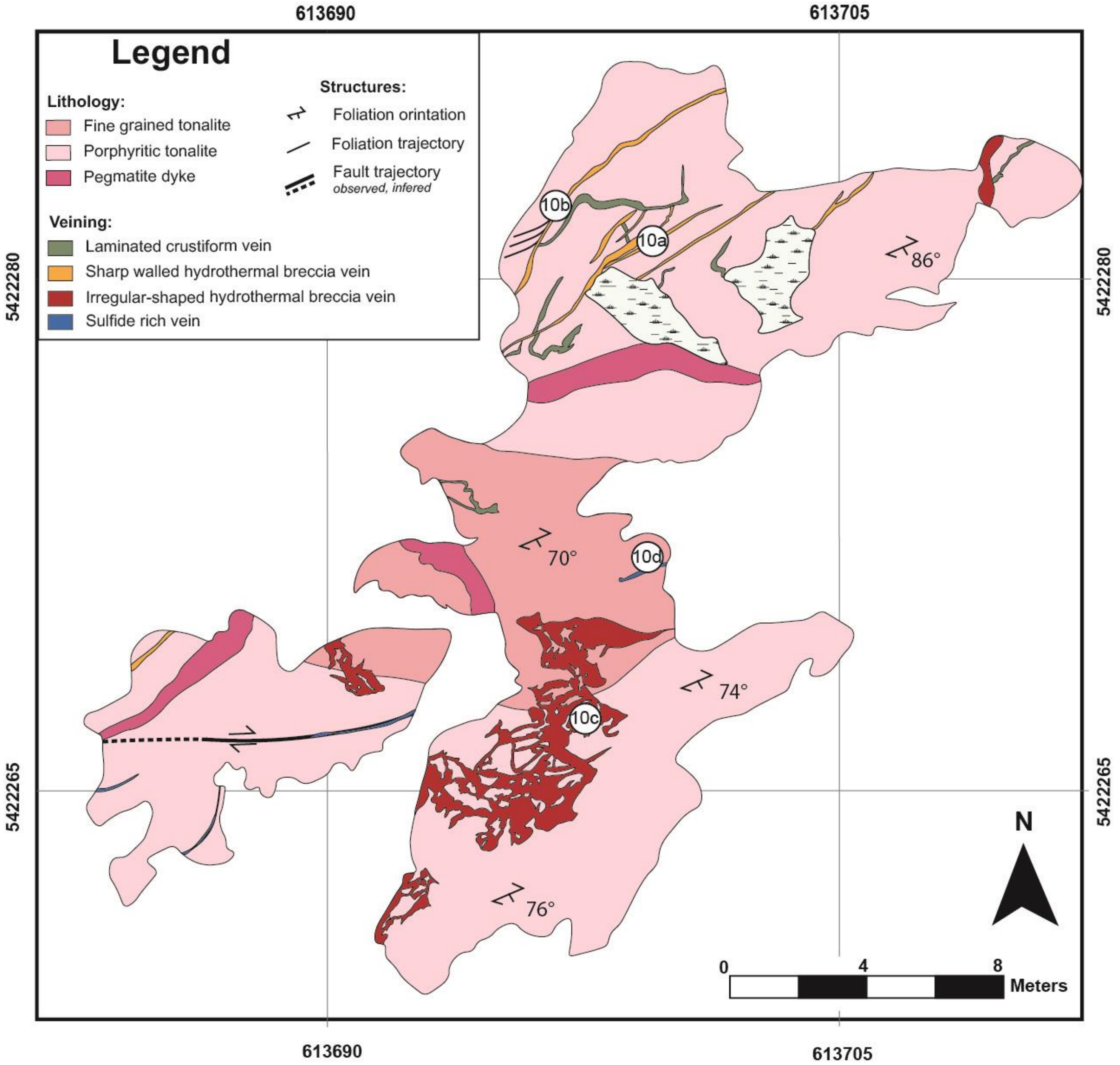

**Figure 9:** Detailed geological map of the Hammond Reef showing which is representative of the Hammond Reef deposit. See Figure 7 for location of outcrop. UTM coordinates NAD83 Zone 15N. Encircled numbers and letters 10a to 10d refer to field photographs shown in Figure 10.

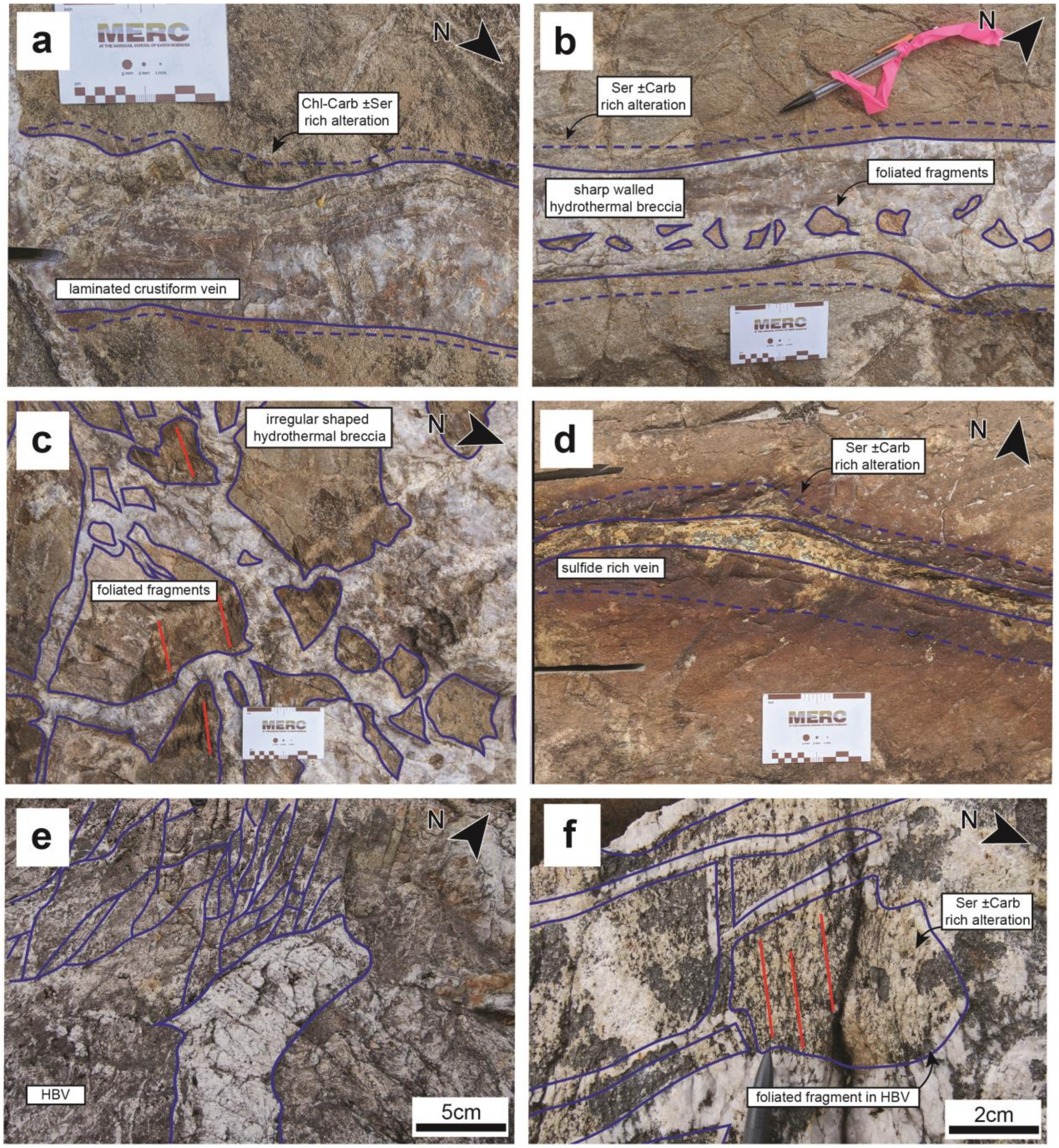
a
N
MERC
Chl-Carb ±Ser rich alteration
laminated crustiform vein
b
N
Ser ±Carb rich alteration
sharp walled hydrothermal breccia
foliated fragments
MERC
c
irregular shaped hydrothermal breccia
N
foliated fragments
MERC
d
N
Ser ±Carb rich alteration
sulfide rich vein
MERC
e
N
HBV
5cm
f
N
Ser ±Carb rich alteration
foliated fragment in HBV
2cm

**Figure 10**: Field photographs from central domain. a) Laminated crustiform vein (solid blue line) with a chlorite-carbonate rich alteration halo (dashed blue line), Hammond Reef prospect. Photo card (8.5 cm in length) for scale; b) Sharp-walled hydrothermal breccia vein (solid blue line) with sericite ±carbonate alteration halo (dashed blue line). Photo card (8.5 cm in length) for scale; c) Irregular-shaped hydrothermal breccia vein with foliated fragments with the foliation represented by solid red line. Photo card (8.5 cm in length) for scale; d) Sulfide-rich vein with a sericite alteration halo. Photo card (8.5 cm in length) for scale. e) hydrothermal breccia vein surrounded by a stockwork of narrow quartz veins represented by blue lines; f) foliated fragments within hydrothermal breccia. HBV, hydrothermal breccia vein. Photograph locations are shown on Figure 9.

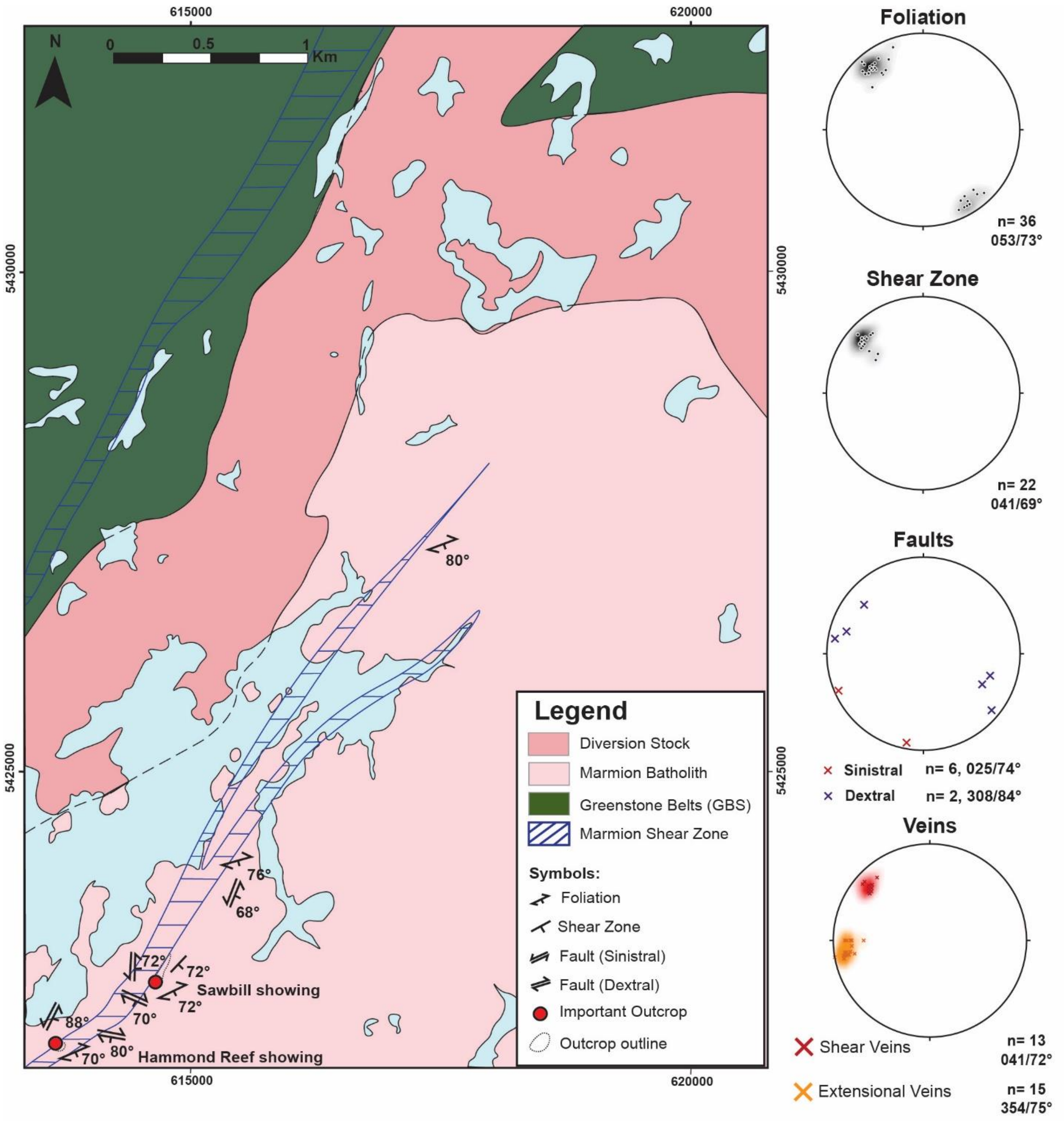

**Figure 11:** Map of the northern domain showing extent and orientation of the MSS. Stereonet plots of poles to foliation, shear zones, faults, and veins. Number of measurement (n=) and average orientation of structural feature to the lower right of the stereonet plots. Contours (1% area) representing density distribution of poles to foliation, shear zone and veins forming syn-deformation at a 2% intervals. Conjugate faults are plotted as poles. UTM coordinates NAD83 Zone 15N.

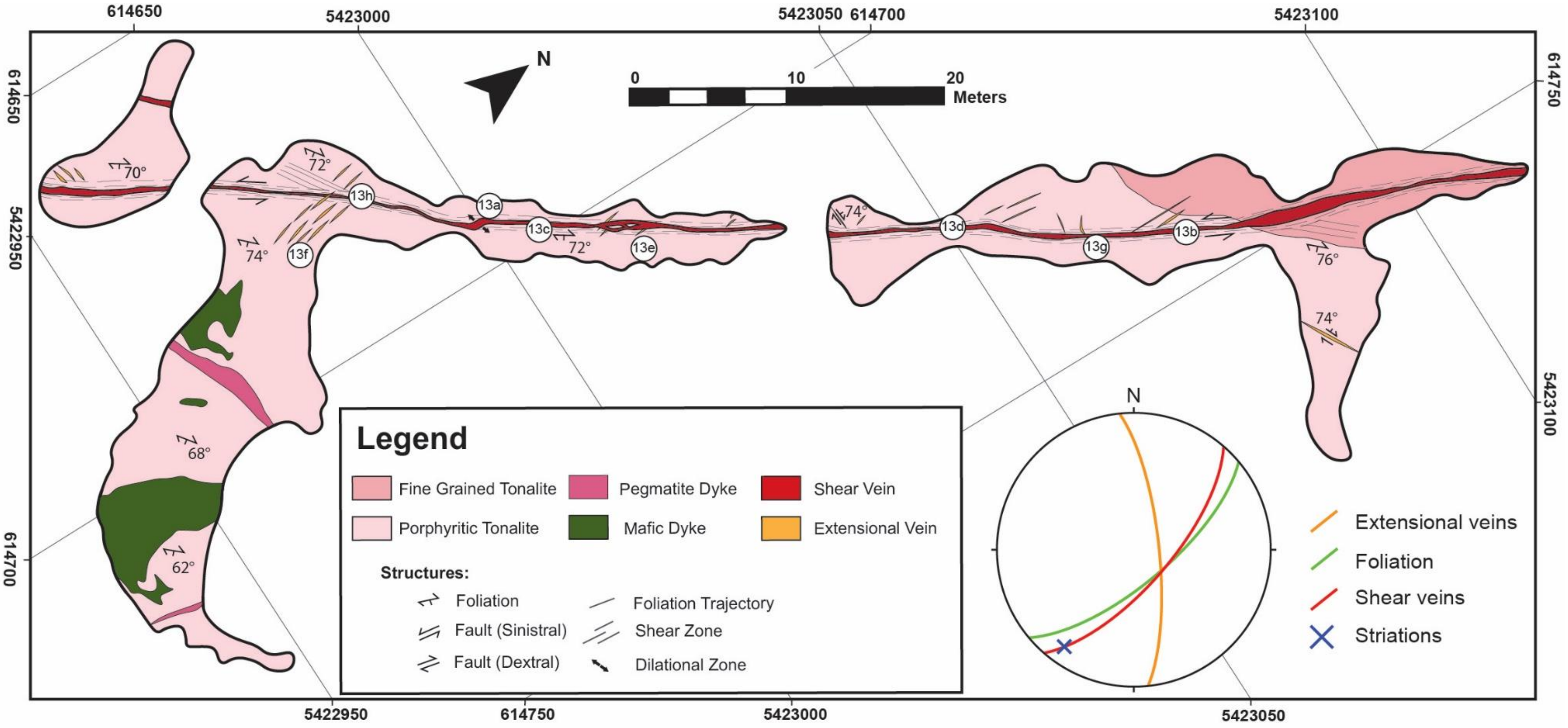

**Figure 12**: Detailed map of the Sawbill showing (outcrop #6) with stereonet showing the average orientation of the shear vein, foliation, extensional quartz veins, and striation along the quartz vein. UTM coordinate NAD83 Zone 15N. See Figure 11 for location of outcrop.

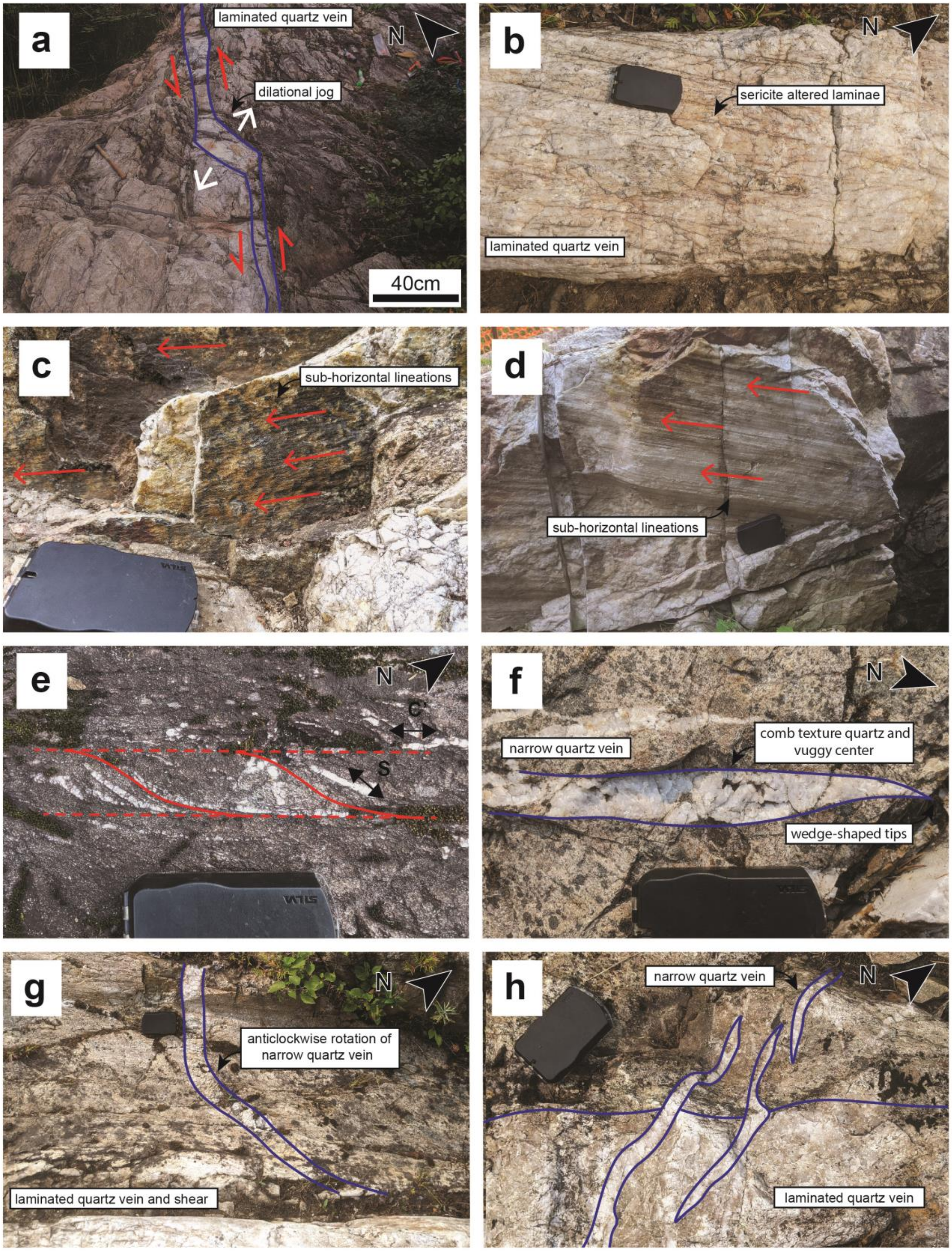
a
laminated quartz vein
N
dilational jog
40cm
b
N
sericite altered laminae
laminated quartz vein
c
sub-horizontal lineations
d
sub-horizontal lineations
e
N
C'
S
f
N
narrow quartz vein
comb texture quartz and vuggy center
wedge-shaped tips
g
N
anticlockwise rotation of narrow quartz vein
laminated quartz vein and shear
h
narrow quartz vein
N
laminated quartz vein

**Figure 13:** Field photographs of the Sawbill vein and outcrop in the northern domain. a) Quartz-filled dilational jog or left-stepping stepover-zone along shear zone indicating sinistral shear. Compass (10 cm in length) for scale. b) Laminated Sawbill vein. Compass (10 cm in length) for scale. c) Sub-horizontal striations along shear planes. Compass (10 cm in length) for scale. d) Sub-horizontal striations along wall of laminated Sawbill vein. Compass (10 cm in length) for scale. e) S-foliation dragged in anticlockwise manner along the C-foliation indicating sinistral shearing. Compass (10 cm in length) for scale. f) Close-up of ESE-trending extensional quartz veins with coarse quartz fibers and vuggy centers. Compass (10 cm in length) for scale. g) ESE-trending extensional quartz vein dragged in anticlockwise manner along the margin of the laminated vein. Compass (10 cm in length) for scale. h) Extensional quartz veins crosscutting laminated quartz vein. Compass (10 cm in length) for scale. Photograph location is shown on Figure 12.

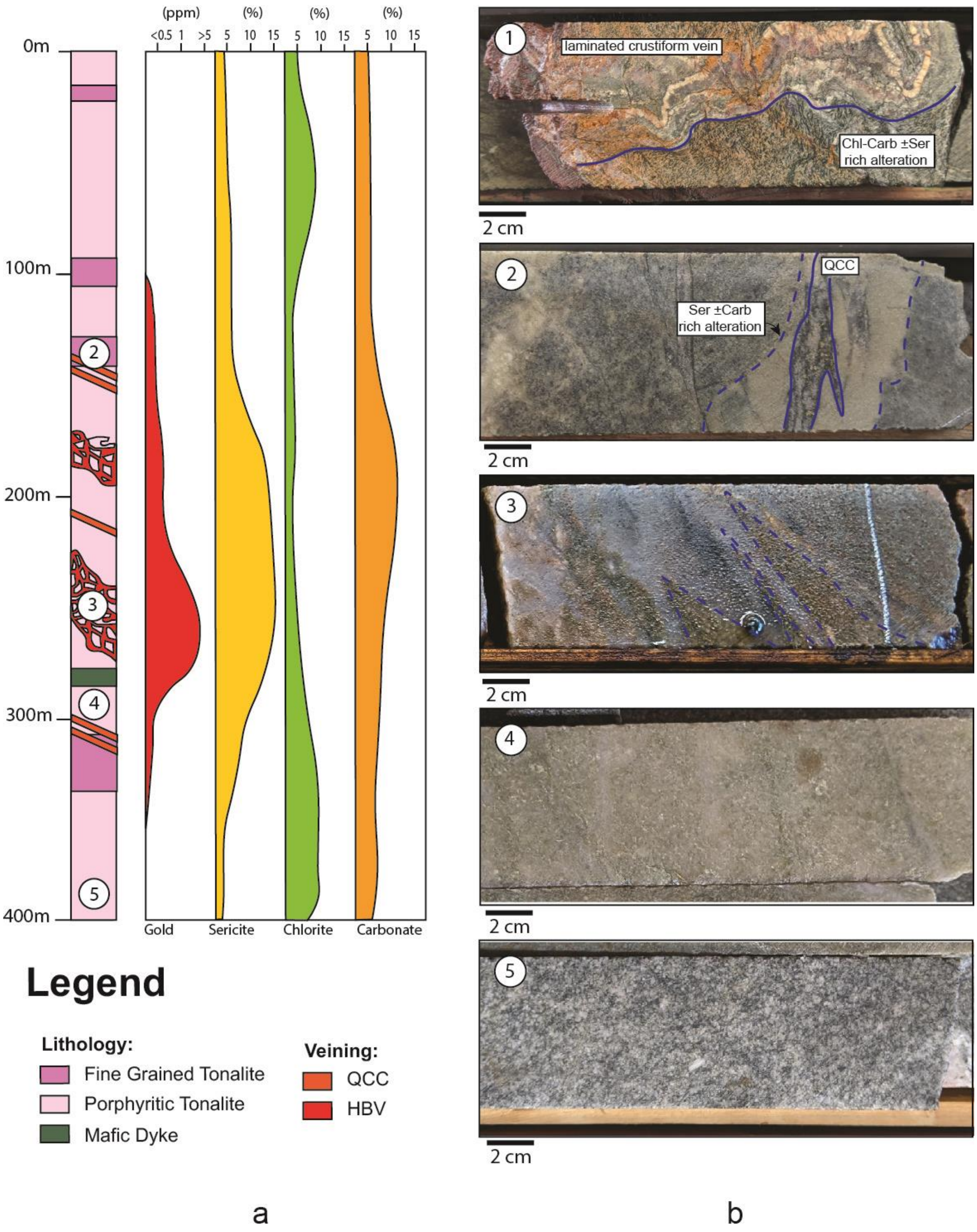

**Figure 14:** a) Graphic log of drill hole (BR-1060) b) 1. LCV with chlorite-carbonate alteration halo present in drill hole BR-4035, 2. QCC (solid blue line) with chlorite selvedges and sericite (±carbonate) alteration halo

(outlined by the blue broken lines) overprinting a chlorite-carbonate (±sericite) altered host rock, 3. HBV within a zone of bleaching. Fragments outlined by blue broken lines, 4. Sericite (±carbonate) altered porphyritic tonalite, 5. Chlorite-carbonate (±sericite)-altered porphyritic tonalite. Modal percentage of minerals are visual estimates. Gold concentrations are from Agnico Eagle Mines Ltd.

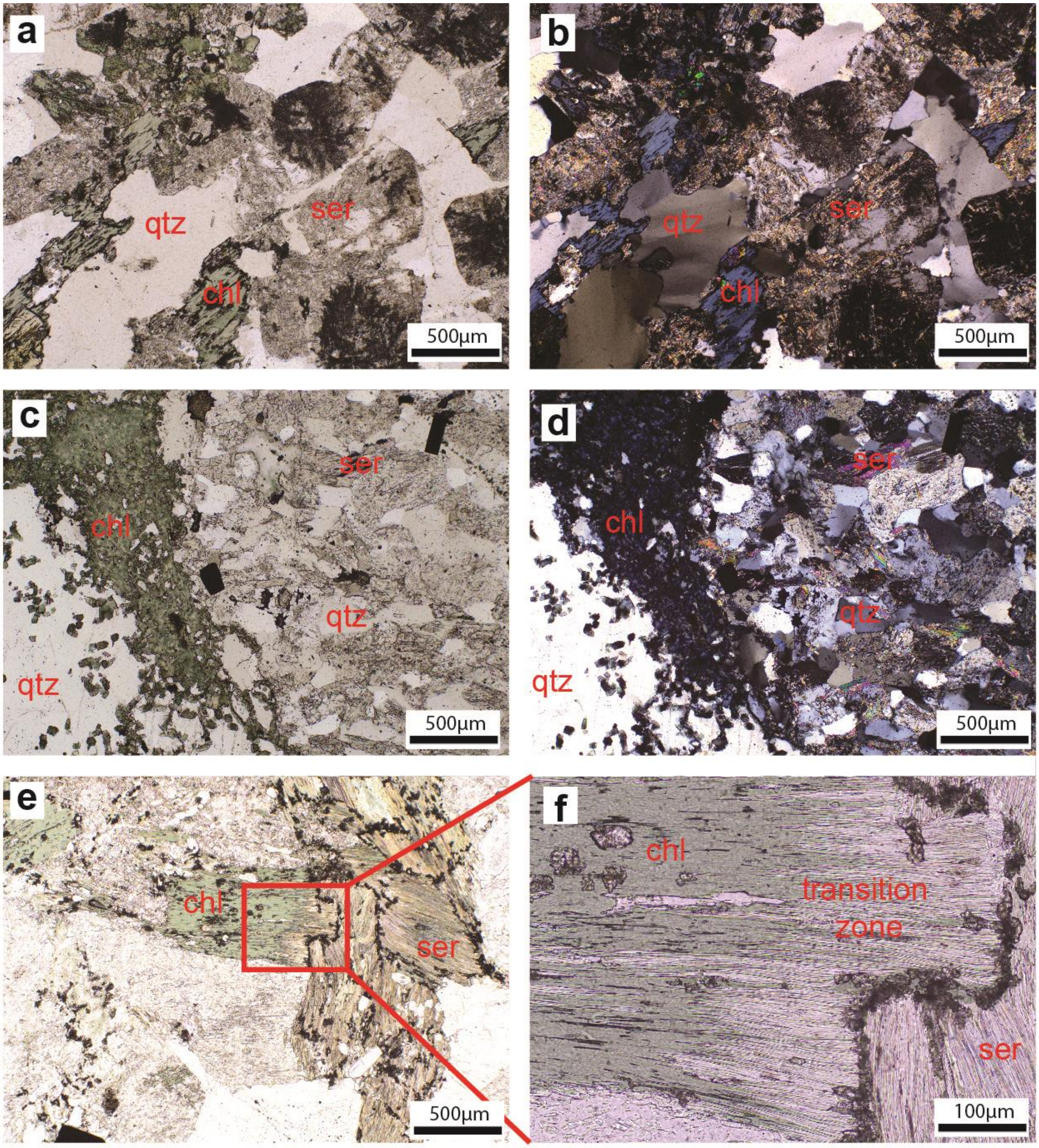

**Figure 15:** Photomicrographs of the early chlorite-carbonate (±sericite) and a late sericite (±carbonate) alteration (a) and (b) Plane polarized and cross polarized light microphotograph of porphyritic tonalite with early chlorite-carbonate (±sericite) alteration. (c) and (d) Plane polarized and cross polarized light microphotograph of a QCC vein with Fe-rich chlorite selvedges in contact with sericite altered porphyritic

tonalite. (e) Sericite replacing chlorite in alteration halo of a QCC vein. Plane polarized light. (f) Close-up of (e). Plane polarized light. QCC, quartz-chlorite-carbonate vein; chl, chlorite, qtz, quartz; ser, sericite.

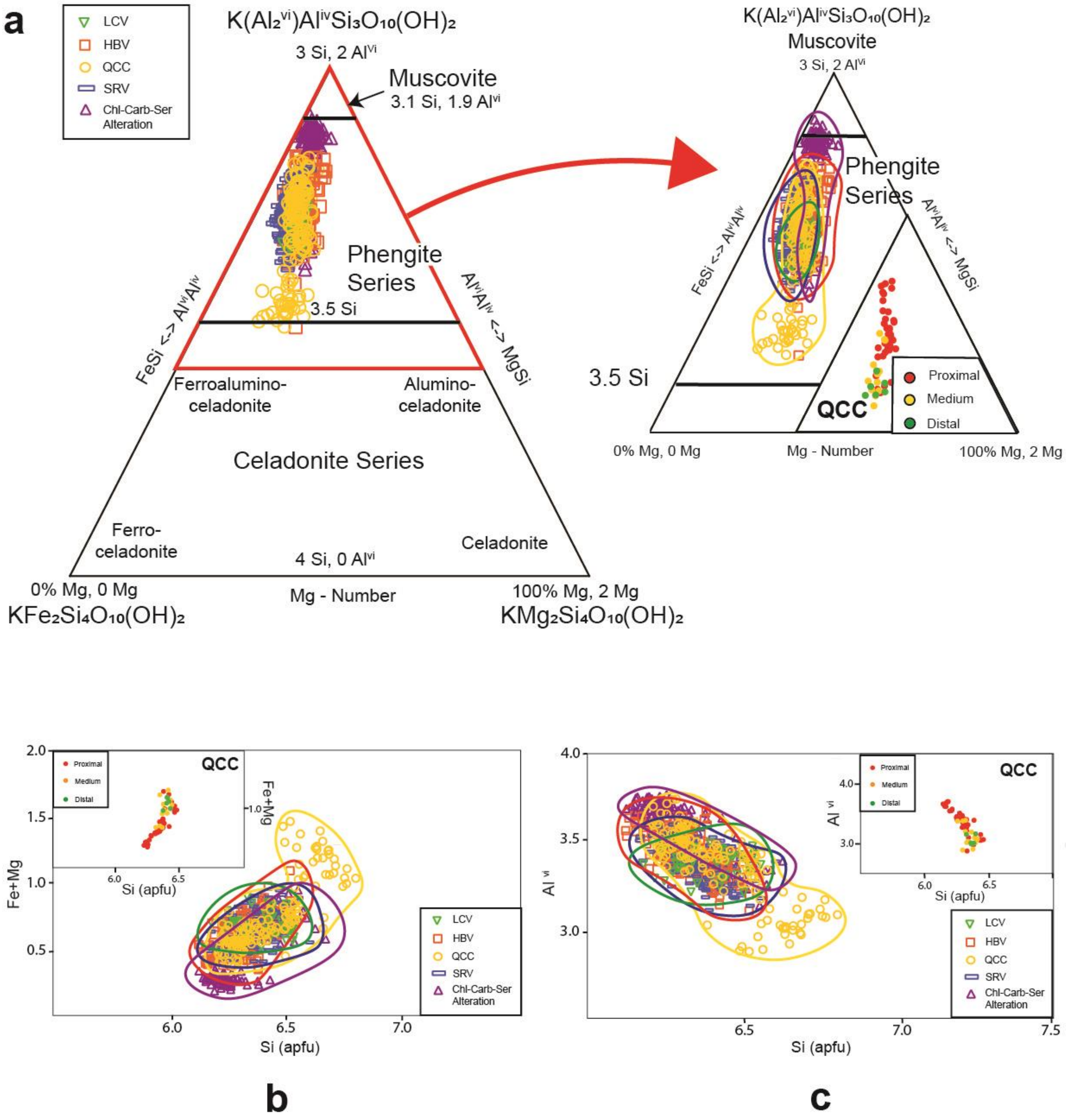

**Figure 16:** Sericite mineral chemistry showing trends in composition along different vein types found throughout the Hammond Reef deposit: a) Ternary diagram for potassic dioctahedral micas from the Hammond Reef deposit (after Tappert et al., 2013). $Al^{iv}$ cations apfu are plotted against Fe and Mg cations apfu calculated

using 11 O. b) Binary plot of Si cations apfu versus Fe+Mg cations apfu. and c) Binary plot of Si cations apfu versus $Al^{vi}$ cations apfu. LCV, laminated crustiform veins; HBV, hydrothermal breccia veins; QCC, quartz-chlorite-carbonate veins; SRV, sulfide-rich veins; Chl-carb-ser, wider zone of chlorite-carbonate-sericite alteration on outcrop #3. Inset plots of sericite chemistry proximal (red) to distal (green) from QCC veins.

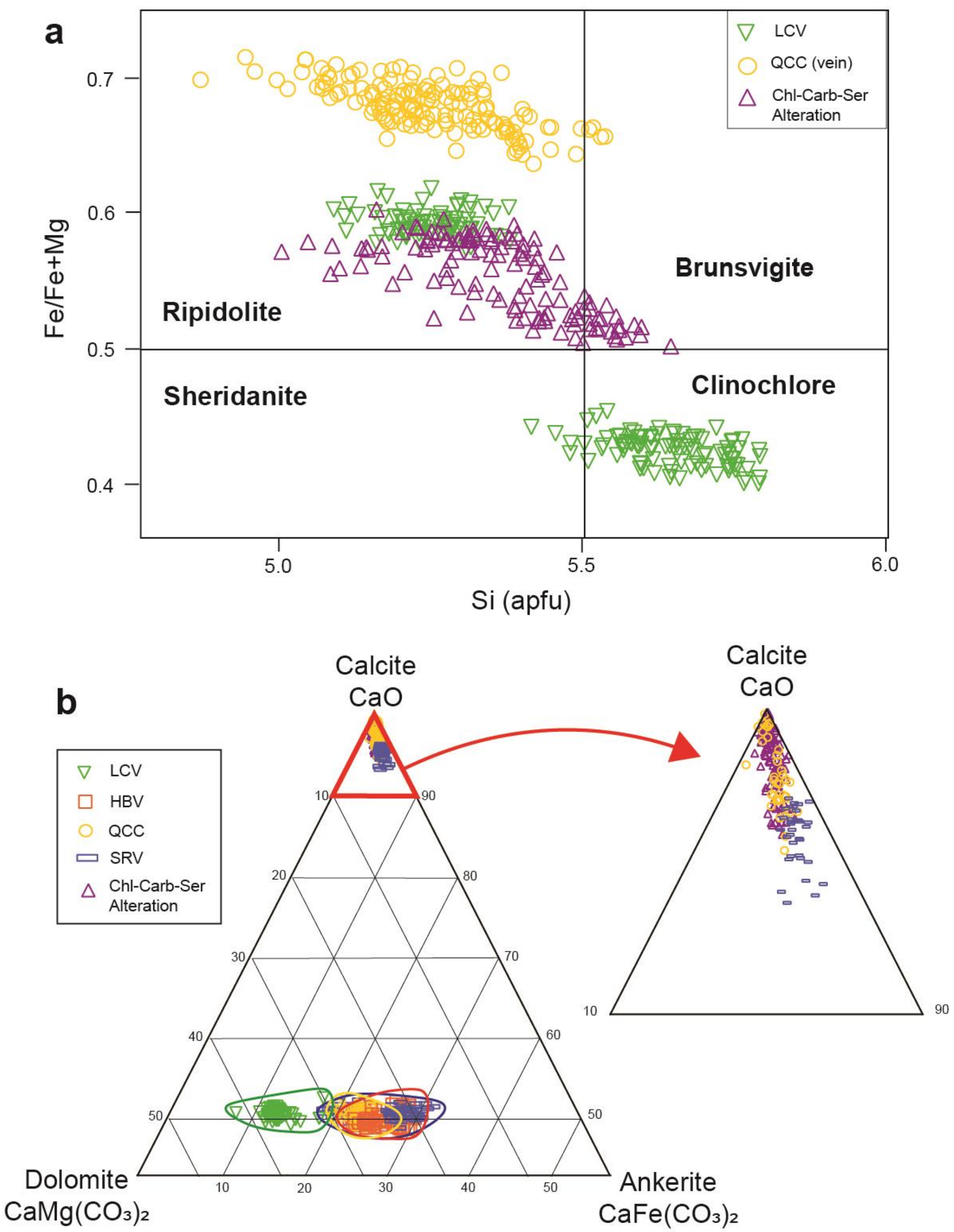

**Figure 17:** Chlorite and carbonate mineral chemistry showing variations in composition along vein types found throughout the Hammond Reef deposit; (a) Chlorite classification diagram after Foster (1962) calculated using 36 O. b) Ternary dolomite-ankerite-calcite diagram with Ca, Mg, Fe cations apfu calculated based on 6 O. LCV,

laminated crustiform veins; HBV, hydrothermal breccia veins; QCC, quartz-chlorite-carbonate veins; SRV, sulfide-rich veins; Chl-Ser-Carb, chlorite-carbonate-sericite alteration.

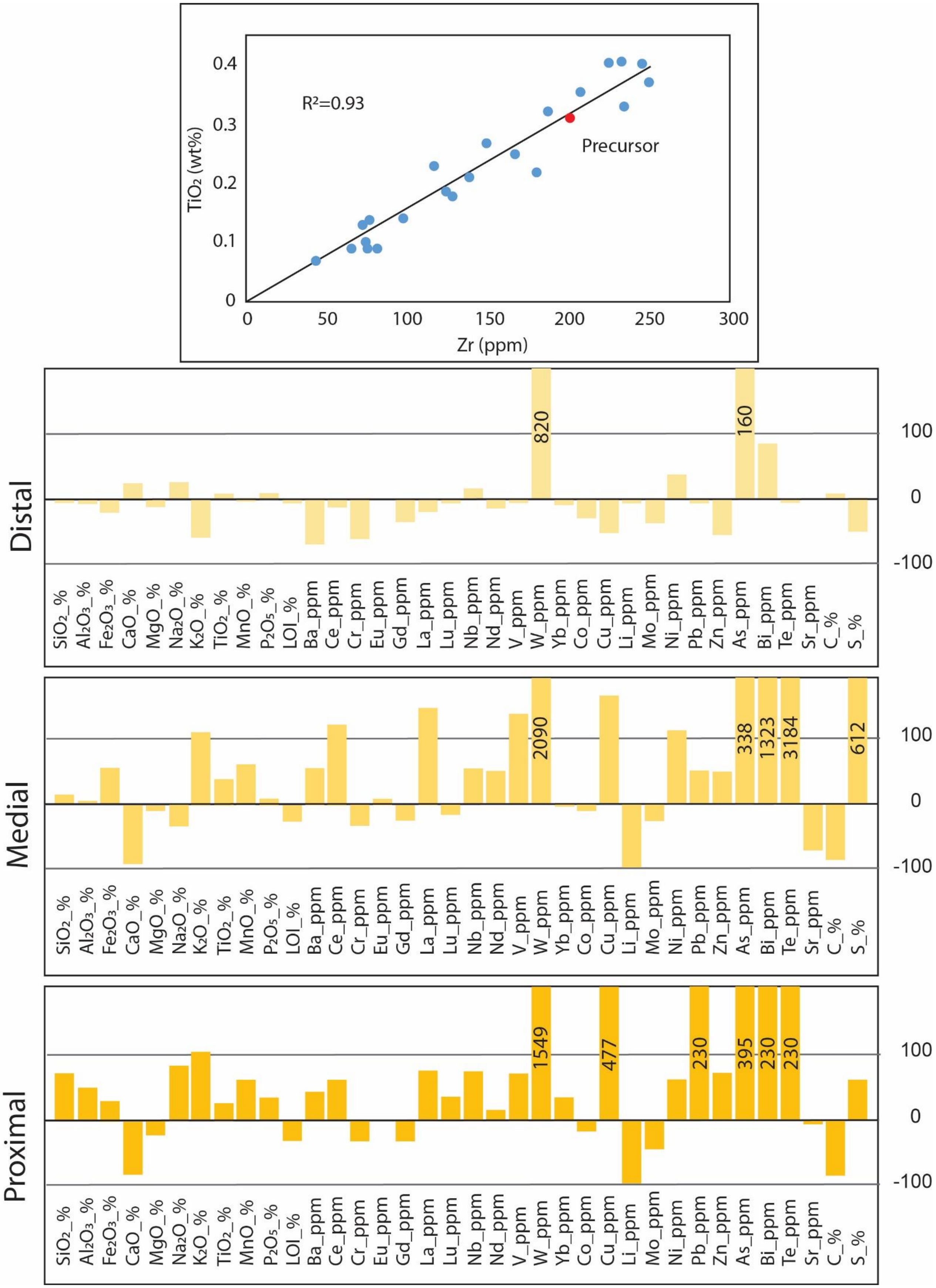
0.4
0.3
0.2
0.1
0
TiO₂ (wt%)
R²=0.93
Precursor
0
50
100
150
200
250
300
Zr (ppm)
Distal
Medial
Proximal
820
160
2090
338
1323
3184
612
1549
477
230
395
230
230
100
0
-100
SiO₂_%
Al₂O₃_%
Fe₂O₃_%
CaO_%
MgO_%
Na₂O_%
K₂O_%
TiO₂_%
MnO_%
P₂O₅_%
LOI_%
Ba_ppm
Ce_ppm
Cr_ppm
Eu_ppm
Gd_ppm
La_ppm
Lu_ppm
Nb_ppm
Nd_ppm
V_ppm
W_ppm
Yb_ppm
Co_ppm
Cu_ppm
Li_ppm
Mo_ppm
Ni_ppm
Pb_ppm
Zn_ppm
As_ppm
Bi_ppm
Te_ppm
Sr_ppm
C_%
S_%

**Figure 18**: Binary plot of $TiO_2$ versus Zr with an $R^2$ factor of 0.93 with the precursor sample shown by red solid circle. Mass balance diagrams in percent changes for distal (D835784), medial (D835783), and proximal (D835782) samples to shear zone on outcrop #3 shown on Figure 8.

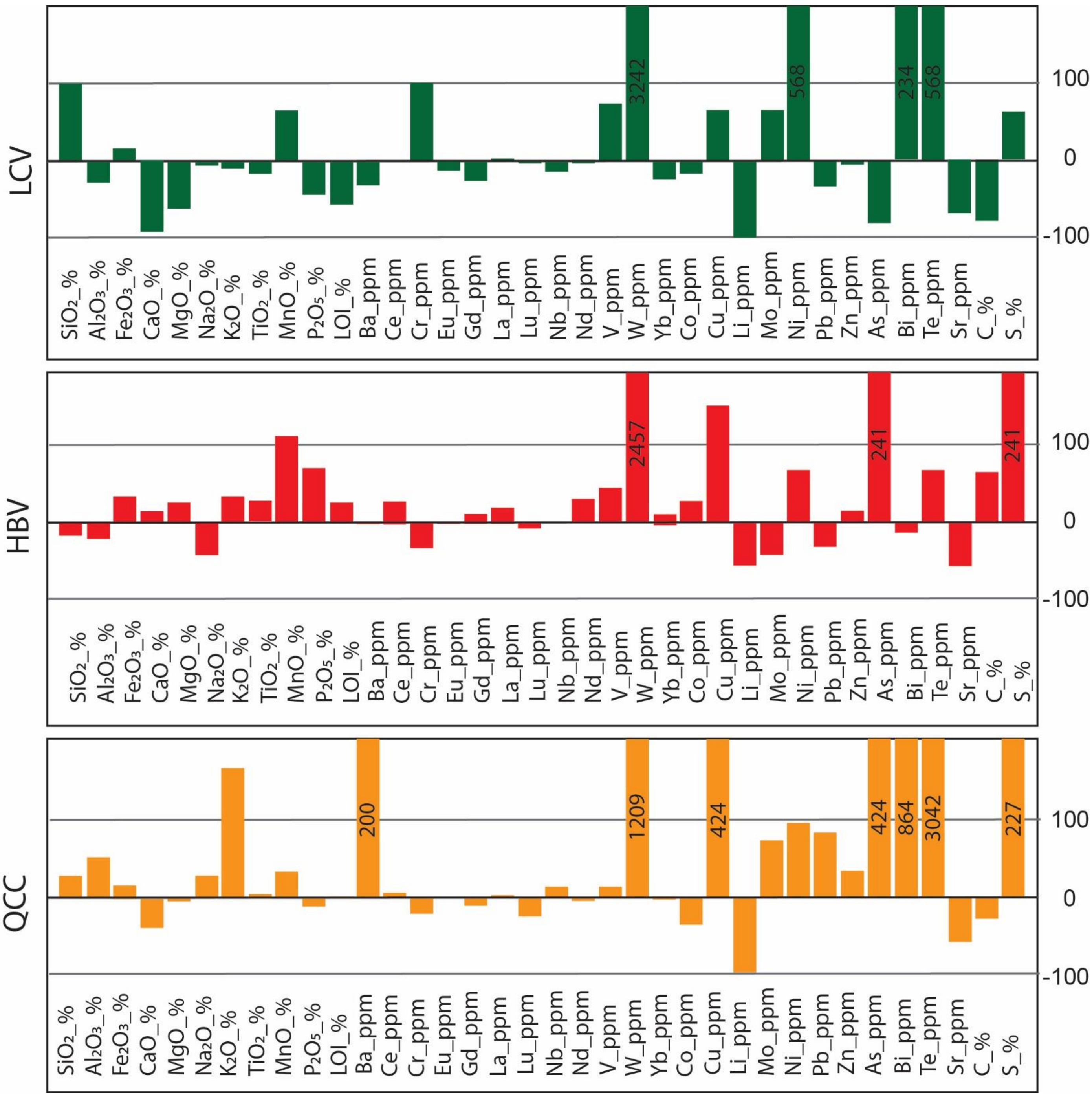

**Figure 19:** Mass balance diagrams in percent changes for alteration halos associated with LCV, laminated crustiform veins; HBV, hydrothermal breccia veins; QCC, quartz chlorite carbonate veins.

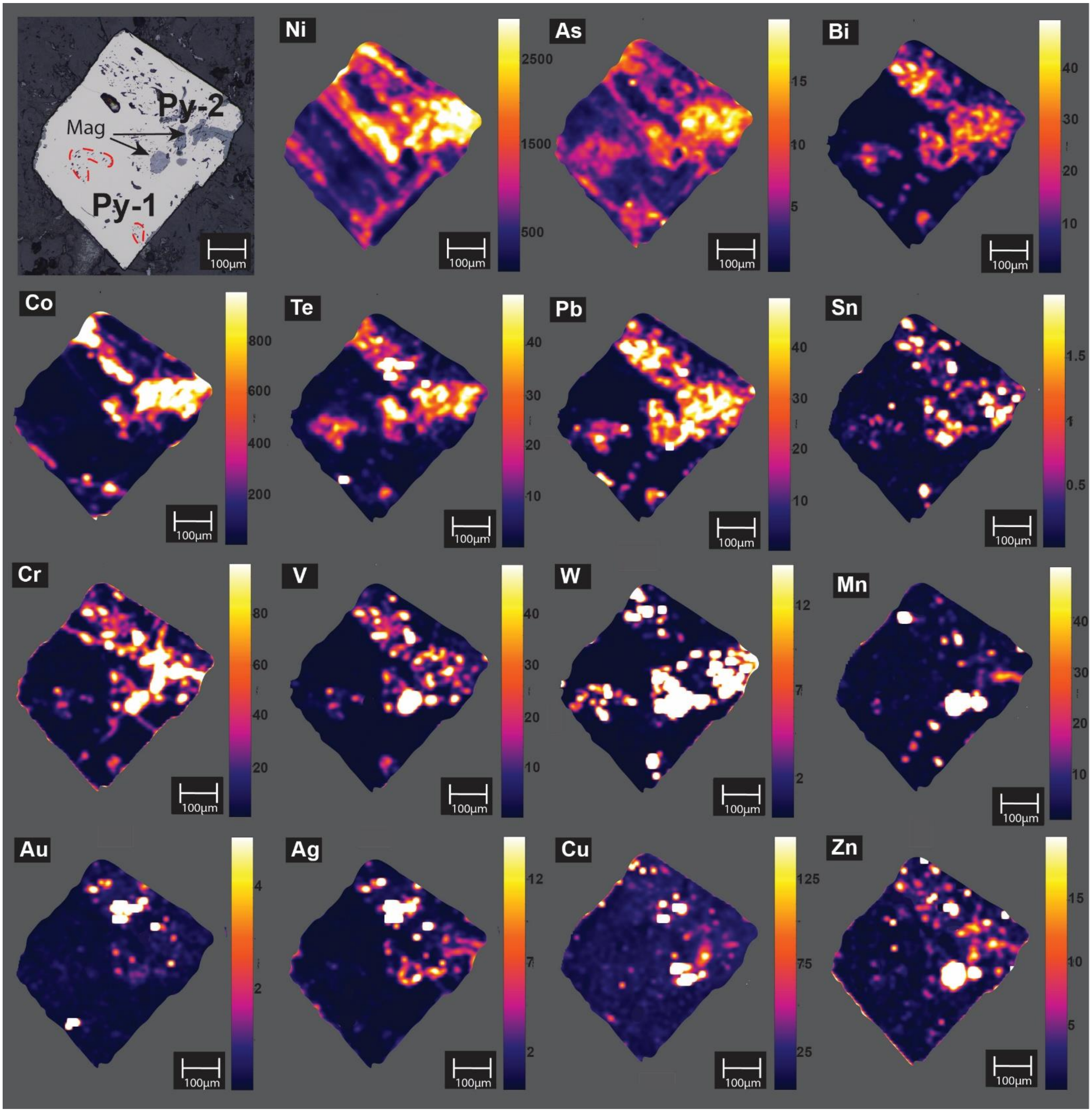

**Figure 20:** LA-ICP-MS element maps showing two generation of pyrite growth of a pyrite grain located in the alteration halo of an LCV.

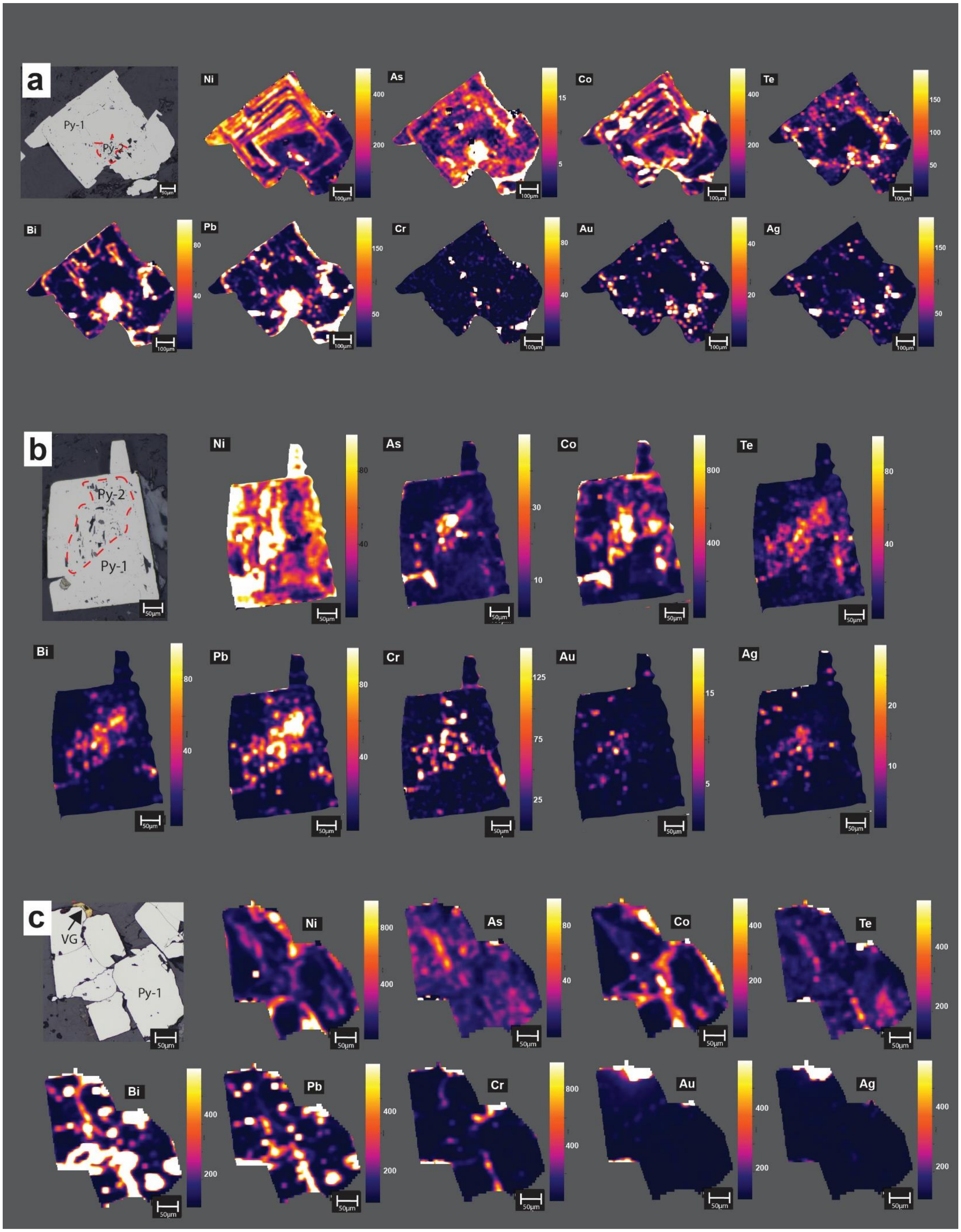

**Figure 21:** LA-ICP-MS element maps showing multiple generation of pyrite growth in pyrite grains associated with; a) HBV, b) QCC vein, and c) SRV.

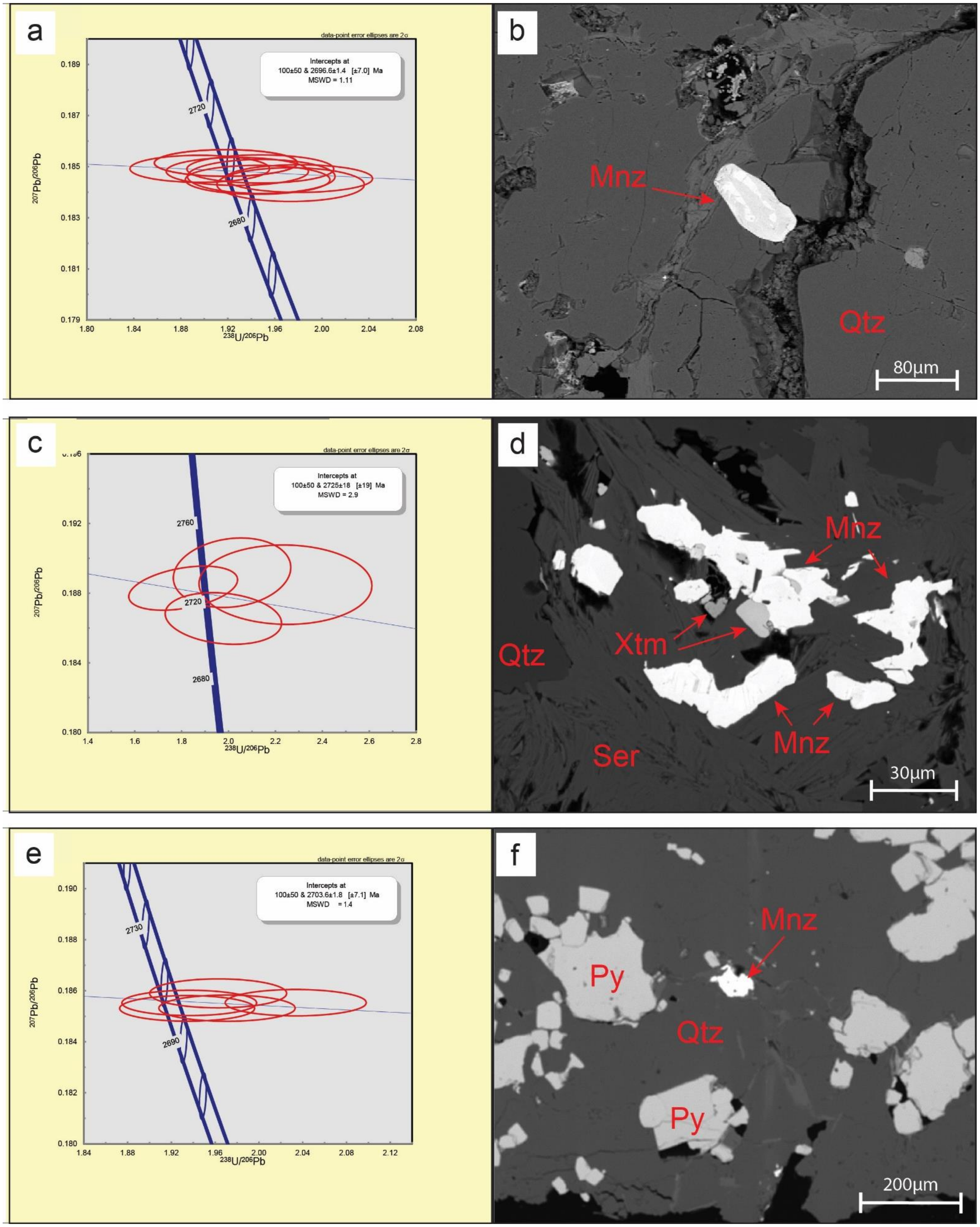
a
data-point error ellipses are 2σ
Intercepts at
100±50 & 2696.6±1.4 [±7.0] Ma
MSWD = 1.11
0.189
0.187
0.185
0.183
0.181
0.179
2720
2680
1.80
1.84
1.88
1.92
1.96
2.00
2.04
2.08
$^{238}U/^{206}Pb$
$^{207}Pb/^{206}Pb$
b
Mnz
Qtz
80µm
c
data-point error ellipses are 2σ
Intercepts at
100±50 & 2725±18 [±19] Ma
MSWD = 2.9
0.196
0.192
0.188
0.184
0.180
2760
2720
2680
1.4
1.6
1.8
2.0
2.2
2.4
2.6
2.8
$^{238}U/^{206}Pb$
$^{207}Pb/^{206}Pb$
d
Mnz
Xtm
Qtz
Ser
Mnz
30µm
e
data-point error ellipses are 2σ
Intercepts at
100±50 & 2703.6±1.8 [±7.1] Ma
MSWD = 1.4
0.190
0.188
0.186
0.184
0.182
0.180
2730
2690
1.84
1.88
1.92
1.96
2.00
2.04
2.08
2.12
$^{238}U/^{206}Pb$
$^{207}Pb/^{206}Pb$
f
Mnz
Py
Qtz
Py
200µm

**Figure 22:** In situ U-Pb monazite age of mineralization. a) Concordia diagram for monazite from the LCV, b) SEM backscattered image of analyzed monazite grain in LCV, c) Concordia diagram for monazite from the HBV, d) SEM backscatter image of analyzed monazite in alteration halo of HBV, e) Concordia diagram for monazite from the SRV, b) SEM backscatter image of analyzed monazite in SRV.

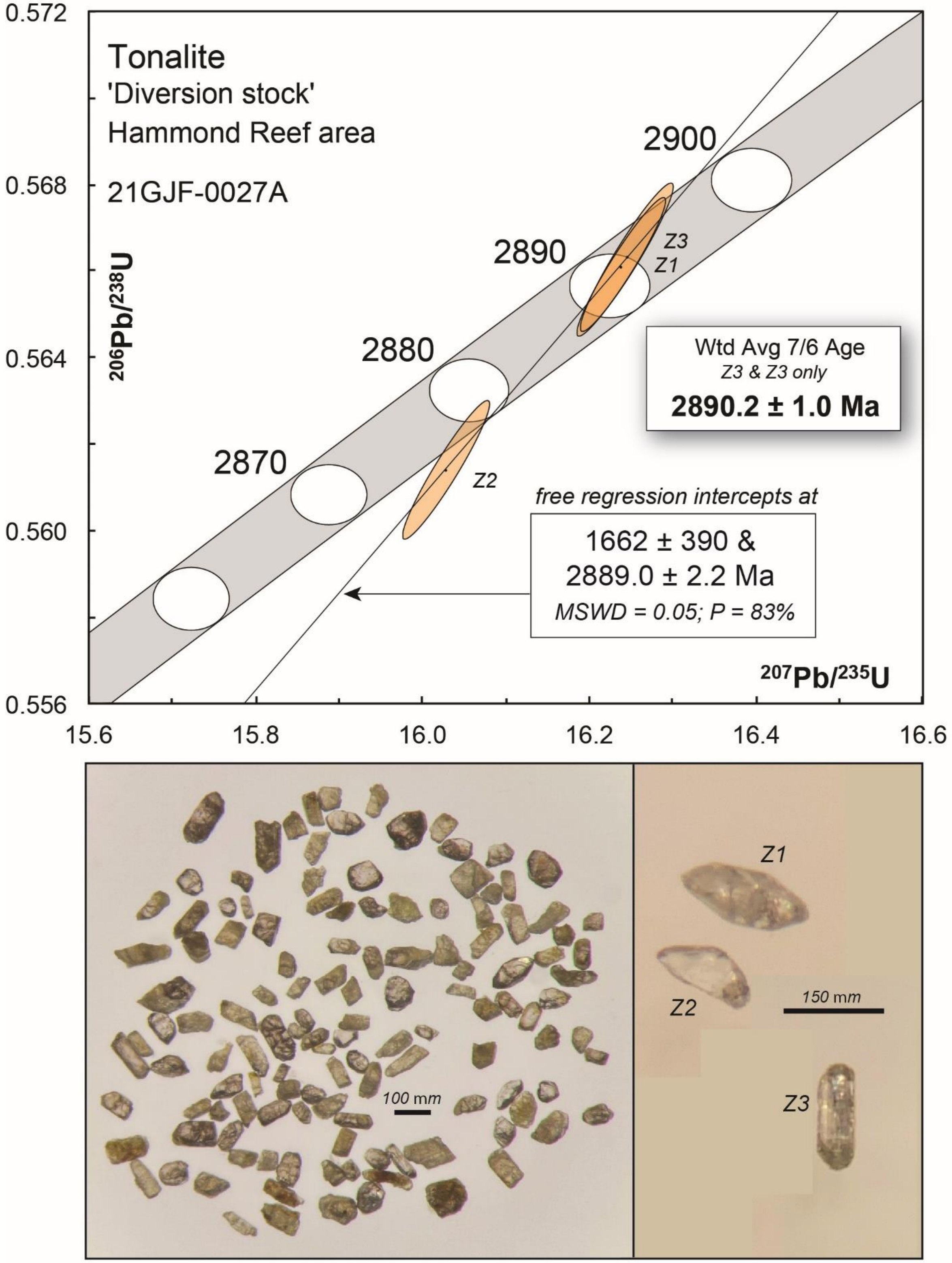

**Figure 23:** Concordia diagram and associated images of analyzed zircons from sample MEAK21GJF0027A of the Diversion stock tonalite.

# Appendices

## Appendix A: Methodology

### *Field mapping*

Field work was done over two summers (2020-21). Regional mapping at a scale of 1:2500 was conducted along the MSS to measure and record the orientation and style of structures along this shear system. More detailed 1:100 scale mapping was done on mechanically stripped outcrops of the Hammond Reef deposit to better understand the controls on mineralization. Graphic logging of ten drill holes equally distributed along two north-south oriented fences was done to better constraint the relative timing of veins and breccias, and characterize the variations in sericite, chlorite, carbonate, and hematite alteration intensity across the deposit.

### *Whole rock geochemistry and assay analysis*

Fifty-five samples from the Marmion Batholith and Diversion stock tonalites were sent for whole rock geochemistry and assay analysis. The samples were prepared at the ALS Laboratory in Sudbury, ON., and analyzed for major and trace elements at the ALS Laboratory in Vancouver, BC. To ensure satisfactory accuracy and precision, standards (ORCA-1 and NP-1-427) followed by a blank were used every twenty samples.

Weathered and altered surfaces were removed, samples were then washed, dried, and crushed to <2 mm. An aliquot of the sample (250g) was pulverized to <75 microns. The crusher and pulverizing discs were cleaned after every sample to avoid contamination. Major elements were digested using metaborate fusion and analyzed by inductive coupled plasma emission spectrometry (ICP). Trace elements (Ba, Ce, Cr, Cs, Dy, Er, Eu, Ga, Gd, Hf, Ho, La, Lu, Nb, Nd, Pr, Rb, Sm, Sn, Sr, Ta, Tb, Th, Tm U, V, W, Y, Yb, Zr) were digested using metaborate fusion and analyzed by inductive coupled plasma emission mass spectrometry (ICP-MS). Precision and accuracy were better than 10%, for major elements, REE's, and other trace metals except for analyses close to detection limits. Base metals Cd, Co, Cu, Mo, Ni, Pb, Sc, Zn, Ag, and Li were analyzed using four acid digestion ICP. Trace elements (As, Bi, Hg, In, Re, Sb, Se, Te, and Tl) were analyzed using the aqua regia digestion coupled with ICP-MS. Concentration of S and C were analyzed by combustion using a Leco™ induction furnace. Concentration of $H_2O$ were analyzed by combustion using absorption of inferred energy with a precision better than 5%. Concentration of Cl and F were analyzed using potassium hydroxide fusion and ion chromatography with a precision better than 6%.

The samples were further assayed for their Au and Ag content. They underwent four acid digestion, and aliquot of these solutions were analyzed for Ag by atomic absorption spectroscopy (AAS), Au was analyzed by fire assay with an ICP instrumental finish.

### *Trace elemental mapping*

Trace element mapping analyses were conducted at the Mineral Exploration Research Centre isotope Geochemistry Lab (MERC-IGL), at Laurentian University. Laser ablation sampling was performed using a Photon Machines Analyte G2 ArF excimer laser, with 193 nm wavelength, <5 ns pulse width, and HelEx II cell. Laterally contiguous line traverses were ablated with laser fluence of 4 J/cm 2, 30 Hz repetition rate, and 5-10 µm spot size. Depending on grain size scan speeds between 15 µm/s were used for each map. Sixty seconds of background were measured at the beginning and end of the analytical session, with 10 seconds of background measured between each line. Helium carrier gas flows through the ablation cell was 0.525 l/min (cup) and 0.1 l/min (cell), with 0.625 l/min Ar and 6 ml/min $N_2$ makeup gas added downstream of the cell. The reference glasses NIST-610 and GSE were analyzed two times at the beginning and end of the session, and periodically throughout the session.

Trace element measurements were conducted using a Thermo Scientific iCap-TQ ICP-MS in single quad mode to ensure maximum sensitivity on the low to intermediate mass range. Cool gas, auxiliary gas, and RF power were set at 14 L/min, 0.8 L/min, and 1550 W, respectively. The raw trace element signal intensity data were processed using Iolite v4, with baseline subtraction, instrumental drift correction, and concentration normalization performed with the Trace Element – Internal Standard reduction scheme (Paton et al., 2011; Petrus and Kamber, 2012). Typically, one second at the beginning and end of each line traverse were excluded from the selections in order to minimize potential fractionation effects. Trace element data were normalized to the pressed powder FeS1 RM. An assumed stoichiometric concentration of 46.5 wt% Fe was used for all pyrite, to account for differing ablation characteristics between the glass and pyrite.

### *In-situ monazite U-Th-Pb isotopic geochronology*

U-Th-Pb isotope analyses were conducted at the Mineral Exploration Research Centre - Isotope Geochemistry Lab (MERC-IGL) at Laurentian University. Laser ablation sampling was performed using a Photon Machines Analyte G2 ArF excimer laser, with 193 nm wavelength, <5 ns pulse width, and HelEx II cell. Helium carrier gas flows through the ablation cell were for 0.6 l/min (cup) and 0.1 l/min (cell), with 0.725 l/min Ar and 8 ml/min $N_2$ makeup gas added downstream of the cell. A laser fluence of 2 J/cm$^2$ and spot diameter of 10-20 μm and were used for monazite, depending on grain/domain size. Ablation durations were 30 seconds at a 7 Hz repetition rate, leaving estimated ablation pit depths of 10-15 μm. Sixty seconds of background were measured at the beginning and end of the analytical session, with 30 seconds of background measured between each ablation.

U-Th-Pb isotope measurements were conducted using a Thermo Scientific Neptune Plus multicollector (MC) ICP-MS, equipped with Jet interface and nine Faraday cups. Analyses were conducted in low resolution, static mode to ensure maximum sensitivity and stability. The ~15% Faraday cup mass range allows isotopes between $^{204}$Hg/Pb to $^{238}$U to be measured simultaneously, with the cup configuration and fictive mass of ~220.65 aligned with the center cup. All cups were coupled with $10^{11}$ Ω amplifiers, with the exception of L2, which was coupled with $10^{12}$ Ω amplifier for better precision on the low intensity $^{207}$Pb signal. Ion beam drift from day to day was typically <0.03 amu, with flat top peak width typically ~0.2 amu, ensuring stable on-peak measurements throughout long-duration analytical sessions. Cool gas flows and RF power were set at 16 L/min and 1200 W, with Ar auxiliary gas flows of 0.85 L/min. During tuning on NIST612 synthetic glass prior to analysis the mean uranium oxide percent (($^{254}$UO/$^{238}$U)*100) was 0.35% (always <0.37%).

The raw U-Th-Pb data were processed in Iolite v4, with baseline subtraction, instrumental drift, and downhole fractionation corrections performed with the U-Pb geochronology data reduction scheme (DRS; Petrus and Kamber, 2012). The reference materials (RMs) used to normalize U-Th-Pb isotope ratios and model downhole fractionation (primary RMs), and evaluate data accuracy (verification RMs) are listed in Table A1. The primary RM, monazite KM03 (MacLachlan et al., 2004) were analyzed three times at the beginning and end of each session, and once every five-ten unknowns throughout the session (depending on the length of session). Typically, 3 seconds at the beginning and 1 second at end of the ablation period were excluded from the selections in order to minimize potential fractionation effects, leaving ~26 seconds of signal for integration. Ablation signals were inspected visually, with integration periods refined to exclude portions of the analyses with high $^{204}$Pb or irregular $^{207}$Pb/$^{206}$Pb age spectra. Within run variance in the measured ratios for primary RMs (i.e. the additional percent error required to achieve MSWD = 1) was propagated into the 2SE uncertainty for all unknowns. No additional uncertainty propagation was applied to the $^{207}$Pb/$^{206}$Pb ratios of unknown analyses, due to the long-term variance of $^{207}$Pb/$^{206}$Pb ratios of verification RMs in the MERC-IGL having MSWD < 1 (e.g. Horstwood et al., 2016). Three verification RMs were analyzed during the session to ensure accuracy of the U-Pb ratios. Each RM yielded accurate $^{207}$Pb/$^{206}$Pb weighted mean ages (overlapping their accepted TIMS ages) with uncertainty between 1-2 Ma and low MSWD.

**Table A2:** Supplementary information referring to analytical data collected in-situ monazite U-Th-Pb isotopic geochronology.

| **Laboratory & Sample Preparation** | |
|---|---|
| Laboratory name | MERC IGL |
| Sample type/mineral | Monazite |
| Analysis | U-Pb |
| Sample preparation | Thin Section |
| Reference material location | Separate mount |
| Imaging | BSE |
| | |
| **Laser ablation system** | |
| Make, Model & type | Photon Machines, Analyte G2 |
| Ablation cell & volume | Helex II, large format, two volume |
| Laser wavelength (nm) | 193 |
| Pulse width (ns) | <4 |
| Fluence (J.cm-2) | 2 |
| Repetition rate (Hz) | 7 |
| Ablation duration (secs) | 30 |
| Ablation pit depth / ablation rate | ~15 um/ ~0.5 um/sec |
| Spot size (um) | 10-20 |
| Sampling mode / pattern | spot |
| Carrier gas | He & Ar (after cell) & N2 (after cell) |
| Cell carrier gas flow (l/min) | He1 (cup) = 0.6, He2 (cell) = 0.10, Ar = 0.725, N2 = 0.008 |

**Table A1**: continued.

| **ICP-MS Instrument** | |
|---|---|
| Make, Model & type | Thermo Neptune Plus with Jet Interface |
| Sample introduction | Laser Ablation |
| RF power (W) | 1200 |
| Make-up gas flow (l/min) | 0.07 |
| Detection system | 9 Faraday Cups |
| Masses measured | 204, 206, 207, 208, 232, 238 |
| Integration time per peak/dwell times (ms) | NA |
| Total integration time per output datapoint (secs) | 0.25 |
| 'Sensitivity' as useful yield (%, element) | |
| IC Dead time (ns) | NA |
| | |
| **Data Processing** | |
| Gas blank | Measured for 90 sec at beginning and end of run & 30 sec between ablations |
| Calibration strategy | Standard Sample bracketing |
| Reference Material info | Primary RM = KM-03 (Mnz; 1822 ± 2 Ma; MacLachlan et al., 2004), Secondary RMs = DD90-26A (Mnz; 2671 ± 1.2 Ma; Davis (1991)); XTC (Xtm; 2632 ± 1.3 Ma; McNaughton et al., 1999); z6413 (Xtm; 997 ± 0.8 Ma; Stern & Rayner (2003) |
| Data processing package used / Correction for LIEF | Iolite v. 4; DRS = U-Pb Geochron |
| Mass discrimination | |
| Common-Pb correction, composition, and uncertainty | NA |
| Uncertainty level & propagation | Spots = 2SE, Wtd. Means = 2 SD with propagation of in-run variance in primary RM |
| Quality control / Validation | DD90-26A = 2669.9 ± 1.0 Ma (MSWD = 1.03; n=12); XTC = 2633.3 ± 2.0 Ma (MSWD = 2.1; n=10); z6413 = 995.7 ± 1.3 Ma (MSWD = 0.98; n=12/12) (207Pb/206Pb Wtd. Means) |

### *TIMS*

Rocks were crushed using a jaw crusher and then underwent grinding using a disk mill. Initial separation of heavy minerals was carried out by passing the heavy concentrate over a shaking, riffled water (Wilfley$^{TM}$) table multiple times. Further processing employed density separations with methylene iodide and paramagnetic separations with a Frantz isodynamic separator. Final sample selection was achieved by hand picking in alcohol under a binocular microscope, choosing the freshest, least cracked, core-and inclusion-free grains of zircon.

Analytical methods involved isotope dilution thermal ionization mass spectrometry (ID-TIMS) following chemical abrasion (chemical abrasion, modified after Mattinson, 2005). Zircon grains that underwent chemical abrasion treatment were annealed in quartz crucibles at 900°C for 2 days. This removes much, although not all, of the radiation damage induced by decay of U and Th contained in the mineral, rendering least altered zircon more inert to chemical attack. The annealed grains were subsequently leached in approximately 0.10 ml of concentrated hydrofluoric (HF) acid for several hours in teflon vessels at 200°C. Altered parts of the crystals, which contain isotopically disturbed Pb, dissolve more rapidly than annealed, unaltered crystal domains for low to moderate levels of radiation damage. Attack is variable, depending on the uranium concentration of the grains and the consequent degree of radiation damage. Chemical abrasion has the advantage of penetrative removal of alteration domains where Pb-loss has occurred, and generally improves concordance.

Weights of mineral fractions chosen for ID-TIMS analysis were estimated from scaled digital photomicrographs, using the density of zircon. Estimated weights should be accurate to about ±20%. This affects only U and Pb concentrations, not age information, which depends only on isotope ratio measurements. Samples were washed briefly in 7N $HNO_3$ prior to dissolution. A mixed $^{205}$Pb-$^{235}$U isotopic spike was added to the dissolution capsules during sample loading. Zircon grains were dissolved using concentrated HF in Teflon bombs at 200°C for 3-4 days, then dried and re-dissolved in 3N HCl overnight to ensure complete dissolution and equilibration with the spike (Krogh, 1973). U and Pb were isolated using 50 microliter anion exchange columns using

HCl elutions, dried down, and then loaded onto outgassed rhenium filaments with silica gel (Gerstenberger and Haase, 1997).

Pb and $UO_2$ were analyzed on a VG354 mass spectrometer using a Daly collector in pulse counting mode. The mass discrimination correction for this detector was constant at 0.07%/AMU. Thermal mass discrimination corrections are 0.10%/AMU for Pb and U. Dead time of the Daly system was 16 ns for Pb during the analytical period, monitored using the SRM982 Pb standard. Mass spectrometer data was reduced using in-house software (UtilAge program) coded by D. Davis. All common Pb was assigned to procedural blank. Initial Pb from geological sources above 1 picogram was corrected using the Pb evolution model of Stacey and Kramers (1975). Plotting of Concordia curves and averaging of age results were carried out using the Isoplot 3.71 Add-In for MS Excel, of Ludwig (2009). The date determined by weighted average (i.e., for fractions Z1 & Z3) uses the algorithm of Ludwig (2009) utilizing the internal errors only; the age calculated based on a linear regression of all 3 fractions (Z1-Z3) uses a modified version of the York (1969) algorithm, in which points are weighted proportional to the inverse of the square of the assigned errors, incorporating error correlations (see Ludwig, 2009); uncertainties in the U decay constants are not considered. Probabilities of fit would be expected to be 50% on average for random data with correctly chosen analytical errors. All age errors and error ellipses are given at the 2 sigma or 95% level of confidence. Total common Pb levels in the analyzed zircons range from only 0.2–0.4 pg and is assigned entirely to the laboratory blank.

## Appendix B: Sample description

**Table B3:** Sample localities, analysis, descriptions, and other associated data.

| Sample ID | Easting | Northing | Analysis | Assay tag | Sample description | Lithology description |
|---|---|---|---|---|---|---|
| MEAK20GJF0001AG03 | 611959 | 5420959 | Polished thin section | - | BR-1060 (135.35-135.65m) | Weak chlorite-carbonate (±sericite) altered porphyritic tonalite |
| MEAK20GJF0001AG07 | 611959 | 5420959 | Polished thin section | - | BR-1060 (242.9-243.2m) | Strong sericite (±carbonate) altered fine grained tonalite |
| MEAK20GJF0001AG08 | 611959 | 5420959 | Polished thin section | - | BR-1060 (250.9-251.2m) | 9 cm wide QCC with 3 cm wide sericite (±carbonate) alteration halo hosted in porphyritic tonalite |
| MEAK20GJF0001AG09 | 611959 | 5420959 | Polished thin section | - | BR-1060 (252.6-252.9m) | Strong sericite (±carbonate) altered fine grained tonalite |
| MEAK20GJF0001AG10 | 611959 | 5420959 | Polished thin section | - | BR-1060 (255-255.3m) | 1 cm wide HBV hosted in strong sericite (±carbonate) altered porphyritic tonalite |
| MEAK20GJF0001AG12 | 611959 | 5420959 | Polished thin section | - | BR-1060 (256.5-256.8m) | Strong sericite (±carbonate) altered porphyritic tonalite |
| MEAK20GJF0001AG15 | 611959 | 5420959 | Polished thin section | - | BR-1060 (270-270.3m) | 1 cm wide QCC with 0.5 cm wide sericite (±carbonate) alteration halo hosted in porphyritic tonalite |
| MEAK20GJF0001AG17 | 611959 | 5420959 | Polished thin section | - | BR-1060 (284.85-285.17m) | Strong hematite and magnetite altered porphyritic tonalite |
| MEAK20GJF0002AG01 | 611909 | 5421052 | Polished thin section | - | BR-1035 (79.65-79.95m) | Weak chlorite-carbonate (±sericite) altered fine grained tonalite |
| MEAK20GJF0002AG04 | 611909 | 5421052 | Polished thin section | - | BR-1035 (169.65-169.95m) | 2 cm wide LCV with a 1 cm wide chlorite-carbonate (±sericite) alteration halo hosted in fine grained tonalite |
| MEAK20GJF0002AG07 | 611909 | 5421052 | Polished thin section | - | BR-1035 (226.2-226.5m) | Strong sericite (±carbonate) altered and sheared porphyritic tonalite |
| MEAK20GJF0002AG08 | 611909 | 5421052 | Polished thin section | - | BR-1035 (234.25-234.55m) | 5-7 cm wide QCC with a 3 cm wide sericite (±carbonate) alteration halo hosted in porphyritic tonalite |
| MEAK20GJF0002AG09 | 611909 | 5421052 | Polished thin section | - | BR-1035 (235.95-236.25m) | Strong sericite-hematite (±carbonate) altered porphyritic tonalite |
| MEAK20GJF0002AG10 | 611909 | 5421052 | Polished thin section | - | BR-1035 (270.95-271.25m) | Strong sericite (±carbonate) altered and sheared porphyritic tonalite |

**Table B2:** Continued.

| Sample ID | Easting | Northing | Analysis | Assay tag | Sample description | Lithology description |
|---|---|---|---|---|---|---|
| MEAK20GJF0003AG01 | 612051 | 5420832 | Polished thin section | - | BR-1200 (116.25-116.55m) | Strong sericite (±carbonate) altered porphyritic tonalite |
| MEAK20GJF0003AG02 | 612051 | 5420832 | Polished thin section | - | BR-1200 (267.25-267.57m) | Strong sericite (±carbonate) altered and sheared fine grained tonalite |
| MEAK20GJF0003AG03 | 612051 | 5420832 | Polished thin section | - | BR-1200 (416.35-416.65m) | Weak chlorite-carbonate (±sericite) altered porphyritic tonalite |
| MEAK20GJF004AG02 | 611720 | 5421329 | Polished thin section | - | BR-1136 (20.6-20.9m) | 1 cm wide HBV hosted in strong sericite (±carbonate) altered porphyritic tonalite |
| MEAK20GJF0005AG02 | 611874 | 5421103 | Polished thin section | - | BR-1042 (163.8-164.1m) | Strong sericite (±carbonate) altered porphyritic tonalite |
| MEAK20GFJ0006AG02 | 615315 | 5422364 | Polished thin section | - | Outcrop #1 | 10 cm wide SRV with a 2 cm wide sericite (±carbonate) alteration halo hosted in gneissic tonalite |
| MEAK20GFJ0006AG03 | 615322 | 5422354 | Polished thin section | - | Outcrop #1 | 1-5 cm wide extensional veins hosted in gneissic tonalite |
| MEAK20GJF0007AG01 | 613696 | 5422267 | Polished thin section | - | Outcrop #2 | 10-15 cm wide breccia vein with a 3-5 cm wide sericite (±carbonate) alteration halo hosted in porphyritic tonalite |
| MEAK20GJF0007AG02 | 613692 | 5422252 | Polished thin section | - | Outcrop #2 | 5-10 cm wide LCV with a 5 cm wide chlorite-carbonate alteration halo hosted in porphyritic tonalite |
| MEAK20GJF0007AG03 | 613694 | 5422283 | Polished thin section | - | Outcrop #2 | 1-5 cm wide SRV vein with 1-2 cm wide sericite (±carbonate) alteration halo hosted in porphyritic tonalite |
| MEAK20GJF0007AG04 | 613699 | 5422282 | Polished thin section | - | Outcrop #2 | HBV hosted in strong sericite (±carbonate) altered porphyritic tonalite |
| MEAK20GJF0007AG05 | 613681 | 5422265 | Polished thin section | - | Outcrop #2 | 1-5 cm SRV with 2-3 cm wide sericite (±carbonate) alteration halo hosted in porphyritic tonalite |
| MEAK21GJF0086AG02 | 611930 | 5421486 | Polished thin section | - | Outcrop #3 | 1-2 cm wide LCV with 5 cm wide chlorite-carbonate alteration halo hosted in porphyritic tonalite |
| MEAK21GJF0088AG02 | 613714 | 5422237 | Polished thin section | - | BR 4216 (39-39.3m) | 1 cm wide QCC with 0.5 cm wide sericite (±carbonate) alteration halo hosted in porphyritic tonalite |
| MEAK20GJF0001AG01 | 611959 | 5420959 | Polished thin section; Geochemistry | D835751 | BR-1060 (30.1-30.4m) | 1 cm wide QCC with 0.5 cm wide sericite (±carbonate) alteration halo hosted in fine grained tonalite |
| MEAK20GJF0001AG02 | 611959 | 5420959 | Polished thin section; Geochemistry | D835752 | BR-1060 (38.2-38.5m) | Unaltered porphyritic tonalite |
| MEAK20GJF0001AG04 | 611959 | 5420959 | Polished thin section; Geochemistry | D835753 | BR-1060 (158.4-158.7m | Strong sericite (±carbonate) altered porphyritic tonalite |
| MEAK20GJF0001AG05 | 611959 | 5420959 | Polished thin section; Geochemistry | D835754 | BR-1060 (170.4-170.7m) | 1-2 cm wide QCC with 1 cm wide sericite (±carbonate) alteration halo veins hosted in fine grained tonalite |

**Table B2:** Continued.

| Sample ID | Easting | Northing | Analysis | Assay tag | Sample description | Lithology description |
|---|---|---|---|---|---|---|
| MEAK20GJF0001AG06 | 611959 | 5420959 | Polished thin section; Geochemistry | D835755 | BR-1060 (239.3-239.6m) | Moderate sericite (±carbonate) altered sheared porphyritic tonalite |
| MEAK20GJF0001AG11 | 611959 | 5420959 | Polished thin section; Geochemistry | D835756 | BR-1060 (255.6-255.9m) | HBV hosted in strong sericite (±carbonate) altered porphyritic tonalite |
| MEAK20GJF0001AG13 | 611959 | 5420959 | Polished thin section; Geochemistry | D835758 | BR-1060 (258.98-259.28m) | 1 cm wide QCC with 0.5 cm wide sericite (±carbonate) alteration halo hosted porphyritic tonalite |
| MEAK20GJF0001AG14 | 611959 | 5420959 | Polished thin section; Geochemistry | D835759 | BR-1060 (261.4-261.7m) | Strong sericite (±carbonate) altered porphyritic tonalite |
| MEAK20GJF0001AG16 | 611959 | 5420959 | Polished thin section; Geochemistry | D835760 | BR-1060 (275.7-276m) | Strong sericite-hematite (±carbonate) altered fine grained tonalite |
| MEAK20GJF0001AG18 | 611959 | 5420959 | Polished thin section; Geochemistry | D835761 | BR-1060 (292.1-292.4m) | Sheared mafic dyke |
| MEAK20GJF0001AG19 | 611959 | 5420959 | Polished thin section; Geochemistry | D835762 | BR-1060 (369.2-369.5m) | Unaltered porphyritic tonalite |
| MEAK20GJF0002AG02 | 611909 | 5421052 | Polished thin section; Geochemistry | D835763 | BR-1035 (82.35-82.85m) | Strongly sericite (±carbonate) altered porphyritic tonalite |
| MEAK20GJF0002AG03 | 611909 | 5421052 | Polished thin section; Geochemistry | D835764 | BR-1035 (84.5-84.8m) | Weak chlorite-carbonate (±sericite) altered fine grained tonalite |
| MEAK20GJF0002AG06 | 611909 | 5421052 | Polished thin section; Geochemistry | D835765 | BR-1035 (221.3-221.6m) | Strong sericite (±carbonate) altered porphyritic tonalite |
| MEAK20GJF0002AG11 | 611909 | 5421052 | Polished thin section; Geochemistry | D835766 | BR-1035 (343.7-344m) | Strong sericite (±carbonate) altered porphyritic tonalite |
| MEAK20GJF004AG01 | 611720 | 5421329 | Polished thin section; Geochemistry | D835767 | BR-1136 (27.6-27.9m) | Strong sericite-hematite (±carbonate) altered porphyritic tonalite |
| MEAK20GJF0005AG01 | 611874 | 5421103 | Polished thin section; Geochemistry | D835768 | BR-1042 (161-161.3) | 5 cm wide QCC with 2 cm wide sericite (±carbonate) alteration halo hosted in porphyritic tonalite |
| MEAK20GJF0005AG03 | 611874 | 5421103 | Polished thin section; Geochemistry | D835769 | BR-1042 (243-243.3m) | Weak chlorite-carbonate (±sericite) altered porphyritic tonalite |
| MEAK20GJF0005AG04 | 611874 | 5421103 | Polished thin section; Geochemistry | D835772 | BR-1042 (319.5-319.8m) | Pegmatite dike |

**Table B2:** Continued.

| Sample ID | Easting | Northing | Analysis | Assay tag | Sample description | Lithology description |
|---|---|---|---|---|---|---|
| MEAK20GJF0005AG05 | 611874 | 5421103 | Polished thin section; Geochemistry | D835773 | BR-1042 (432.4-432.7m) | Strong sericite (±carbonate) altered porphyritic tonalite |
| MEAK20GFJ0006AG01 | 615307 | 5422360 | Polished thin section; Geochemistry | D835774 | Outcrop #1 | Folded calcite veinlets hosted in gneissic tonalite |
| MEAK21GJF0017AG01 | 607410 | 5419189 | Polished thin section; Geochemistry | D835775 | NA | Strong sericite (±carbonate) altered and sheared porphyritic tonalite |
| MEAK21GJF0027AG01 | 607308 | 5419217 | Polished thin section; Geochemistry; TIMS | D835776 | NA | Unaltered Diversion stock tonalite |
| MEAK21GJF0029AG01 | 612829 | 5421786 | Polished thin section; Geochemistry | D835777 | NA | Strong sericite (±carbonate) altered porphyritic tonalite |
| MEAK21GJF0086AG01 | 611930 | 5421486 | Polished thin section; Geochemistry | D835778 | Outcrop #3 | HBV hosted in strong sericite (±carbonate) altered porphyritic tonalite |
| MEAK21GJF0086AG03 | 611930 | 5421486 | Polished thin section; Geochemistry | D835779 | Outcrop #3 | Strong sericite (±carbonate) altered porphyritic tonalite |
| MEAK21GJF0086AG04 | 611930 | 5421486 | Polished thin section; Geochemistry | D835780 | Outcrop #3 | Strong sericite (±carbonate) altered porphyritic tonalite |
| MEAK21GJF0086AG05 | 611930 | 5421486 | Polished thin section; Geochemistry | D835781 | Outcrop #3 | Weak chlorite-carbonate (±sericite) altered porphyritic tonalite |
| MEAK21GJF0087AG01 | 611928 | 5421486 | Polished thin section; Geochemistry | D835782 | Outcrop #4 | 5 cm wide QCC with 3 cm wide sericite (±carbonate) alteration halo hosted in a sheared porphyritic tonalite |
| MEAK21GJF0087AG02 | 611928 | 5421486 | Polished thin section; Geochemistry | D835783 | Outcrop #4 | Strong sericite (±carbonate) altered porphyritic tonalite |
| MEAK21GJF0087AG03 | 611928 | 5421486 | Polished thin section; Geochemistry | D835784 | Outcrop #4 | Strong sericite (±carbonate) altered porphyritic tonalite |
| MEAK21GJF0087AG04 | 611928 | 5421486 | Polished thin section; Geochemistry | D835785 | Outcrop #4 | Weak chlorite-carbonate (±sericite) altered porphyritic tonalite |
| MEAK21GJF0088AG01 | 613714 | 5422237 | Polished thin section; Geochemistry | D835786 | BR 4216 (27-27.3m) | HBV hosted in strong sericite (±carbonate) altered porphyritic tonalite |
| MEAK21GJF0088AG03 | 613714 | 5422237 | Polished thin section; Geochemistry | D835787 | BR 4216 (168.8-169.3m) | HBV hosted in strong sericite (±carbonate) altered porphyritic tonalite |

**Table B2:** Continued.

| Sample ID | Easting | Northing | Analysis | Assay tag | Sample description | Lithology description |
|---|---|---|---|---|---|---|
| MEAK21GJF0088AG04 | 613714 | 5422237 | Polished thin section; Geochemistry | D835788 | BR 4216 (188.6-188.9m) | Weak chlorite-carbonate (±sericite) altered porphyritic tonalite |
| MEAK21GJF0089AG01 | 613684 | 5422304 | Polished thin section; Geochemistry | D835789 | BR 4248 (18.6-18.9m) | Strong sericite (±carbonate) altered porphyritic tonalite |
| MEAK21GJF0089AG02 | 613684 | 5422304 | Polished thin section; Geochemistry | D835792 | BR 4248 (28-28.3m) | HBV hosted in strong sericite (±carbonate) altered porphyritic tonalite |
| MEAK21GJF0089AG03 | 613684 | 5422304 | Polished thin section; Geochemistry | D835793 | BR 4248 (99-99.3m) | Weak chlorite-carbonate (±sericite) altered porphyritic tonalite |
| MEAK21GJF0090AG01 | 613846 | 5422065 | Polished thin section; Geochemistry | D835794 | BR 4025 (120.6-120.9m) | Strong sericite (±carbonate) altered and sheared porphyritic tonalite |
| MEAK21GJF0090AG02 | 613846 | 5422065 | Polished thin section; Geochemistry | D835795 | BR 4025 (286.3-286.6m) | Strong sericite (±carbonate) altered porphyritic tonalite |
| MEAK21GJF0090AG03 | 613846 | 5422065 | Polished thin section; Geochemistry | D835796 | BR 4025 (332.6-332.9m) | Weak chlorite-carbonate (±sericite) altered porphyritic tonalite |
| MEAK21GJF0091AG01 | 613755 | 5422188 | Polished thin section; Geochemistry | D835797 | BR 4035 (33.8-34.1m) | Weak chlorite-carbonate (±sericite) altered porphyritic tonalite |
| MEAK21GJF0091AG02 | 613755 | 5422188 | Polished thin section; Geochemistry | D835798 | BR 4035 (42.5-42.8m) | 5-10 cm wide LCV with 5 cm wide chlorite-carbonate alteration halo hosted in porphyritic tonalite |
| MEAK21GJF0091AG03 | 613755 | 5422188 | Polished thin section; Geochemistry | D835799 | BR 4035 (69-69.4m) | Strong sericite (±carbonate) altered porphyritic tonalite |
| MEAK21GJF0091AG04 | 613755 | 5422188 | Polished thin section; Geochemistry | D835800 | BR 4035 (199.7-200m) | Weak chlorite-carbonate (±sericite) altered porphyritic tonalite |
| MEAK21GJF0092AG01 | 615312 | 5422580 | Polished thin section; Geochemistry | D835801 | BR 0365 (56.3-56.6m) | 1-5 cm wide SRV vein with 1-2 cm wide sericite (±carbonate) altered porphyritic tonalite |
| MEAK21GJF0092AG02 | 615312 | 5422580 | Polished thin section; Geochemistry | D835802 | BR 0365 (78-78.3m) | HBV hosted in strong sericite (±carbonate) altered porphyritic tonalite |
| MEAK21GJF0092AG03 | 615312 | 5422580 | Polished thin section; Geochemistry | D835803 | BR 0365 (197-197.3m) | Strong sericite (±carbonate) altered porphyritic tonalite |
| MEAK21GJF0092AG04 | 615312 | 5422580 | Polished thin section; Geochemistry | D835804 | BR 0365 (314.4-314.7m) | Strong sericite (±carbonate) altered and sheared porphyritic tonalite |

**Table B2:** Continued.

| Sample ID | Easting | Northing | Analysis | Assay tag | Sample description | Lithology description |
|---|---|---|---|---|---|---|
| MEAK21GJF0092AG05 | 615312 | 5422580 | Polished thin section; Geochemistry | D835805 | BR 0365 (386.2-386.5m) | Weak chlorite-carbonate (±sericite) altered porphyritic tonalite |
| MEAK21GJF0098AG01 | 617166 | 5422019 | Polished thin section; Geochemistry | D835806 | Outcrop #6 | Strong sericite (±carbonate) altered porphyritic tonalite |
| MEAK21GJF0098AG02 | 617166 | 5422019 | Polished thin section; Geochemistry | D835807 | Outcrop #6 | Strong sericite (±carbonate) altered porphyritic tonalite |
| MEAK21GJF0098AG03 | 617166 | 5422019 | Polished thin section; Geochemistry | D835808 | Outcrop #6 | Weak chlorite-carbonate (±sericite) altered porphyritic tonalite |
| MEAK21GJF0098AG04 | 617166 | 5422019 | Polished thin section; Geochemistry | D835809 | Outcrop #6 | 1-5 cm wide extensional veins hosted in porphyritic tonalite |
| MEAK21GJF0098AG05 | 617166 | 5422019 | Polished thin section; Geochemistry | D835812 | Outcrop #6 | Strong sericite (±carbonate) altered and sheared porphyritic tonalite |

Notes: LCV, laminated crustiform vein; QCC, quartz chlorite carbonate vein; HBV, hydrothermal breccia vein; SRV, sulfide rich veins.

## Appendix C: Whole rock geochemistry and assay analysis

Hammond Reef whole rock geochemistry and assay analysis from 2020-2021 available in excel format (Appendix C)

**Table C4:** Concentration data for major and trace elements from collected samples

| Analyte | Rock Type | Vein Type | Alt. type | Northing | Easting | $SiO_2$ | $Al_2O_3$ | $Fe_2O_3$ | CaO | MgO | $Na_2O$ |
|---|---|---|---|---|---|---|---|---|---|---|---|
| **Unit** | | | | | | wt. % | wt. % | wt. % | wt. % | wt. % | wt. % |
| **LDL** | | | | | | 0.01 | 0.01 | 0.01 | 0.01 | 0.01 | 0.01 |
| **Method** | | | | | | FUS-ICP | FUS-ICP | FUS-ICP | FUS-ICP | FUS-ICP | FUS-ICP |
| **D835751** | FGT | Na | Ser (±carb) | 611959 | 5420959 | 65 | 15.25 | 5.26 | 2.83 | 1.28 | 4.08 |
| **D835752** | PT | Na | Chl-carb (±ser) | 611959 | 5420959 | 65.2 | 15.45 | 4.45 | 3.65 | 1.47 | 4.09 |
| **D835753** | PT | Na | Ser (±carb) | 611959 | 5420959 | 70.8 | 16 | 1.76 | 0.97 | 0.36 | 3.58 |
| **D835754** | PT | QCC | Ser (±carb) | 611959 | 5420959 | 57.2 | 15.35 | 5.3 | 4.62 | 1.83 | 1.98 |
| **D835755** | PT | Na | Ser (±carb) | 611959 | 5420959 | 61.8 | 13.9 | 5 | 3.85 | 1.98 | 3.06 |
| **D835756** | PT | HBV | Ser (±carb) | 611959 | 5420959 | 79.1 | 6.32 | 4.41 | 2.03 | 0.75 | 0.18 |
| **D835757** | Blank | | | | | 11 | 0.1 | 0.17 | 49.6 | 1.87 | 0.02 |
| **D835758** | PT | QCC | Ser (±carb) | 611959 | 5420959 | 76.5 | 11.55 | 1.78 | 1.84 | 0.48 | 3.46 |
| **D835759** | PT | QCC | Ser (±carb) | 611959 | 5420959 | 57.8 | 14.55 | 6.47 | 4.51 | 2.1 | 1.97 |
| **D835760** | PT | Na | Ser (±carb) | 611959 | 5420959 | 61 | 13.4 | 4.66 | 3.97 | 1.84 | 1.98 |
| **D835761** | MD | Na | Ser (±carb) | 611959 | 5420959 | 47 | 11.85 | 12.7 | 6.97 | 7.2 | 1.69 |
| **D835762** | PT | Na | Chl-carb (±ser) | 611959 | 5420959 | 68.3 | 15.1 | 3.95 | 2.79 | 1 | 3.93 |
| **D835763** | PT | Na | Ser (±carb) | 611909 | 5421052 | 75.4 | 13.4 | 1.43 | 1.97 | 0.19 | 5.09 |
| **D835764** | PT | QCC | Ser (±carb) | 611909 | 5421052 | 61.9 | 14.85 | 6.4 | 3.96 | 1.32 | 2.62 |
| **D835765** | PT | LCV | Chl-carb (±ser) | 611909 | 5421052 | 69.9 | 13.25 | 3.8 | 2.52 | 0.69 | 3 |
| **D835766** | PT | Na | Ser (±carb) | 611909 | 5421052 | 55.2 | 15.25 | 7.56 | 5.47 | 1.6 | 1.58 |
| **D835767** | PT | Na | Ser (±carb) | 611720 | 5421329 | 64.7 | 14 | 2.93 | 3.59 | 1 | 2.89 |
| **D835768** | PT | HBV | Ser (±carb) | 611874 | 5421103 | 93.3 | 4.17 | 0.76 | 0.07 | 0.08 | 1.32 |
| **D835769** | FGT | Na | Chl-carb (±ser) | 611874 | 5421103 | 63.4 | 15.35 | 6.69 | 5.23 | 2.54 | 3.54 |
| **D835770** | standard (ORCA-1) | | | | | 76.5 | 12.55 | 2.85 | 1.15 | 0.47 | 4.64 |
| **D835771** | Blank | | | | | 9.38 | 0.07 | 0.14 | 50.9 | 2.02 | 0.02 |
| **D835772** | PT | Na | Ser (±carb) | 611874 | 5421103 | 75.3 | 13.85 | 1.6 | 1.35 | 0.23 | 4.83 |
| **D835773** | PT | Na | Ser (±carb) | 611874 | 5421103 | 77.3 | 12.75 | 0.68 | 2.55 | 0.06 | 3.86 |
| **D835774** | PT | QCC | Ser (±carb) | 615307 | 5422360 | 55.8 | 15.15 | 5.71 | 4.7 | 2.26 | 1.41 |
| **D835775** | PT | Na | Ser (±carb) | 607410 | 5419189 | 73.9 | 14.35 | 2.13 | 1.15 | 0.42 | 3.5 |
| **D835776** | PT | Na | Chl-carb (±ser) | 607308 | 5419217 | 77.5 | 13.2 | 1.03 | 0.45 | 0.11 | 4.06 |
| **D835777** | PT | Na | Ser (±carb) | 612829 | 5421786 | 90.1 | 5.98 | 1.42 | 0.08 | 0.11 | 2.09 |
| **D835778** | PT | HBV | Ser (±carb) | 611930 | 5421486 | 95.9 | 1.5 | 1.24 | 0.69 | 0.22 | 0.39 |
| **D835779** | PT | Na | Ser (±carb) | 611930 | 5421486 | 78.3 | 13 | 1.53 | 0.65 | 0.19 | 4.5 |
| **D835780** | PT | Na | Ser (±carb) | 611930 | 5421486 | 62.7 | 15.4 | 4.42 | 4.39 | 1.49 | 2.67 |
| **D835781** | PT | Na | Chl-carb (±ser) | 611930 | 5421486 | 74 | 14.55 | 2.48 | 2.72 | 0.56 | 4.6 |
| **D835782** | PT | Na | Ser (±carb) | 611928 | 5421486 | 79 | 13 | 1.63 | 0.18 | 0.23 | 4.27 |
| **D835783** | PT | Na | Ser (±carb) | 611928 | 5421486 | 76.7 | 12.95 | 2.87 | 0.07 | 0.41 | 2.15 |
| **D835784** | PT | Na | Ser (±carb) | 611928 | 5421486 | 72.8 | 13.45 | 1.68 | 2.81 | 0.46 | 4.97 |
| **D835785** | PT | Na | Chl-carb (±ser) | 611928 | 5421486 | 68.5 | 14.9 | 3.64 | 3.09 | 1 | 4.26 |
| **D835786** | PT | Na | Chl-carb (±ser) | 613714 | 5422237 | 52.5 | 20.7 | 4.33 | 2.73 | 1.71 | 6.03 |
| **D835787** | PT | HBV | Ser (±carb) | 613714 | 5422237 | 71.9 | 12.6 | 3.15 | 2.81 | 0.74 | 2.47 |
| **D835788** | PT | Na | Chl-carb (±ser) | 613714 | 5422237 | 70.3 | 14.7 | 3.61 | 3.54 | 0.78 | 4.17 |
| **D835789** | PT | Na | Ser (±carb) | 613684 | 5422304 | 68.9 | 14.3 | 2.72 | 3.05 | 0.72 | 3.18 |
| **D835790** | standard (NIP-1-427) | | | | | 48.9 | 15.2 | 13.5 | 10.3 | 7.33 | 2.42 |
| **D835791** | Blank | | | | | 8.58 | 0.12 | 0.11 | 51.6 | 2.05 | 0.03 |
| **D835792** | PT | Na | Ser (±carb) | 613684 | 5422304 | 75.9 | 13.25 | 1.33 | 1.67 | 0.19 | 3.63 |
| **D835793** | PT | Na | Chl-carb (±ser) | 613684 | 5422304 | 70 | 14.05 | 3.1 | 2.93 | 0.68 | 3.83 |
| **D835794** | PT | Na | Ser (±carb) | 613846 | 5422065 | 64.9 | 13.15 | 4.17 | 4.16 | 1.76 | 0.55 |
| **D835795** | PT | Na | Ser (±carb) | 613846 | 5422065 | 69.3 | 13.35 | 2.93 | 2.96 | 0.73 | 2.44 |
| **D835796** | PT | Na | Chl-carb (±ser) | 613846 | 5422065 | 67.8 | 14.95 | 4.35 | 4.04 | 1.17 | 3.83 |
| **D835797** | PT | Na | Chl-carb (±ser) | 613755 | 5422188 | 65.8 | 12.95 | 3.92 | 3.07 | 1.58 | 2.45 |
| **D835798** | PT | LCV | Chl-carb (±ser) | 613755 | 5422188 | 35.7 | 3.79 | 11.2 | 14.15 | 10.4 | 0.01 |
| **D835799** | PT | Na | Ser (±carb) | 613755 | 5422188 | 67.1 | 13.95 | 3.85 | 3.33 | 1.25 | 2.56 |
| **D835800** | PT | Na | Chl-carb (±ser) | 613755 | 5422188 | 72.7 | 13.5 | 2.43 | 2.24 | 0.39 | 4.05 |
| **D835801** | PT | SRV | Ser (±carb) | 615312 | 5422580 | 57.6 | 13.95 | 4.27 | 6.86 | 1.19 | 1.99 |
| **D835802** | PT | QCC | Ser (±carb) | 615312 | 5422580 | 72.3 | 11.1 | 3.67 | 3.13 | 1.14 | 0.89 |
| **D835803** | PT | Na | Ser (±carb) | 615312 | 5422580 | 75.2 | 13.1 | 1.39 | 1.46 | 0.28 | 4.5 |
| **D835804** | PT | QCC | Ser (±carb) | 615312 | 5422580 | 63.2 | 13.6 | 4.55 | 4.18 | 2.17 | 4.04 |
| **D835805** | PT | Na | Chl-carb (±ser) | 615312 | 5422580 | 73.5 | 13.9 | 3.06 | 3.07 | 0.69 | 4.02 |
| **D835806** | PT | Na | Ser (±carb) | 617166 | 5422019 | 71.7 | 15 | 3.14 | 1.58 | 0.46 | 3.08 |
| **D835807** | PT | Na | Ser (±carb) | 617166 | 5422019 | 74.6 | 14 | 2.04 | 2.11 | 0.5 | 3.75 |
| **D835808** | PT | Na | Chl-carb (±ser) | 617166 | 5422019 | 68.1 | 16.65 | 3.74 | 1.03 | 1.51 | 3.72 |
| **D835809** | PT | QCC | Ser (±carb) | 617166 | 5422019 | 74.1 | 11.15 | 3.09 | 2.73 | 0.47 | 0.2 |
| **D835810** | standard (ORCA-1) | | | | | 75.9 | 12.5 | 2.78 | 1.12 | 0.47 | 4.63 |
| **D835811** | Blank | | | | | 10.25 | 0.14 | 0.17 | 50.9 | 2.18 | 0.03 |
| **D835812** | PT | QCC | Ser (±carb) | 617166 | 5422019 | 100 | 0.25 | 0.53 | 0.16 | 0.02 | 0.01 |

**Table C3:** Continued.

| Analyte | K2O | Cr2O3 | TiO2 | MnO | P2O5 | SrO | BaO | LOI | Total | Au | Ag |
|---|---|---|---|---|---|---|---|---|---|---|---|
| **Unit** | wt. % | wt. % | wt. % | wt. % | wt. % | wt. % | wt. % | wt. % | wt. % | ppm | ppm |
| **LDL** | 0.01 | 0.01 | 0.01 | 0.01 | 0.01 | 0.01 | 0.01 | 0.01 |  | 0.001 | 0.5 |
| **Method** | FUS-ICP | FUS-ICP | FUS-ICP | FUS-ICP | FUS-ICP | FUS-ICP | FUS-ICP | FUS-ICP |  | INAA | TD-ICP |
| **D835751** | 2.13 | 0.003 | 0.61 | 0.07 | 0.2 | 0.02 | 0.04 | 3.03 | 99.8 | 0.066 | <0.5 |
| **D835752** | 1.25 | 0.004 | 0.44 | 0.06 | 0.12 | 0.05 | 0.03 | 1.82 | 98.08 | <0.001 | <0.5 |
| **D835753** | 3.31 | 0.004 | 0.14 | 0.02 | 0.04 | 0.01 | 0.11 | 2.04 | 99.14 | 0.082 | <0.5 |
| **D835754** | 4.15 | 0.004 | 0.52 | 0.09 | 0.1 | 0.01 | 0.08 | 7.4 | 98.63 | 1.74 | 4.1 |
| **D835755** | 2.5 | 0.011 | 0.49 | 0.07 | 0.14 | 0.02 | 0.04 | 6.17 | 99.03 | 0.132 | <0.5 |
| **D835756** | 1.9 | 0.007 | 0.19 | 0.04 | <0.01 | <0.01 | 0.03 | 3.83 | 98.79 | 104 | 11.2 |
| **D835757** | 0.01 | <0.002 | 0.01 | 0.01 | 0.01 | 0.01 | <0.01 | 37.9 | 100.71 | 0.005 | <0.5 |
| **D835758** | 1.91 | 0.005 | 0.13 | 0.03 | 0.03 | 0.01 | 0.03 | 2.77 | 100.53 | 0.094 | <0.5 |
| **D835759** | 3.5 | 0.01 | 0.61 | 0.11 | 0.13 | 0.01 | 0.06 | 7.52 | 99.35 | 1.26 | <0.5 |
| **D835760** | 3.58 | 0.008 | 0.46 | 0.09 | 0.11 | 0.01 | 0.05 | 6.87 | 98.03 | 0.947 | 0.6 |
| **D835761** | 0.51 | 0.038 | 1.15 | 0.16 | 0.07 | 0.02 | 0.01 | 11.3 | 100.67 | 0.007 | <0.5 |
| **D835762** | 1.91 | 0.006 | 0.37 | 0.05 | 0.12 | 0.02 | 0.04 | 2.21 | 99.8 | 0.002 | <0.5 |
| **D835763** | 1.64 | 0.003 | 0.1 | 0.03 | 0.03 | 0.02 | 0.04 | 2.14 | 101.48 | 0.001 | <0.5 |
| **D835764** | 2.87 | 0.005 | 0.67 | 0.08 | 0.29 | 0.02 | 0.05 | 4.65 | 99.69 | 0.008 | <0.5 |
| **D835765** | 2.91 | 0.003 | 0.32 | 0.05 | 0.14 | 0.01 | 0.06 | 3.99 | 100.64 | 2.71 | 0.7 |
| **D835766** | 3.79 | 0.005 | 0.83 | 0.1 | 0.34 | 0.02 | 0.06 | 6.48 | 98.29 | 2.9 | 0.9 |
| **D835767** | 2.78 | 0.003 | 0.38 | 0.07 | 0.09 | 0.01 | 0.04 | 5.79 | 98.27 | 0.137 | 0.5 |
| **D835768** | 0.69 | 0.006 | 0.02 | 0.01 | <0.01 | <0.01 | 0.02 | 0.44 | 100.89 | 0.169 | 0.8 |
| **D835769** | 0.98 | 0.009 | 0.64 | 0.09 | 0.21 | 0.03 | 0.02 | 2.46 | 101.19 | 0.002 | <0.5 |
| **D835770** | 2.16 | 0.01 | 0.3 | 0.06 | 0.05 | 0.01 | 0.04 | 0.79 | 101.58 | <0.001 | <0.5 |
| **D835771** | <0.01 | <0.002 | 0.01 | 0.01 | 0.02 | 0.01 | <0.01 | 38.6 | 101.18 | <0.001 | <0.5 |
| **D835772** | 3.04 | 0.005 | 0.1 | 0.05 | 0.03 | 0.01 | 0.06 | 1.46 | 101.92 | <0.001 | <0.5 |
| **D835773** | 0.5 | 0.005 | 0.04 | 0.01 | 0.01 | 0.03 | 0.01 | 2.92 | 100.73 | <0.001 | <0.5 |
| **D835774** | 4.68 | 0.006 | 0.57 | 0.09 | 0.22 | 0.01 | 0.06 | 8.2 | 98.87 | 0.015 | <0.5 |
| **D835775** | 3.36 | 0.003 | 0.19 | 0.03 | 0.05 | 0.01 | 0.07 | 2.14 | 101.3 | <0.001 | <0.5 |
| **D835776** | 3.89 | 0.003 | 0.07 | 0.03 | 0.01 | 0.01 | 0.09 | 0.86 | 101.31 | 0.043 | <0.5 |
| **D835777** | 0.9 | 0.008 | 0.09 | 0.02 | 0.02 | <0.01 | 0.02 | 0.69 | 101.53 | 0.003 | <0.5 |
| **D835778** | 0.3 | 0.009 | 0.05 | 0.02 | <0.01 | <0.01 | <0.01 | 1.11 | 101.43 | 8.45 | 63.1 |
| **D835779** | 1.99 | 0.006 | 0.09 | 0.01 | 0.04 | 0.01 | 0.04 | 1.34 | 101.7 | 0.277 | 0.6 |
| **D835780** | 2.99 | 0.006 | 0.5 | 0.06 | 0.15 | 0.02 | 0.04 | 5.53 | 100.37 | 0.01 | <0.5 |
| **D835781** | 0.59 | 0.004 | 0.34 | 0.02 | 0.1 | 0.04 | 0.02 | 1.13 | 101.15 | <0.001 | <0.5 |
| **D835782** | 2.11 | 0.003 | 0.14 | 0.02 | 0.05 | 0.02 | 0.04 | 1.11 | 101.8 | 0.002 | <0.5 |
| **D835783** | 3.29 | 0.004 | 0.23 | 0.03 | 0.06 | 0.01 | 0.07 | 1.82 | 100.66 | 1.065 | <0.5 |
| **D835784** | 0.7 | 0.003 | 0.21 | 0.02 | 0.07 | 0.03 | 0.01 | 2.69 | 99.9 | 0.003 | <0.5 |
| **D835785** | 1.57 | 0.004 | 0.31 | 0.05 | 0.1 | 0.03 | 0.04 | 2.84 | 100.33 | 0.136 | <0.5 |
| **D835786** | 4.03 | 0.002 | 0.56 | 0.05 | 0.02 | 0.02 | 0.08 | 5.9 | 98.66 | 0.154 | 0.7 |
| **D835787** | 2.62 | 0.006 | 0.27 | 0.05 | 0.12 | 0.02 | 0.05 | 4.04 | 100.85 | 0.084 | <0.5 |
| **D835788** | 1.34 | 0.003 | 0.41 | 0.05 | 0.13 | 0.03 | 0.02 | 1.72 | 100.8 | <0.001 | <0.5 |
| **D835789** | 2.88 | 0.004 | 0.22 | 0.05 | 0.06 | 0.02 | 0.06 | 4.8 | 100.96 | 0.062 | <0.5 |
| **D835790** | 0.46 | 0.023 | 1.14 | 0.19 | 0.11 | 0.02 | 0.02 | 0.15 | 99.76 | 0.005 | <0.5 |
| **D835791** | 0.01 | <0.002 | 0.01 | 0.01 | 0.02 | 0.01 | <0.01 | 38.6 | 101.15 | <0.001 | <0.5 |
| **D835792** | 2.34 | 0.005 | 0.08 | 0.02 | 0.04 | 0.01 | 0.06 | 2.36 | 100.89 | 0.059 | <0.5 |
| **D835793** | 2.14 | 0.004 | 0.32 | 0.05 | 0.11 | 0.02 | 0.04 | 3.39 | 100.66 | 0.023 | <0.5 |
| **D835794** | 4.08 | 0.003 | 0.37 | 0.06 | 0.09 | 0.01 | 0.07 | 7.53 | 100.9 | 0.054 | <0.5 |
| **D835795** | 3.02 | 0.004 | 0.25 | 0.04 | 0.09 | 0.02 | 0.07 | 4.92 | 100.12 | <0.001 | <0.5 |
| **D835796** | 1.02 | 0.005 | 0.4 | 0.06 | 0.13 | 0.03 | 0.04 | 1.64 | 99.47 | <0.001 | <0.5 |
| **D835797** | 3.03 | 0.007 | 0.4 | 0.06 | 0.11 | 0.01 | 0.06 | 5.58 | 99.03 | 0.016 | <0.5 |
| **D835798** | 0.01 | 0.157 | 0.8 | 0.22 | 0.03 | 0.04 | <0.01 | 22.2 | 98.71 | 0.169 | <0.5 |
| **D835799** | 3.3 | 0.003 | 0.36 | 0.07 | 0.09 | 0.01 | 0.05 | 5.98 | 101.9 | 0.232 | <0.5 |
| **D835800** | 2.04 | 0.005 | 0.16 | 0.04 | 0.06 | 0.02 | 0.09 | 2.74 | 100.47 | 0.019 | <0.5 |
| **D835801** | 3.59 | 0.006 | 0.41 | 0.09 | 0.11 | 0.03 | 0.09 | 8.49 | 98.68 | 0.004 | <0.5 |
| **D835802** | 3.33 | 0.007 | 0.34 | 0.07 | 0.15 | 0.01 | 0.07 | 4.06 | 100.27 | 0.091 | 2 |
| **D835803** | 1.9 | 0.003 | 0.09 | 0.02 | 0.02 | 0.02 | 0.07 | 2.09 | 100.14 | 0.002 | <0.5 |
| **D835804** | 1.78 | 0.012 | 0.38 | 0.09 | 0.09 | 0.02 | 0.03 | 6.56 | 100.7 | 0.016 | <0.5 |
| **D835805** | 1.02 | 0.004 | 0.3 | 0.05 | 0.11 | 0.02 | 0.03 | 1.19 | 100.96 | <0.001 | <0.5 |
| **D835806** | 3.12 | 0.004 | 0.36 | 0.04 | 0.14 | 0.01 | 0.07 | 3.06 | 101.76 | <0.001 | <0.5 |
| **D835807** | 1.67 | 0.007 | 0.18 | 0.02 | 0.06 | 0.02 | 0.04 | 2.74 | 101.74 | <0.001 | <0.5 |
| **D835808** | 2.35 | 0.004 | 0.41 | 0.02 | 0.13 | 0.02 | 0.06 | 2.75 | 100.49 | <0.001 | <0.5 |
| **D835809** | 3.67 | 0.006 | 0.33 | 0.03 | 0.12 | <0.01 | 0.05 | 4.01 | 99.96 | 0.01 | <0.5 |
| **D835810** | 2.16 | 0.011 | 0.29 | 0.06 | 0.06 | <0.01 | 0.04 | 0.8 | 100.82 | <0.001 | <0.5 |
| **D835811** | 0.03 | <0.002 | 0.01 | 0.01 | 0.02 | <0.01 | <0.01 | 38 | 101.74 | <0.001 | <0.5 |
| **D835812** | 0.11 | 0.01 | <0.01 | 0.01 | <0.01 | <0.01 | <0.01 | 0.23 | 101.33 | 12.9 | 1.8 |

**Table C3:** Continued.

| **Analyte** | **Ba** | **Ce** | **Cr** | **Cs** | **Dy** | **Er** | **Eu** | **Ga** | **Gd** | **Ge** | **Hf** |
|---|---|---|---|---|---|---|---|---|---|---|---|
| **Unit** | ppm | ppm | ppm | ppm | ppm | ppm | ppm | ppm | ppm | ppm | ppm |
| **LDL** | 0.5 | 0.5 | 10 | 0.01 | 0.05 | 0.03 | 0.03 | 0.1 | 0.05 | 5 | 0.2 |
| **Method** | FUS-MS | FUS-MS | FUS-MS | FUS-MS | FUS-MS | FUS-MS | FUS-MS | FUS-MS | FUS-MS | FUS-MS | FUS-MS |
| **D835751** | 363 | 74.6 | 30 | 1.04 | 3.29 | 1.7 | 1.31 | 21.5 | 4.3 | <5 | 5.5 |
| **D835752** | 303 | 81.1 | 30 | 0.58 | 1.04 | 0.52 | 0.74 | 19.9 | 1.63 | <5 | 4.4 |
| **D835753** | 918 | 37.6 | 30 | 0.98 | 1.12 | 0.49 | 0.55 | 20 | 1.9 | <5 | 2.7 |
| **D835754** | 654 | 38.6 | 20 | 1.61 | 2.37 | 1.32 | 0.85 | 22.2 | 2.65 | <5 | 3.5 |
| **D835755** | 339 | 43.6 | 80 | 1.17 | 3.03 | 1.73 | 1.12 | 16.7 | 3.45 | <5 | 4.5 |
| **D835756** | 279 | 13.9 | 50 | 0.63 | 0.75 | 0.46 | 0.34 | 11.6 | 0.77 | <5 | 1.4 |
| **D835757** | 20.1 | 2.9 | 10 | 0.03 | 0.41 | 0.21 | 0.04 | 0.2 | 0.34 | <5 | 0.1 |
| **D835758** | 287 | 29.1 | 40 | 0.65 | 1.14 | 0.6 | 0.39 | 13.2 | 1.56 | <5 | 2.3 |
| **D835759** | 498 | 35.1 | 60 | 1.16 | 2.96 | 1.77 | 1.03 | 22.5 | 3.39 | <5 | 4 |
| **D835760** | 460 | 43.3 | 60 | 1.42 | 2.54 | 1.58 | 0.95 | 18.8 | 3.19 | <5 | 3.8 |
| **D835761** | 85.6 | 18.9 | 250 | 0.27 | 3.02 | 1.81 | 0.91 | 17.5 | 3.15 | <5 | 1.7 |
| **D835762** | 359 | 65.9 | 40 | 0.71 | 3.3 | 1.61 | 0.95 | 20 | 3.44 | <5 | 5.4 |
| **D835763** | 368 | 23.8 | 30 | 0.6 | 2.23 | 1.41 | 0.47 | 18.1 | 2.33 | <5 | 2.7 |
| **D835764** | 481 | 72.3 | 30 | 1.14 | 4.4 | 2.35 | 1.51 | 21.8 | 5.82 | <5 | 6.4 |
| **D835765** | 522 | 120 | 20 | 1.11 | 3.31 | 1.29 | 1.45 | 20 | 6 | <5 | 6.9 |
| **D835766** | 550 | 84.4 | 40 | 1.3 | 5.29 | 2.86 | 1.63 | 24.9 | 6.1 | <5 | 8.1 |
| **D835767** | 395 | 48.2 | 20 | 1.23 | 1.03 | 0.52 | 0.63 | 17.6 | 1.64 | <5 | 3.2 |
| **D835768** | 147 | 8.9 | 50 | 0.26 | 0.43 | 0.24 | 0.11 | 5.1 | 0.42 | <5 | 0.9 |
| **D835769** | 213 | 56.5 | 60 | 0.55 | 3.54 | 1.83 | 1.25 | 20.5 | 4.27 | <5 | 4.8 |
| **D835770** | 372 | 63.2 | 70 | 0.6 | 11.3 | 7.45 | 1.3 | 16.1 | 9.58 | <5 | 7.8 |
| **D835771** | 17.1 | 0.9 | <10 | 0.02 | 0.17 | 0.12 | 0.04 | 0.2 | 0.16 | <5 | <0.1 |
| **D835772** | 500 | 25.5 | 40 | 0.63 | 4.25 | 2.76 | 0.52 | 19 | 3.3 | <5 | 3.4 |
| **D835773** | 67.9 | 10.4 | 40 | 0.23 | 1.02 | 0.61 | 0.25 | 13.2 | 1.05 | <5 | 2.6 |
| **D835774** | 499 | 24.2 | 30 | 1.55 | 3.02 | 1.64 | 0.94 | 18.4 | 3.13 | <5 | 4.2 |
| **D835775** | 620 | 41.4 | 20 | 1.43 | 1.53 | 0.93 | 0.43 | 19.2 | 1.72 | <5 | 3.4 |
| **D835776** | 801 | 32.5 | 20 | 0.92 | 1.51 | 0.86 | 0.55 | 15.9 | 1.66 | <5 | 1.7 |
| **D835777** | 162 | 28.7 | 60 | 0.41 | 0.77 | 0.32 | 0.38 | 6.9 | 1.19 | <5 | 1.8 |
| **D835778** | 47.5 | 4.2 | 60 | 0.11 | 0.53 | 0.32 | 0.11 | 2.5 | 0.4 | <5 | 0.5 |
| **D835779** | 337 | 11.5 | 50 | 0.63 | 1.6 | 1.04 | 0.33 | 16 | 1.35 | <5 | 2.1 |
| **D835780** | 374 | 39 | 40 | 0.95 | 3.24 | 1.7 | 0.76 | 19.9 | 3.7 | <5 | 5.3 |
| **D835781** | 193 | 93.7 | 30 | 0.23 | 2.35 | 1.64 | 0.97 | 19.3 | 2.82 | <5 | 6.4 |
| **D835782** | 354 | 46.3 | 20 | 0.69 | 0.92 | 0.5 | 0.44 | 14.4 | 1.1 | <5 | 2.1 |
| **D835783** | 586 | 97.6 | 30 | 1.12 | 1.23 | 0.55 | 0.73 | 19.6 | 1.83 | <5 | 3 |
| **D835784** | 125 | 42.9 | 20 | 0.27 | 1.58 | 0.81 | 0.79 | 18.6 | 1.88 | <5 | 3.5 |
| **D835785** | 381 | 62.8 | 30 | 0.41 | 2.14 | 1.15 | 0.81 | 21.5 | 2.4 | <5 | 4.6 |
| **D835786** | 708 | 87.8 | 10 | 1.4 | 1.84 | 0.65 | 1.19 | 29.9 | 3.59 | <5 | 6.8 |
| **D835787** | 464 | 69.8 | 40 | 0.73 | 2.32 | 0.96 | 0.86 | 17.7 | 3.57 | <5 | 3.8 |
| **D835788** | 188 | 39.1 | 20 | 0.48 | 2.84 | 1.65 | 0.77 | 19.1 | 2.49 | <5 | 5.1 |
| **D835789** | 552 | 60.4 | 30 | 0.78 | 2.62 | 1.63 | 0.72 | 18.5 | 2.9 | <5 | 4.7 |
| **D835790** | 145.5 | 21.7 | 160 | 0.58 | 4.15 | 2.3 | 1.18 | 20.1 | 4.16 | <5 | 2.3 |
| **D835791** | 24.1 | 1.3 | <10 | 0.01 | 0.17 | 0.17 | 0.04 | 0.3 | 0.23 | <5 | 0.1 |
| **D835792** | 563 | 44.5 | 30 | 0.74 | 1.5 | 0.66 | 0.76 | 14.3 | 2.13 | <5 | 2.9 |
| **D835793** | 295 | 45.2 | 30 | 0.69 | 3.24 | 1.63 | 0.9 | 18.4 | 3.22 | <5 | 4.4 |
| **D835794** | 639 | 39.8 | 20 | 1.17 | 2.13 | 1.16 | 0.64 | 20.3 | 2.42 | <5 | 3.1 |
| **D835795** | 592 | 51.6 | 30 | 0.76 | 1.54 | 0.62 | 0.63 | 17.8 | 2.24 | <5 | 3.8 |
| **D835796** | 334 | 64.4 | 40 | 0.34 | 2.62 | 1.42 | 0.96 | 18.9 | 3.24 | <5 | 5.5 |
| **D835797** | 516 | 51.4 | 50 | 0.78 | 2.02 | 1.1 | 0.77 | 17.3 | 2.45 | <5 | 4.8 |
| **D835798** | 31.6 | 13.2 | 1130 | 0.04 | 2.31 | 1.09 | 1.02 | 7.9 | 2.77 | <5 | 1.2 |
| **D835799** | 447 | 33.9 | 20 | 0.95 | 2.11 | 1.19 | 0.58 | 17.2 | 2.38 | <5 | 3.4 |
| **D835800** | 828 | 67.7 | 30 | 0.7 | 2.4 | 1.08 | 0.79 | 16.8 | 3.58 | <5 | 4.7 |
| **D835801** | 854 | 30.5 | 40 | 0.82 | 3.05 | 1.64 | 1.46 | 19.8 | 3.26 | <5 | 3.8 |
| **D835802** | 677 | 46.3 | 40 | 1.14 | 1.77 | 0.97 | 0.9 | 16.6 | 2.62 | <5 | 2.6 |
| **D835803** | 652 | 15.6 | 30 | 0.49 | 0.73 | 0.3 | 0.42 | 14.2 | 1.08 | <5 | 2.4 |
| **D835804** | 278 | 43.4 | 90 | 0.47 | 2.04 | 0.98 | 0.7 | 18.3 | 2.56 | <5 | 3.5 |
| **D835805** | 279 | 181.5 | 30 | 0.42 | 3.36 | 1.64 | 1.11 | 18.3 | 5.85 | <5 | 6.6 |
| **D835806** | 628 | 74.6 | 30 | 0.73 | 1.51 | 0.8 | 0.97 | 20.6 | 3.15 | <5 | 4.7 |
| **D835807** | 400 | 46.4 | 50 | 0.43 | 1.56 | 0.73 | 0.73 | 18 | 2.7 | <5 | 3.7 |
| **D835808** | 542 | 38.7 | 30 | 0.52 | 1.18 | 0.62 | 0.73 | 21.6 | 1.99 | <5 | 4.4 |
| **D835809** | 440 | 42.8 | 40 | 1.06 | 1.68 | 0.87 | 0.68 | 17 | 2.17 | <5 | 5.4 |
| **D835810** | 387 | 61.1 | 80 | 0.59 | 11.9 | 7.73 | 1.29 | 15.8 | 10.25 | <5 | 7.5 |
| **D835811** | 25.9 | 1 | 10 | 0.02 | 0.22 | 0.12 | 0.04 | 0.3 | 0.22 | <5 | <0.1 |
| **D835812** | 8.3 | 1 | 60 | 0.04 | 0.05 | 0.03 | 0.02 | 0.5 | 0.09 | <5 | 0.1 |

**Table C3:** Continued.

| **Analyte** | **Ho** | **La** | **Lu** | **Nb** | **Nd** | **Pr** | **Rb** | **Sm** | **Sn** | **Sr** | **Ta** |
|---|---|---|---|---|---|---|---|---|---|---|---|
| **Unit** | ppm | ppm | ppm | ppm | ppm | ppm | ppm | ppm | ppm | ppm | ppm |
| **LDL** | 0.01 | 0.5 | 0.01 | 0.2 | 0.1 | 0.03 | 0.2 | 0.03 | 1 | 0.1 | 0.1 |
| **Method** | FUS-MS | FUS-MS | FUS-MS | FUS-MS | FUS-MS | FUS-MS | FUS-MS | FUS-MS | FUS-MS | FUS-MS | FUS-MS |
| **D835751** | 0.66 | 33.5 | 0.29 | 11.6 | 31.3 | 8.85 | 65.8 | 6.13 | 2 | 146.5 | 0.7 |
| **D835752** | 0.19 | 44.5 | 0.1 | 6.1 | 26 | 8.29 | 39 | 3.09 | 1 | 393 | 0.5 |
| **D835753** | 0.18 | 19.3 | 0.07 | 5.5 | 13.7 | 4.07 | 75.4 | 2.86 | 1 | 80.2 | 0.4 |
| **D835754** | 0.47 | 19.7 | 0.21 | 6.7 | 14.5 | 4.4 | 106 | 3.3 | 1 | 119 | 1.1 |
| **D835755** | 0.58 | 19.9 | 0.23 | 5.6 | 21.6 | 5.61 | 68.1 | 4.6 | 1 | 162.5 | 0.4 |
| **D835756** | 0.18 | 6.8 | 0.07 | 3.4 | 5 | 1.59 | 44.9 | 1.14 | 1 | 44.4 | 0.3 |
| **D835757** | 0.06 | 4.4 | 0.03 | 0.2 | 1.8 | 0.44 | 0.4 | 0.37 | <1 | 75.9 | <0.1 |
| **D835758** | 0.2 | 15.7 | 0.1 | 5 | 9.6 | 3.1 | 46.3 | 1.9 | 1 | 87 | 0.6 |
| **D835759** | 0.64 | 16.2 | 0.25 | 10 | 14.9 | 4.26 | 82.1 | 3.39 | 2 | 99.3 | 0.7 |
| **D835760** | 0.55 | 22.1 | 0.23 | 8.3 | 16 | 4.72 | 94.9 | 3.52 | 1 | 107 | 0.7 |
| **D835761** | 0.61 | 9.2 | 0.24 | 2.3 | 10.7 | 2.53 | 12.6 | 3.19 | 1 | 107.5 | 0.2 |
| **D835762** | 0.59 | 34.4 | 0.25 | 10.3 | 22.8 | 7.1 | 55.9 | 4.46 | 2 | 166 | 0.8 |
| **D835763** | 0.46 | 11.5 | 0.24 | 9.2 | 11.4 | 2.79 | 43.7 | 2.99 | 1 | 186.5 | 1 |
| **D835764** | 0.88 | 31.9 | 0.36 | 15.1 | 34.2 | 8.74 | 71.3 | 6.67 | 2 | 159.5 | 0.9 |
| **D835765** | 0.55 | 57.3 | 0.17 | 7.8 | 48.9 | 13.7 | 71 | 8.62 | 1 | 119.5 | 0.4 |
| **D835766** | 1.03 | 37.6 | 0.38 | 18.7 | 39.8 | 10.35 | 89.3 | 7.27 | 1 | 155 | 0.9 |
| **D835767** | 0.2 | 26 | 0.09 | 6.8 | 17.7 | 5.11 | 66.6 | 2.71 | 1 | 108 | 0.6 |
| **D835768** | 0.07 | 4.8 | 0.04 | 0.5 | 3.2 | 0.91 | 16.2 | 0.64 | <1 | 23.2 | <0.1 |
| **D835769** | 0.66 | 25 | 0.25 | 12.1 | 27.6 | 6.97 | 32.7 | 5.36 | 2 | 238 | 0.8 |
| **D835770** | 2.51 | 27.6 | 1.21 | 11.3 | 36.9 | 8.35 | 53.7 | 9.24 | 3 | 73.9 | 0.9 |
| **D835771** | 0.05 | 1.2 | 0.02 | 0.1 | 0.8 | 0.16 | 0.3 | 0.18 | <1 | 84.6 | <0.1 |
| **D835772** | 0.92 | 12.9 | 0.44 | 11 | 11.2 | 3.03 | 65.8 | 2.7 | 2 | 104 | 1.5 |
| **D835773** | 0.22 | 5.1 | 0.12 | 2.8 | 4.6 | 1.22 | 11.4 | 1 | <1 | 270 | 0.3 |
| **D835774** | 0.55 | 10.1 | 0.22 | 5.2 | 15 | 3.35 | 106.5 | 3.21 | 1 | 134.5 | 0.4 |
| **D835775** | 0.31 | 22.6 | 0.16 | 7.8 | 14.6 | 4.29 | 150 | 2.32 | 1 | 82.7 | 1 |
| **D835776** | 0.31 | 15.3 | 0.13 | 7.6 | 12.4 | 3.68 | 94 | 2.62 | 1 | 92.1 | 0.6 |
| **D835777** | 0.12 | 15.1 | 0.07 | 3.2 | 10.8 | 3.12 | 22.2 | 1.76 | <1 | 43.8 | 0.1 |
| **D835778** | 0.11 | 2.1 | 0.04 | 1.8 | 1.9 | 0.46 | 8.3 | 0.37 | <1 | 28.5 | 0.2 |
| **D835779** | 0.3 | 6 | 0.17 | 7.7 | 5.2 | 1.27 | 51 | 1.18 | 1 | 117.5 | 1.1 |
| **D835780** | 0.61 | 18.7 | 0.21 | 9.1 | 19.3 | 4.76 | 77 | 4.18 | 1 | 171.5 | 0.7 |
| **D835781** | 0.47 | 36.6 | 0.28 | 13.5 | 27.4 | 8.04 | 14.6 | 3.99 | 2 | 334 | 1.2 |
| **D835782** | 0.19 | 26.6 | 0.1 | 6.8 | 13.1 | 4.24 | 59.2 | 1.88 | 1 | 133 | 0.8 |
| **D835783** | 0.19 | 57.1 | 0.09 | 9 | 25.6 | 8.69 | 89.9 | 3.12 | 2 | 55.4 | 0.6 |
| **D835784** | 0.28 | 20.9 | 0.12 | 8 | 16.8 | 4.53 | 17.2 | 2.96 | 1 | 250 | 0.9 |
| **D835785** | 0.41 | 36.9 | 0.17 | 10.3 | 23.7 | 6.82 | 39.4 | 3.96 | 1 | 259 | 0.8 |
| **D835786** | 0.28 | 42.5 | 0.11 | 13.1 | 37.7 | 10.15 | 96.4 | 6.72 | 2 | 135.5 | 0.7 |
| **D835787** | 0.43 | 34.2 | 0.13 | 7.5 | 28.4 | 7.8 | 59.6 | 4.88 | 1 | 116.5 | 0.4 |
| **D835788** | 0.57 | 19.7 | 0.22 | 11.4 | 15.6 | 4.25 | 40.9 | 3.01 | 1 | 253 | 1.1 |
| **D835789** | 0.57 | 33.1 | 0.3 | 7.7 | 22 | 6.35 | 73.3 | 3.79 | 1 | 155 | 0.8 |
| **D835790** | 0.86 | 9.9 | 0.34 | 5 | 13.3 | 2.98 | 13.1 | 3.7 | 1 | 176.5 | 0.3 |
| **D835791** | 0.05 | 1.3 | 0.01 | 0.1 | 1 | 0.25 | 0.3 | 0.16 | <1 | 83.3 | <0.1 |
| **D835792** | 0.24 | 23.5 | 0.11 | 2.8 | 17.1 | 4.87 | 55.3 | 3.04 | <1 | 115 | 0.3 |
| **D835793** | 0.6 | 22.8 | 0.17 | 10.2 | 18.3 | 4.95 | 53.3 | 3.71 | 1 | 171 | 0.9 |
| **D835794** | 0.41 | 20.4 | 0.15 | 6.3 | 16.3 | 4.27 | 90 | 2.92 | 1 | 86.8 | 0.5 |
| **D835795** | 0.26 | 27.6 | 0.1 | 6.7 | 19.9 | 5.52 | 68.6 | 3.51 | 1 | 126.5 | 0.4 |
| **D835796** | 0.49 | 33.5 | 0.2 | 7.5 | 25.7 | 6.89 | 33.4 | 4.19 | 1 | 206 | 0.4 |
| **D835797** | 0.38 | 27.5 | 0.16 | 6.4 | 20.3 | 5.46 | 65.8 | 3.33 | 1 | 127.5 | 0.3 |
| **D835798** | 0.37 | 5.2 | 0.14 | 4.3 | 9.3 | 2 | 0.2 | 2.53 | 1 | 385 | 0.3 |
| **D835799** | 0.38 | 17.1 | 0.18 | 7.1 | 14.2 | 3.84 | 72.1 | 2.7 | 2 | 109 | 0.7 |
| **D835800** | 0.4 | 35.3 | 0.16 | 4.6 | 25.3 | 7.27 | 48.1 | 4.11 | 1 | 175 | 0.2 |
| **D835801** | 0.55 | 14.6 | 0.2 | 9.9 | 14.1 | 3.64 | 71.6 | 2.93 | 3 | 283 | 0.6 |
| **D835802** | 0.33 | 22.3 | 0.13 | 6.6 | 20.8 | 5.44 | 77.7 | 3.59 | 1 | 127.5 | 0.6 |
| **D835803** | 0.12 | 8.7 | 0.06 | 3.8 | 6 | 1.57 | 35 | 1.26 | 1 | 187 | 0.2 |
| **D835804** | 0.37 | 22 | 0.15 | 6.5 | 17.9 | 4.83 | 36.6 | 3.14 | 1 | 187.5 | 0.4 |
| **D835805** | 0.58 | 100.5 | 0.24 | 12.8 | 60.5 | 18.1 | 29.6 | 8.87 | 1 | 223 | 0.4 |
| **D835806** | 0.25 | 39.9 | 0.1 | 9.1 | 29.4 | 8.16 | 67 | 4.28 | 1 | 106.5 | 0.4 |
| **D835807** | 0.27 | 24.4 | 0.12 | 6.3 | 18.6 | 5.2 | 37.9 | 3.52 | 1 | 235 | 0.4 |
| **D835808** | 0.22 | 24 | 0.08 | 8.3 | 16.2 | 4.5 | 52 | 2.68 | 1 | 201 | 0.5 |
| **D835809** | 0.28 | 22.4 | 0.09 | 7.6 | 16.6 | 4.55 | 83.1 | 2.73 | 1 | 68.5 | 0.5 |
| **D835810** | 2.46 | 26.5 | 1.23 | 11.6 | 35.1 | 7.94 | 53.2 | 8.96 | 3 | 73.5 | 0.9 |
| **D835811** | 0.04 | 1.1 | 0.02 | 0.2 | 0.9 | 0.2 | 0.7 | 0.16 | <1 | 82.7 | <0.1 |
| **D835812** | 0.01 | 0.5 | 0.01 | 0.3 | 0.4 | 0.11 | 1.3 | 0.08 | <1 | 4.4 | <0.1 |

**Table C3:** Continued.

| **Analyte** | **Tb** | **Th** | **Tm** | **U** | **V** | **W** | **Y** | **Yb** | **Zr** | **Cd** | **Co** |
|---|---|---|---|---|---|---|---|---|---|---|---|
| **Unit** | ppm | ppm | ppm | ppm | ppm | ppm | ppm | ppm | ppm | ppm | ppm |
| **LDL** | 0.01 | 0.05 | 0.01 | 0.05 | 5 | 1 | 0.5 | 0.03 | 2 | 0.5 | 1 |
| **Method** | FUS-MS | FUS-MS | FUS-MS | FUS-MS | FUS-MS | FUS-MS | FUS-MS | FUS-MS | FUS-MS | TD-ICP | TD-ICP |
| **D835751** | 0.62 | 5.06 | 0.26 | 0.94 | 72 | 5 | 18.6 | 1.7 | 244 | <0.5 | 9 |
| **D835752** | 0.23 | 7.95 | 0.08 | 0.6 | 70 | 1 | 5.9 | 0.54 | 192 | <0.5 | 11 |
| **D835753** | 0.26 | 6.7 | 0.09 | 0.59 | 15 | 1 | 5.8 | 0.53 | 97 | <0.5 | 2 |
| **D835754** | 0.39 | 4.05 | 0.19 | 1.4 | 84 | 5 | 13.9 | 1.34 | 148 | <0.5 | 13 |
| **D835755** | 0.51 | 1.54 | 0.28 | 0.68 | 74 | 3 | 17.3 | 1.58 | 204 | <0.5 | 14 |
| **D835756** | 0.14 | 0.91 | 0.06 | 0.35 | 54 | 20 | 5 | 0.44 | 60 | <0.5 | 8 |
| **D835757** | 0.05 | 0.1 | 0.05 | 0.13 | 108 | 1 | 3 | 0.1 | 2 | <0.5 | <1 |
| **D835758** | 0.22 | 4.66 | 0.1 | 1.86 | 21 | 2 | 5.8 | 0.53 | 72 | <0.5 | 3 |
| **D835759** | 0.53 | 2.04 | 0.27 | 1.03 | 96 | 9 | 18.9 | 1.54 | 166 | <0.5 | 17 |
| **D835760** | 0.46 | 3.2 | 0.25 | 1.22 | 76 | 10 | 16.1 | 1.54 | 161 | <0.5 | 13 |
| **D835761** | 0.52 | 1.68 | 0.27 | 0.54 | 193 | 2 | 16.7 | 1.55 | 61 | <0.5 | 45 |
| **D835762** | 0.51 | 7.51 | 0.24 | 1.53 | 35 | 1 | 17.4 | 1.63 | 250 | <0.5 | 7 |
| **D835763** | 0.38 | 7.16 | 0.23 | 2.5 | 7 | 1 | 14.1 | 1.53 | 74 | <0.5 | 1 |
| **D835764** | 0.85 | 2.29 | 0.34 | 0.55 | 66 | 5 | 24.5 | 2.16 | 280 | <0.5 | 11 |
| **D835765** | 0.76 | 11.8 | 0.18 | 1.1 | 42 | 8 | 14.9 | 1.11 | 304 | <0.5 | 5 |
| **D835766** | 0.9 | 3.35 | 0.38 | 0.73 | 82 | 11 | 28.4 | 2.5 | 380 | <0.5 | 15 |
| **D835767** | 0.2 | 6.42 | 0.08 | 2.29 | 52 | 5 | 5.5 | 0.49 | 137 | <0.5 | 9 |
| **D835768** | 0.07 | 2.21 | 0.04 | 0.72 | 12 | 1 | 2.4 | 0.2 | 24 | <0.5 | 1 |
| **D835769** | 0.61 | 3.91 | 0.25 | 1.25 | 96 | 1 | 19.3 | 1.67 | 202 | <0.5 | 16 |
| **D835770** | 1.73 | 4.95 | 1.17 | 1.3 | 12 | 1 | 72.1 | 7.78 | 263 | <0.5 | 3 |
| **D835771** | 0.02 | <0.05 | 0.02 | 0.08 | <5 | <1 | 1.9 | 0.1 | <2 | <0.5 | <1 |
| **D835772** | 0.63 | 6.97 | 0.44 | 5.04 | 7 | 1 | 29.2 | 2.92 | 86 | <0.5 | 2 |
| **D835773** | 0.15 | 4.19 | 0.1 | 3.32 | 7 | 1 | 6.6 | 0.69 | 65 | <0.5 | <1 |
| **D835774** | 0.49 | 1.69 | 0.23 | 1.3 | 88 | 3 | 16.5 | 1.55 | 196 | <0.5 | 16 |
| **D835775** | 0.25 | 10.05 | 0.14 | 2.88 | 22 | 1 | 8.7 | 0.87 | 124 | <0.5 | 2 |
| **D835776** | 0.26 | 7.61 | 0.14 | 2.01 | <5 | 1 | 9.7 | 0.85 | 43 | <0.5 | 1 |
| **D835777** | 0.16 | 3.53 | 0.06 | 0.5 | 18 | 2 | 3.5 | 0.32 | 76 | <0.5 | 2 |
| **D835778** | 0.06 | 0.52 | 0.04 | 0.59 | 10 | 1 | 3.3 | 0.29 | 17 | <0.5 | 2 |
| **D835779** | 0.23 | 2.36 | 0.17 | 1.59 | 15 | 2 | 11 | 1.07 | 65 | <0.5 | 2 |
| **D835780** | 0.58 | 4.08 | 0.28 | 0.91 | 60 | 1 | 17.8 | 1.53 | 223 | <0.5 | 11 |
| **D835781** | 0.39 | 10.25 | 0.25 | 1.75 | 24 | <1 | 15.2 | 1.74 | 280 | <0.5 | 4 |
| **D835782** | 0.16 | 3.83 | 0.09 | 0.92 | 18 | 1 | 5.6 | 0.59 | 77 | <0.5 | 2 |
| **D835783** | 0.23 | 7.79 | 0.09 | 0.87 | 38 | 2 | 6.1 | 0.62 | 116 | <0.5 | 4 |
| **D835784** | 0.28 | 4.8 | 0.11 | 1.66 | 17 | 1 | 8.6 | 0.68 | 138 | <0.5 | 3 |
| **D835785** | 0.34 | 8.4 | 0.15 | 1.48 | 36 | 1 | 11.9 | 0.96 | 201 | <0.5 | 6 |
| **D835786** | 0.44 | 8.47 | 0.1 | 1.37 | 97 | 24 | 7.5 | 0.62 | 278 | <0.5 | 8 |
| **D835787** | 0.49 | 8.83 | 0.17 | 1.21 | 29 | 3 | 11.8 | 0.93 | 149 | <0.5 | 6 |
| **D835788** | 0.47 | 3.13 | 0.25 | 0.83 | 39 | 1 | 17.6 | 1.54 | 233 | <0.5 | 6 |
| **D835789** | 0.43 | 9.65 | 0.26 | 2.55 | 27 | 2 | 17 | 1.59 | 180 | <0.5 | 5 |
| **D835790** | 0.64 | 2 | 0.35 | 0.48 | 312 | <1 | 23 | 2.15 | 90 | <0.5 | 58 |
| **D835791** | 0.03 | 0.15 | 0.02 | 0.1 | <5 | <1 | 2.2 | 0.12 | 2 | <0.5 | <1 |
| **D835792** | 0.27 | 6.43 | 0.09 | 1.53 | 12 | 2 | 7.4 | 0.64 | 95 | <0.5 | 2 |
| **D835793** | 0.56 | 6.09 | 0.19 | 0.82 | 30 | 2 | 15.5 | 0.88 | 187 | <0.5 | 5 |
| **D835794** | 0.36 | 4.36 | 0.15 | 0.83 | 77 | 7 | 11.8 | 0.93 | 121 | <0.5 | 9 |
| **D835795** | 0.29 | 8.43 | 0.11 | 0.81 | 26 | 3 | 7.5 | 0.58 | 167 | <0.5 | 5 |
| **D835796** | 0.46 | 5.96 | 0.2 | 0.62 | 43 | <1 | 13.7 | 1.16 | 245 | <0.5 | 9 |
| **D835797** | 0.39 | 5.07 | 0.14 | 0.76 | 61 | 4 | 11.1 | 1.02 | 224 | <0.5 | 9 |
| **D835798** | 0.38 | 0.38 | 0.15 | 0.52 | 123 | 7 | 11.8 | 0.92 | 45 | 0.9 | 57 |
| **D835799** | 0.36 | 3.83 | 0.18 | 0.93 | 56 | 5 | 11.8 | 1.22 | 134 | <0.5 | 7 |
| **D835800** | 0.49 | 11.45 | 0.13 | 1.46 | 16 | 2 | 11.2 | 0.93 | 171 | <0.5 | 3 |
| **D835801** | 0.54 | 2.02 | 0.24 | 0.7 | 66 | 3 | 17.6 | 1.43 | 147 | <0.5 | 9 |
| **D835802** | 0.34 | 4.82 | 0.13 | 0.61 | 61 | 23 | 9.6 | 0.79 | 103 | <0.5 | 12 |
| **D835803** | 0.14 | 3.78 | 0.04 | 1.15 | 13 | 1 | 3.9 | 0.29 | 81 | <0.5 | 2 |
| **D835804** | 0.37 | 5.11 | 0.14 | 0.93 | 70 | 3 | 10.7 | 0.96 | 139 | <0.5 | 12 |
| **D835805** | 0.73 | 29.9 | 0.22 | 2.44 | 20 | <1 | 16 | 1.48 | 288 | <0.5 | 5 |
| **D835806** | 0.36 | 9.33 | 0.09 | 0.93 | 42 | 6 | 7.8 | 0.7 | 207 | <0.5 | 4 |
| **D835807** | 0.32 | 8.76 | 0.09 | 0.77 | 17 | <1 | 7.6 | 0.71 | 127 | <0.5 | 4 |
| **D835808** | 0.23 | 6.4 | 0.08 | 0.73 | 44 | 1 | 6.7 | 0.52 | 206 | <0.5 | 9 |
| **D835809** | 0.28 | 2.31 | 0.1 | 0.46 | 34 | 3 | 8.6 | 0.67 | 234 | <0.5 | 6 |
| **D835810** | 1.79 | 4.91 | 1.18 | 1.23 | 15 | 2 | 73 | 7.68 | 259 | <0.5 | 3 |
| **D835811** | 0.03 | 0.07 | 0.02 | 0.16 | <5 | <1 | 2.2 | 0.11 | 2 | <0.5 | 1 |
| **D835812** | 0.01 | 0.16 | <0.01 | 0.12 | 5 | 1 | 0.4 | 0.03 | 3 | <0.5 | <1 |

**Table C3:** Continued.

| **Analyte** | **Cu** | **Li** | **Mo** | **Ni** | **Pb** | **Sc** | **Zn** | **As** | **Bi** | **Hg** | **In** |
|---|---|---|---|---|---|---|---|---|---|---|---|
| **Unit** | ppm | ppm | ppm | ppm | ppm | ppm | ppm | ppm | ppm | ppm | ppm |
| **LDL** | 1 | 10 | 1 | 1 | 2 | 1 | 2 | 0.1 | 0.5 | 0.005 | 0.005 |
| **Method** | TD-ICP | TD-ICP | TD-ICP | TD-ICP | TD-ICP | TD-ICP | TD-ICP | AR-MS | AR-MS | AR-MS | AR-MS |
| **D835751** | 24 | 20 | 1 | 3 | 6 | 8 | 96 | 0.4 | 0.03 | <0.005 | 0.007 |
| **D835752** | 49 | 20 | 1 | 11 | 14 | 5 | 78 | 0.4 | 0.01 | <0.005 | <0.005 |
| **D835753** | 8 | <10 | 4 | 3 | 7 | 2 | 31 | 0.4 | 0.15 | <0.005 | <0.005 |
| **D835754** | 33 | <10 | 2 | 13 | 29 | 8 | 57 | 0.5 | 1.81 | 0.006 | <0.005 |
| **D835755** | 11 | 20 | 2 | 35 | 5 | 9 | 115 | 0.1 | 0.04 | <0.005 | 0.006 |
| **D835756** | 3 | <10 | 69 | 12 | 63 | 4 | 111 | 0.7 | 1.88 | 0.052 | <0.005 |
| **D835757** | 1 | <10 | <1 | <1 | 2 | <1 | 3 | 0.2 | 0.01 | <0.005 | <0.005 |
| **D835758** | 11 | <10 | 3 | 4 | 6 | 3 | 19 | 0.1 | 0.03 | <0.005 | <0.005 |
| **D835759** | 12 | 10 | 1 | 24 | 9 | 11 | 118 | 0.5 | 0.2 | <0.005 | 0.007 |
| **D835760** | 104 | <10 | 1 | 19 | 5 | 9 | 65 | 0.2 | 0.14 | <0.005 | 0.005 |
| **D835761** | 52 | 100 | 1 | 173 | 3 | 20 | 145 | 0.5 | 0.04 | <0.005 | 0.037 |
| **D835762** | 6 | 10 | 2 | 7 | 7 | 6 | 72 | 0.7 | 0.01 | <0.005 | 0.007 |
| **D835763** | 6 | <10 | 2 | 2 | 6 | 2 | 19 | <0.1 | 0.02 | 0.006 | <0.005 |
| **D835764** | 57 | 20 | 1 | 9 | 5 | 8 | 93 | 0.3 | 0.04 | <0.005 | 0.011 |
| **D835765** | 31 | <10 | 2 | 4 | 7 | 3 | 56 | 0.2 | 0.18 | 0.006 | <0.005 |
| **D835766** | 9 | 30 | 1 | 14 | 4 | 10 | 110 | 1.4 | 0.18 | 0.005 | 0.01 |
| **D835767** | 12 | 10 | 3 | 34 | 76 | 4 | 26 | 32.4 | 0.02 | <0.005 | 0.006 |
| **D835768** | 103 | <10 | 6 | 4 | 42 | <1 | 8 | 0.3 | 1.03 | <0.005 | <0.005 |
| **D835769** | 7 | 30 | 1 | 43 | 5 | 10 | 96 | 2.1 | 0.02 | <0.005 | 0.007 |
| **D835770** | 11 | 10 | 4 | 4 | 5 | 7 | 54 | 0.6 | 0.06 | <0.005 | 0.024 |
| **D835771** | <1 | <10 | <1 | <1 | 4 | <1 | 2 | <0.1 | 0.01 | <0.005 | <0.005 |
| **D835772** | 3 | <10 | 2 | 3 | 14 | 3 | 30 | 0.9 | 0.01 | <0.005 | <0.005 |
| **D835773** | 1 | 20 | 2 | 1 | 4 | 1 | <2 | 0.1 | 0.01 | <0.005 | <0.005 |
| **D835774** | 61 | 10 | 1 | 24 | 3 | 9 | 72 | 1.6 | 0.04 | <0.005 | 0.005 |
| **D835775** | 9 | <10 | 1 | 2 | 4 | 3 | 33 | 3.1 | 0.03 | <0.005 | <0.005 |
| **D835776** | 2 | <10 | 1 | 2 | 5 | 2 | 17 | 0.4 | 0.04 | <0.005 | <0.005 |
| **D835777** | 2 | <10 | 3 | 8 | 2 | 1 | 17 | <0.1 | 0.02 | <0.005 | <0.005 |
| **D835778** | 882 | <10 | 4 | 7 | 2290 | 1 | 12 | 0.6 | 63.8 | 0.019 | 0.006 |
| **D835779** | 4 | <10 | 2 | 2 | 13 | 2 | 23 | 0.4 | 0.32 | <0.005 | <0.005 |
| **D835780** | 16 | 20 | 1 | 14 | 6 | 9 | 79 | <0.1 | 0.04 | <0.005 | 0.011 |
| **D835781** | 4 | 20 | 2 | 3 | 8 | 4 | 17 | 0.2 | 0.02 | <0.005 | 0.007 |
| **D835782** | 7 | <10 | 1 | 2 | 10 | 2 | 32 | 0.3 | 0.02 | <0.005 | <0.005 |
| **D835783** | 5 | <10 | 2 | 4 | 7 | 2 | 42 | 0.4 | 0.13 | <0.005 | <0.005 |
| **D835784** | 1 | 20 | 2 | 3 | 5 | 3 | 14 | 0.3 | 0.02 | <0.005 | 0.005 |
| **D835785** | 5 | 20 | 1 | 7 | 8 | 6 | 36 | 0.8 | 0.02 | <0.005 | 0.012 |
| **D835786** | 5 | 10 | 8 | 51 | 4 | 8 | 60 | 13.8 | 0.07 | <0.005 | 0.006 |
| **D835787** | 6 | 10 | 2 | 4 | 4 | 3 | 41 | 0.4 | 0.01 | <0.005 | <0.005 |
| **D835788** | 2 | 10 | 1 | 3 | 6 | 4 | 75 | 0.8 | 0.04 | <0.005 | <0.005 |
| **D835789** | 2 | <10 | 2 | 6 | 8 | 4 | 53 | 0.4 | 0.01 | <0.005 | 0.005 |
| **D835790** | 178 | 10 | 1 | 157 | 3 | 31 | 109 | 0.7 | 0.02 | <0.005 | 0.016 |
| **D835791** | <1 | <10 | <1 | <1 | 2 | <1 | 3 | 0.3 | <0.01 | <0.005 | <0.005 |
| **D835792** | 2 | <10 | 2 | 3 | 5 | 1 | 17 | 0.2 | <0.01 | <0.005 | <0.005 |
| **D835793** | 3 | 10 | 1 | 2 | 6 | 6 | 59 | 0.3 | 0.01 | <0.005 | 0.005 |
| **D835794** | 3 | <10 | 1 | 32 | 5 | 8 | 48 | 1.3 | 0.13 | <0.005 | <0.005 |
| **D835795** | 1 | <10 | 2 | 5 | 4 | 3 | 41 | 0.2 | <0.01 | <0.005 | <0.005 |
| **D835796** | 5 | 10 | 2 | 10 | 6 | 6 | 81 | 2.2 | 0.01 | <0.005 | 0.005 |
| **D835797** | 12 | 10 | 1 | 17 | 5 | 6 | 43 | 0.8 | 0.04 | <0.005 | 0.005 |
| **D835798** | 105 | 30 | 3 | 612 | 6 | 20 | 155 | 17.1 | 0.07 | 0.005 | 0.044 |
| **D835799** | 21 | <10 | 1 | 10 | 2 | 6 | 50 | 3.7 | 0.01 | <0.005 | 0.005 |
| **D835800** | 21 | 10 | 1 | 3 | 6 | 2 | 42 | 0.3 | 0.01 | <0.005 | <0.005 |
| **D835801** | 24 | 10 | 1 | 14 | 6 | 9 | 63 | 5.5 | 0.13 | <0.005 | 0.016 |
| **D835802** | 5 | 10 | 6 | 15 | 30 | 7 | 32 | 1.4 | 4.2 | <0.005 | <0.005 |
| **D835803** | 2 | <10 | 2 | 4 | 5 | 2 | 22 | 0.2 | 0.04 | <0.005 | <0.005 |
| **D835804** | 2 | 20 | 1 | 40 | 3 | 9 | 66 | 0.4 | 0.03 | <0.005 | 0.008 |
| **D835805** | 2 | 10 | 2 | 5 | 9 | 4 | 57 | 0.6 | <0.01 | <0.005 | 0.007 |
| **D835806** | 3 | <10 | 2 | 7 | 3 | 4 | 28 | 1.2 | 0.01 | <0.005 | <0.005 |
| **D835807** | 2 | 20 | 3 | 2 | 5 | 2 | 30 | 0.1 | 0.01 | <0.005 | <0.005 |
| **D835808** | 2 | 40 | 1 | 9 | 4 | 4 | 56 | 0.2 | 0.01 | <0.005 | <0.005 |
| **D835809** | 5 | <10 | 2 | 4 | 19 | 3 | 179 | 7.5 | 0.04 | 0.019 | 0.008 |
| **D835810** | 12 | 10 | 5 | 5 | 5 | 7 | 57 | 0.6 | 0.05 | <0.005 | 0.021 |
| **D835811** | 1 | <10 | <1 | <1 | 2 | <1 | 5 | 1.2 | 0.01 | <0.005 | <0.005 |
| **D835812** | 18 | <10 | 4 | 1 | 8 | <1 | 4 | 0.5 | 0.01 | 0.011 | <0.005 |

**Table C3:** Continued.

| **Analyte** | **Re** | **Sb** | **Se** | **Te** | **Tl** | **C** | **S** | **H2O+** | **Cl** | **F** | **S.G.** |
|---|---|---|---|---|---|---|---|---|---|---|---|
| **Unit** | ppm | ppm | ppm | ppm | ppm | wt. % | wt. % | wt. % | ppm | ppm | |
| **LDL** | 0.001 | 0.05 | 0.2 | 0.01 | 0.02 | 0.01 | 0.01 | 0.01 | 50 | 20 | |
| **Method** | AR-MS | AR-MS | AR-MS | AR-MS | AR-MS | LECO | LECO | COM-IRS | KOH | KOH | |
| **D835751** | <0.001 | 0.05 | <0.2 | 0.02 | 0.03 | 0.41 | 0.06 | 1.93 | 90 | 470 | 2.83 |
| **D835752** | <0.001 | 0.07 | <0.2 | <0.01 | 0.02 | 0.08 | 0.02 | 1.78 | 120 | 410 | 2.79 |
| **D835753** | <0.001 | <0.05 | <0.2 | 0.12 | 0.03 | 0.22 | 0.05 | 1.52 | 90 | 290 | 2.79 |
| **D835754** | <0.001 | <0.05 | 0.2 | 2.33 | 0.04 | 1.73 | 0.5 | 1.82 | 90 | 430 | 2.81 |
| **D835755** | <0.001 | <0.05 | <0.2 | 0.01 | 0.02 | 1.32 | <0.01 | 0.34 | 130 | 390 | 2.81 |
| **D835756** | 0.002 | <0.05 | 0.5 | 3.37 | 0.02 | 0.7 | 1.49 | 1.13 | 80 | 210 | 2.8 |
| **D835757** | <0.001 | <0.05 | 0.3 | 0.01 | <0.02 | 10.5 | <0.01 | 0.22 | 130 | 140 | 2.78 |
| **D835758** | <0.001 | <0.05 | <0.2 | 0.03 | 0.02 | 0.57 | 0.06 | 0.87 | 90 | 200 | 2.82 |
| **D835759** | <0.001 | <0.05 | 0.2 | 0.09 | 0.03 | 1.75 | 0.32 | 2.09 | 70 | 410 | 2.84 |
| **D835760** | 0.001 | <0.05 | <0.2 | 0.31 | 0.04 | 1.57 | 0.25 | 1.66 | 110 | 510 | 2.81 |
| **D835761** | 0.001 | <0.05 | 0.2 | 0.02 | <0.02 | 2.3 | 0.04 | 3.88 | 130 | 290 | 2.79 |
| **D835762** | <0.001 | 0.14 | <0.2 | <0.01 | 0.03 | 0.22 | <0.01 | 1.25 | 90 | 360 | 2.77 |
| **D835763** | <0.001 | <0.05 | <0.2 | <0.01 | 0.02 | 0.4 | <0.01 | 0.83 | 100 | 200 | 2.82 |
| **D835764** | <0.001 | <0.05 | 0.2 | 0.01 | 0.03 | 0.78 | 0.13 | 2.29 | 80 | 510 | 2.83 |
| **D835765** | <0.001 | <0.05 | <0.2 | 0.41 | 0.03 | 0.8 | 0.59 | 1.34 | 90 | 380 | 2.79 |
| **D835766** | <0.001 | 0.05 | 0.4 | 0.38 | 0.04 | 1.13 | 1.26 | 2.72 | 70 | 760 | 2.82 |
| **D835767** | <0.001 | 0.05 | 0.5 | <0.01 | 0.02 | 1.08 | 0.03 | 1.55 | 110 | 380 | 2.83 |
| **D835768** | <0.001 | <0.05 | <0.2 | 0.2 | <0.02 | 0.04 | 0.04 | 0.86 | 90 | 110 | 2.8 |
| **D835769** | <0.001 | 0.07 | <0.2 | <0.01 | 0.02 | 0.11 | 0.01 | 2.31 | 80 | 480 | 2.81 |
| **D835770** | 0.001 | 0.12 | <0.2 | <0.01 | 0.02 | 0.04 | <0.01 | 1.12 | 100 | 300 | 2.82 |
| **D835771** | <0.001 | <0.05 | 0.2 | <0.01 | <0.02 | 10.9 | <0.01 | 0.23 | 150 | 100 | 2.82 |
| **D835772** | <0.001 | 0.05 | <0.2 | <0.01 | 0.03 | 0.23 | 0.01 | 0.81 | 120 | 150 | 2.81 |
| **D835773** | <0.001 | <0.05 | <0.2 | <0.01 | <0.02 | 0.51 | <0.01 | 1.27 | 100 | 110 | 2.82 |
| **D835774** | <0.001 | <0.05 | 0.2 | 0.02 | 0.05 | 1.9 | 0.43 | 2.1 | 70 | 630 | 2.79 |
| **D835775** | <0.001 | 0.07 | <0.2 | <0.01 | 0.06 | 0.24 | 0.01 | 1.43 | 100 | 320 | 2.79 |
| **D835776** | <0.001 | <0.05 | <0.2 | 0.01 | 0.03 | 0.1 | 0.06 | 0.5 | 130 | 170 | 2.95 |
| **D835777** | <0.001 | <0.05 | <0.2 | 0.02 | 0.02 | 0.05 | 0.02 | 0.46 | 80 | 130 | 2.81 |
| **D835778** | <0.001 | <0.05 | 2.9 | 22.2 | <0.02 | 0.29 | 0.16 | 0.29 | 110 | 80 | 2.81 |
| **D835779** | <0.001 | <0.05 | <0.2 | 0.18 | 0.02 | 0.15 | 0.15 | 0.86 | 80 | 240 | 2.82 |
| **D835780** | <0.001 | <0.05 | <0.2 | 0.02 | 0.03 | 0.93 | 0.01 | 2.63 | 80 | 440 | 2.81 |
| **D835781** | <0.001 | 0.07 | <0.2 | <0.01 | <0.02 | 0.04 | 0.01 | 1.3 | 170 | 290 | 2.76 |
| **D835782** | <0.001 | <0.05 | <0.2 | 0.01 | 0.04 | 0.03 | 0.02 | 1.14 | <50 | 310 | 2.8 |
| **D835783** | <0.001 | <0.05 | <0.2 | 0.15 | 0.03 | 0.04 | 0.13 | 1.8 | 310 | 450 | 2.84 |
| **D835784** | <0.001 | <0.05 | <0.2 | <0.01 | <0.02 | 0.46 | 0.01 | 1.16 | 140 | 210 | 2.81 |
| **D835785** | <0.001 | 0.07 | <0.2 | 0.03 | 0.02 | 0.39 | 0.01 | 1.67 | 130 | 300 | 2.78 |
| **D835786** | <0.001 | <0.05 | 0.4 | 0.45 | 0.03 | 1.14 | 0.47 | 1.75 | <50 | 470 | 2.81 |
| **D835787** | <0.001 | <0.05 | <0.2 | 0.01 | 0.02 | 0.78 | 0.08 | 1.19 | 130 | 310 | 2.81 |
| **D835788** | <0.001 | 0.05 | <0.2 | 0.02 | 0.03 | 0.17 | 0.03 | 1.23 | 180 | 330 | 2.82 |
| **D835789** | <0.001 | <0.05 | <0.2 | <0.01 | 0.03 | 1 | 0.01 | 1.09 | <50 | 290 | 2.84 |
| **D835790** | 0.001 | <0.05 | 0.2 | 0.01 | 0.08 | 0.04 | 0.04 | 0.86 | 510 | 220 | 2.91 |
| **D835791** | <0.001 | <0.05 | 0.5 | <0.01 | <0.02 | 10.6 | 0.01 | 0.17 | 140 | 150 | 2.8 |
| **D835792** | <0.001 | <0.05 | <0.2 | 0.01 | 0.02 | 0.39 | 0.03 | 1.11 | <50 | 250 | 2.8 |
| **D835793** | <0.001 | <0.05 | <0.2 | 0.01 | 0.02 | 0.58 | 0.02 | 1.6 | <50 | 310 | 2.81 |
| **D835794** | <0.001 | <0.05 | <0.2 | 0.08 | 0.02 | 1.7 | 0.1 | 1.52 | <50 | 420 | 2.8 |
| **D835795** | <0.001 | <0.05 | <0.2 | <0.01 | 0.02 | 1.02 | 0.02 | 1.02 | 110 | 310 | 2.83 |
| **D835796** | <0.001 | <0.05 | <0.2 | <0.01 | 0.02 | 0.09 | 0.01 | 1.85 | 120 | 300 | 2.82 |
| **D835797** | <0.001 | <0.05 | <0.2 | 0.04 | 0.02 | 1.19 | 0.16 | 1.57 | <50 | 340 | 2.81 |
| **D835798** | <0.001 | <0.05 | 0.6 | 0.3 | <0.02 | 5.78 | 0.22 | 2.55 | 140 | 330 | 2.78 |
| **D835799** | <0.001 | 0.05 | <0.2 | 0.03 | 0.03 | 1.29 | 0.03 | 1.36 | <50 | 350 | 2.81 |
| **D835800** | <0.001 | <0.05 | <0.2 | 0.01 | 0.03 | 0.49 | 0.05 | 1.22 | <50 | 240 | 2.83 |
| **D835801** | <0.001 | <0.05 | <0.2 | 0.01 | 0.03 | 1.99 | 0.03 | 1.69 | 120 | 330 | 2.82 |
| **D835802** | <0.001 | <0.05 | 0.2 | 0.67 | 0.03 | 0.65 | 0.64 | 1.7 | 110 | 500 | 2.85 |
| **D835803** | <0.001 | <0.05 | <0.2 | <0.01 | 0.02 | 0.35 | 0.02 | 0.8 | 170 | 200 | 2.8 |
| **D835804** | <0.001 | <0.05 | <0.2 | 0.01 | 0.02 | 1.43 | 0.02 | 1.27 | 120 | 300 | 2.8 |
| **D835805** | <0.001 | <0.05 | <0.2 | <0.01 | 0.02 | 0.08 | 0.02 | 1.18 | 210 | 250 | 2.8 |
| **D835806** | <0.001 | <0.05 | <0.2 | <0.01 | 0.03 | 0.4 | 0.05 | 1.74 | <50 | 390 | 2.81 |
| **D835807** | <0.001 | <0.05 | <0.2 | <0.01 | 0.02 | 0.4 | 0.02 | 1.43 | <50 | 220 | 2.81 |
| **D835808** | <0.001 | <0.05 | <0.2 | <0.01 | 0.02 | 0.18 | 0.01 | 2.06 | 110 | 300 | 2.81 |
| **D835809** | <0.001 | <0.05 | <0.2 | 0.02 | 0.03 | 0.7 | 0.29 | 1.63 | 120 | 430 | 2.88 |
| **D835810** | 0.001 | 0.13 | <0.2 | <0.01 | 0.02 | 0.03 | 0.02 | 0.97 | 130 | 330 | 2.81 |
| **D835811** | <0.001 | <0.05 | 0.5 | <0.01 | <0.02 | 10.4 | 0.01 | 0.15 | <50 | 170 | 2.81 |
| **D835812** | <0.001 | <0.05 | <0.2 | 0.03 | <0.02 | 0.06 | 0.02 | 0.09 | 250 | <20 | 2.8 |

**Notes***:* PT, Porphyritic tonalite; FGT, Fine grained tonalite; MD, mafic dyke; LCV, laminated crustiform vein; QCC, quartz chlorite sulfide vein; HBV, hydrothermal breccia vein; SRV, sulfide rich veins; Chl-carb (±ser) , chlorite-sericite-carbonate rich alteration; Ser (±carb) , sericite-chlorite-carbonate rich alteration; LOI, loss on ignition; FUS-ICP, lithium metaborate & tetraborate fusion ICP; FUS-MS, lithium metaborate & tetraborate fusion FUS-MS; AR-MS, aqua regia digestion FUS-MS; TD-ICP, total four acid digestion ICP; INAA, instrumental neutron activation analysis; LECO, combustion by LecoTM induction furnace

## Appendix D: Trace element maps

Sample : MEAK20GJF007AG02A

Description : A 0.5 mm cubic pyrite located within the chlorite-carbonate (±sericite) alteration halo of a laminated crustiform vein. The pyrite grain is surrounded by primary quartz and sericitized primary plagioclase grains.

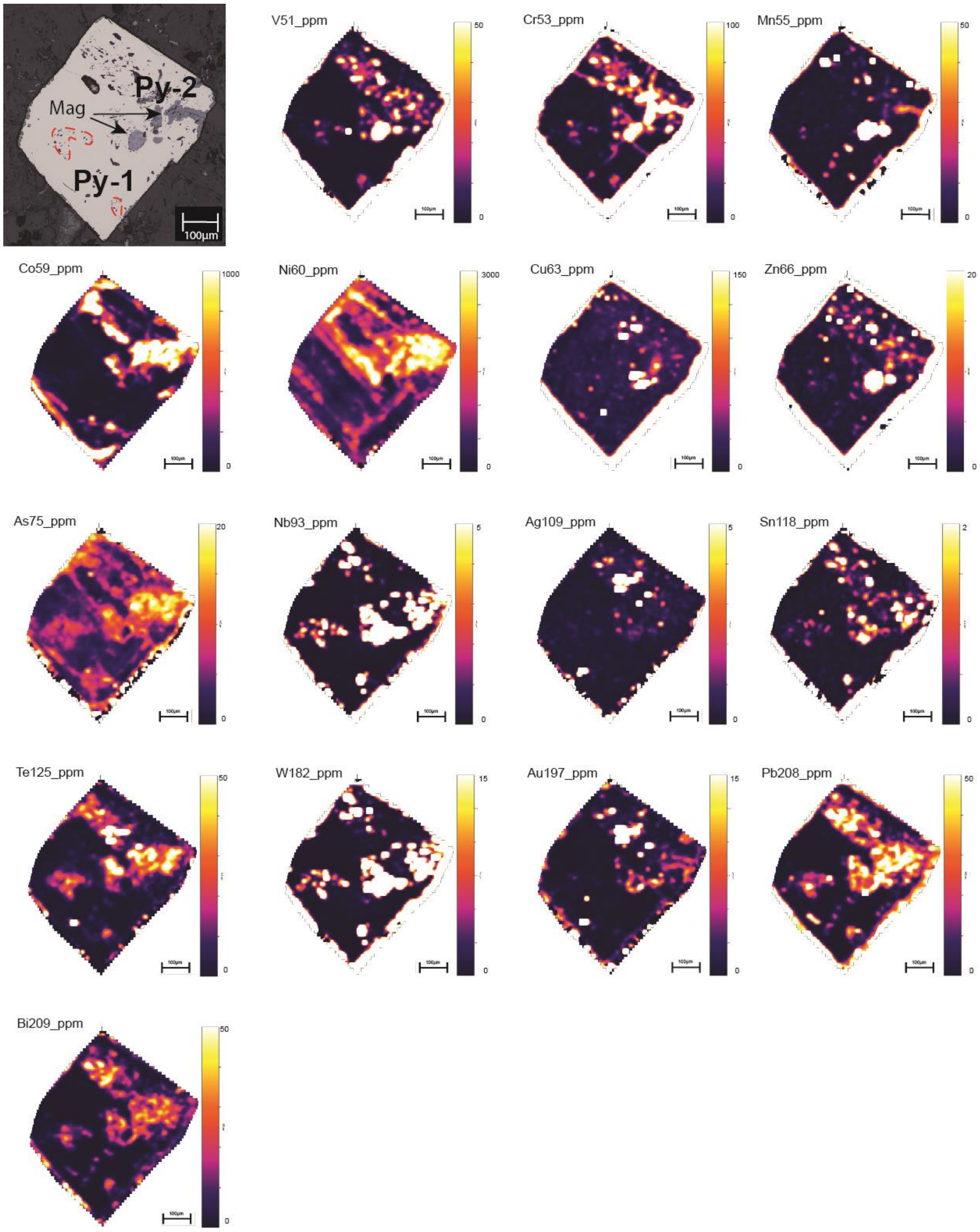

Sample : MEAK20GJF001AG09

Description : A 0.2 mm cubic pyrite located within a sericite (±carbonate) altered fragment within a hydrothermal breccia vein. The pyrite grain is surrounded by primary quartz and sericitized primary plagioclase grains.

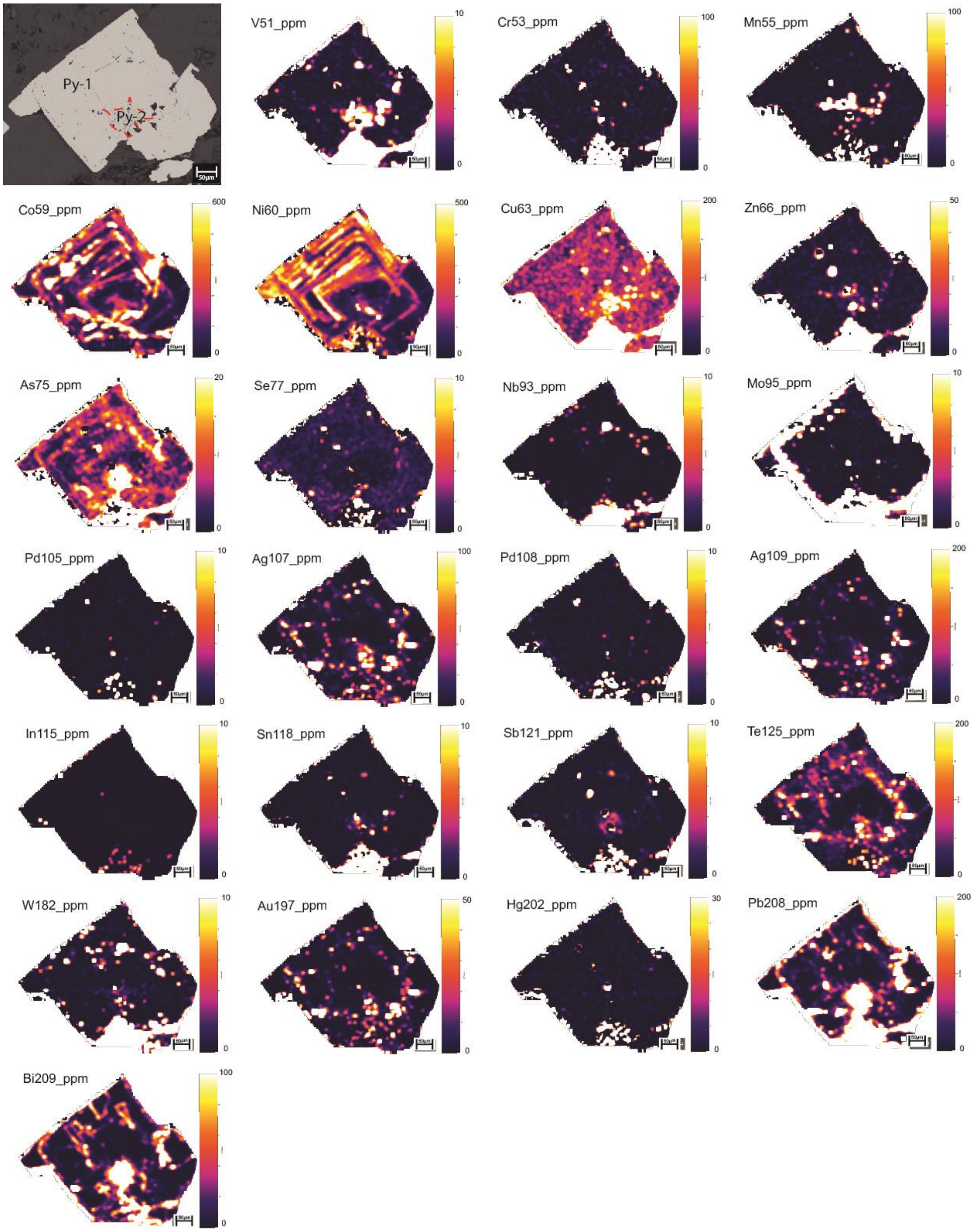

Sample : MEAK20GJF001AG01A

Description : A 0.5 mm cubic pyrite located within the sericite (±carbonate) alteration halo of a quartz chlorite carbonate vein. The pyrite grain is surrounded by primary quartz and sericitized primary plagioclase grains.

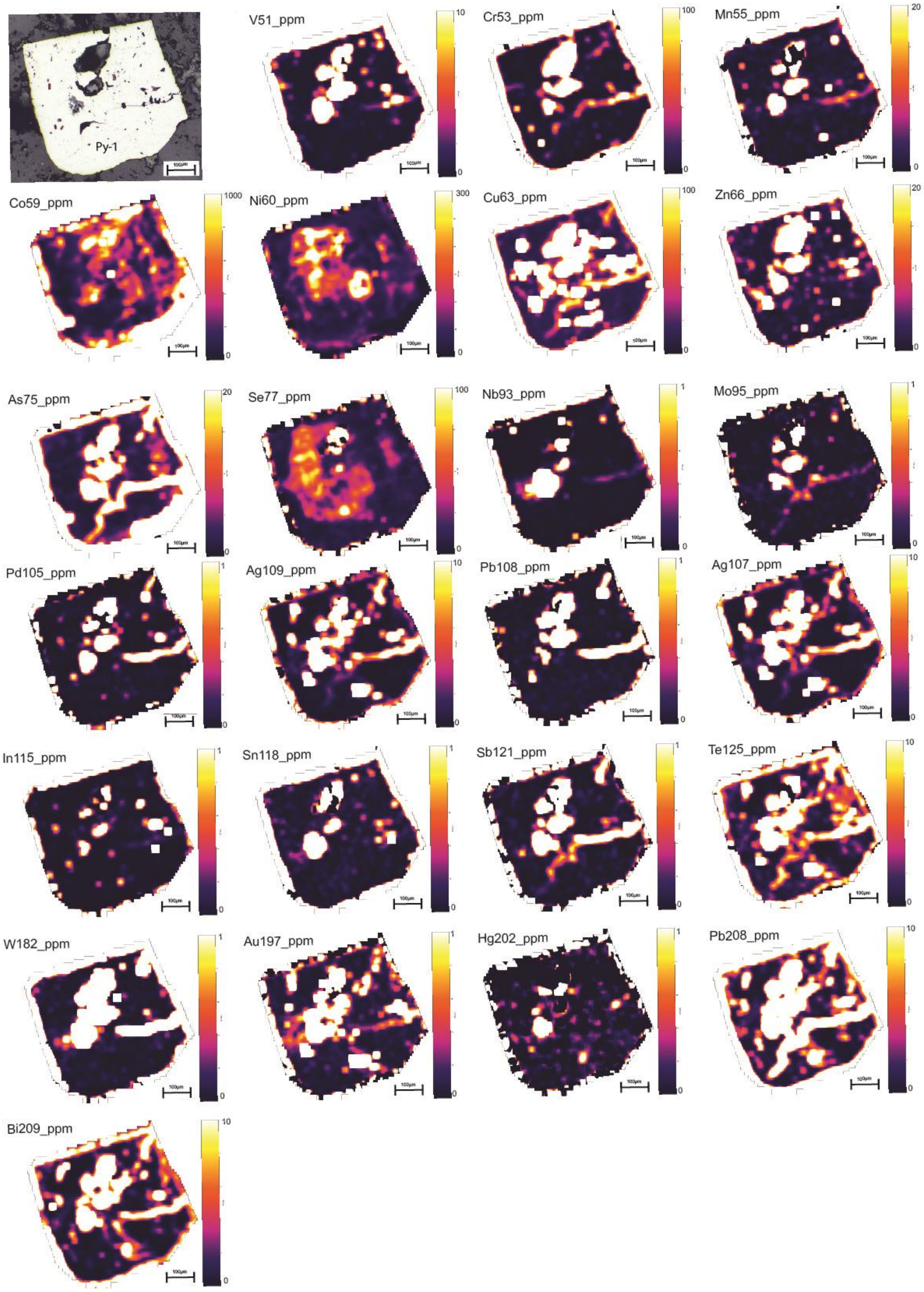

Sample : MEAK20GJF001AG01A

Description : A 0.2 mm cubic pyrite located within the sericite (±carbonate) alteration halo of a quartz chlorite carbonate vein. The pyrite grain is surrounded by primary quartz and sericitized primary plagioclase grains.

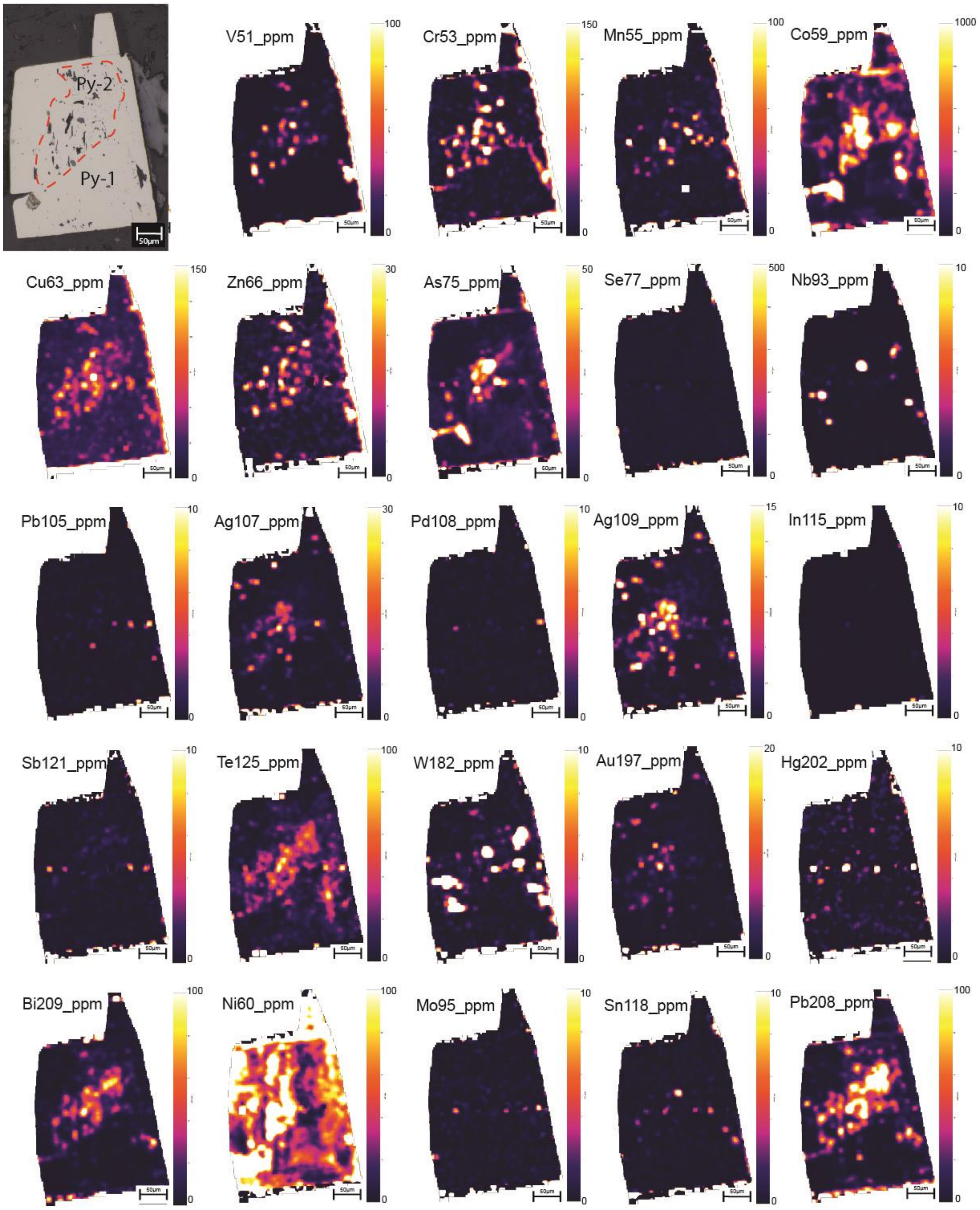

Sample : MEAK20GJF007AG05

Description : An amalgamation of pyrite located within a sulfide rich vein. The pyrite grains are surrounded by quartz.